UNIVERSITÉ DE GRENOBLE

THÈSE

Pour obtenir le grade de

DOCTEUR DE L'UNIVERSITÉ DE GRENOBLE

Spécialité : **Physique de la Matière Condensée et du Rayonnement**

Arrêté ministériel : 7 août 2006

Présentée par

Yaroslav O. KVASHNIN

Thèse dirigée par **Patrick BRUNO**
et codirigée par **Luigi GENOVESE**

préparée au sein **European Synchrotron Radiation Facility (ESRF)**
et de **l'École Doctorale de Physique**

Ab initio study of ferromagnetic transition metals and alloys under high pressure

Thèse soutenue publiquement le **2 Octobre 2013**,
devant le jury composé de :

Alexander I. LICHTENSTEIN
Prof., Institute for Theoretical Physics, Hamburg University, Rapporteur
Mébarek ALOUANI
Prof., Institut de Physique et Chimie des Matériaux de Strasbourg, Rapporteur
Josef KUDRNOVSKÝ
Dr., Institute of Physics, Prague, Examinateur
Claudine LACROIX
D.R. CNRS, Institut Néel, Grenoble, Examinateur
Patrick BRUNO
Prof., Theory group, ESRF, Grenoble, Directeur de thèse
Luigi GENOVESE
Dr., CEA, Grenoble, Co-Directeur de thèse



Acknowledgements

First of all, this thesis would never appear without valuable discussions and support provided by my supervisors Luigi Genovese and Patrick Bruno. Their guidance was of tremendous help and can hardly be overestimated. I also appreciate the amount of freedom which I have been given in terms of the choice of research directions and collaborations.

Raffaella Torchio and Sakura Pascarelli have initiated the project on x-ray dichroism and I was very glad to work in such a team. Nearly all experimental data presented in this manuscript are provided by them.

I thank also Alexei Bossak, Gaston Garbarino and staff of the ID18 for their assistance with the Mössbauer experiment. Luckily, none of the ESRF's equipment went off !

The atmosphere in the Theory group has always been very friendly. The sense of humor of Tim Ziman (Thanks for proofreading) and Andres Cano is something I shall miss. Together with Efim Kats they made each coffee-break a pleasant journey.

I am deeply indebted to Alexander Yaresko for thousands of e-mails which were exchanged between us and for all the time he dedicated to explain me the physics. Our meetings with Andrei Rogalev were also very fruitful for me.

My stays in Prague were unforgettable. I thank Josef Kudrnovský, Vaclav Drchal, Ilja Turek and Vaclav Janis for the arrangement of these visits and our joint discussions.

Working with Pieter Glatzel was a fantastic experience. Those internships at the ID26 have influenced my way of thinking. Thank you for that!

I did my master studies at the Ural Federal University and it is worth thanking the staff of the Department of Theoretical Physics and Applied Mathematics. The background, which I acquired there, was sufficient to perform the Ph.D. and I am grateful to my *alma mater* and teachers for that. I am much obliged to Vladimir V. Mazurenko for introducing me to the field of band structure modeling and magnetism.

I really appreciate the help and support which was provided by Kristina and Dirk, so I could feel at home in Grenoble. Yann, Theo and Eddy are very inspiring guys - they are part of me. Special thanks to my parents and friends for the words of encouragement.

Contents

Acknowledgements i

Abbreviations iv

Abstract vi

Resumé vii

Introduction 1

1 Computational methods in band structure modeling 5
- 1.1 Hartree-Fock method . . . 5
- 1.2 Density Functional Theory . . . 8
- 1.3 XC Approximations . . . 9
- 1.4 Realizations of the DFT . . . 11
  - 1.4.1 Muffin-tin orbitals . . . 12
  - 1.4.2 Plane waves . . . 14
    - 1.4.2.1 Pseudopotentials . . . 15
    - 1.4.2.2 Non-linear Core Correction (NLCC) . . . 16
  - 1.4.3 Linearized Augmented Plane Waves (LAPW) . . . 17
  - 1.4.4 Wavelets . . . 17
- 1.5 Drawbacks of DFT-based methods . . . 20
- 1.6 Practical applications of the DFT formalism . . . 21
  - 1.6.1 Structural properties . . . 22
  - 1.6.2 Magnetism: Mapping on the Heisenberg model . . . 23
    - 1.6.2.1 Frozen magnons simulations . . . 27
- 1.7 Conclusions . . . 28

2 K-edge XMCD study of transition metals under high pressure 30
- 2.1 Introduction: experimental technique . . . 30
- 2.2 Theoretical interpretation of XMCD spectra . . . 32
- 2.3 Bulk Ni: an example of persistent ferromagnet . . . 34
- 2.4 Orbital magnetism in hcp Co under pressure . . . 39
  - 2.4.1 Simple view on the evolution of L and S under pressure . . . 41
- 2.5 Competing phases in FeCo alloy . . . 42
  - 2.5.1 X-ray experiments . . . 43
  - 2.5.2 Phase diagram from first principles . . . 44

2.6 Conclusions . . . 49

3 High-pressure phase of $FePd_3$ ordered alloy from first principles 51
3.1 Introduction . . . 51
3.2 Modeling of incommensurate magnetic structures . . . 53
3.2.1 Spin spirals . . . 54
3.2.2 Canted spin states . . . 57
3.3 Heisenberg exchange parameters . . . 58
3.4 Extended Heisenberg model . . . 61
3.5 Triple-Q phase . . . 64
3.6 Relation to experiments . . . 66
3.7 Conclusions . . . 67

4 Evaluation of stress in the DFT 69
4.1 Introduction . . . 69
4.2 Stress contributions in the PSP formalism . . . 71
4.3 Tests and comparisons . . . 73
4.3.1 Bulk Si . . . 73
4.3.2 $SrTiO_3$ and $LaAlO_3$ . . . 75
4.4 NLCC and intrinsic stress . . . 77
4.5 NLCC and intrinsic stress: Results . . . 78
4.6 Conclusions . . . 80

Conclusions 82

A General equations for the spin wave energies 85
A.1 Collinear magnets with several sublattices . . . 85
A.2 Noncollinear magnetic structures . . . 88

B Derivation of expressions for stress tensor in the DFT 89
B.1 Kinetic stress . . . 89
B.2 Stress tensor from the Hartree energy . . . 90
B.3 Local part of the PSP . . . 92
B.3.1 Long-range part . . . 92
B.3.2 Short-range part . . . 93
B.4 Non-local part of the PSP . . . 94
B.5 XC contribution . . . 96
B.6 Ion-ion impact . . . 96

Bibliography 97

Abbreviations

DFT	**D**ensity **F**unctional **T**heory
DOS	**D**ensity **O**f **S**tates
XMCD	**X**-ray **M**agnetic **C**ircular **D**ichroism
WF	**W**ave**F**unction
MF	**M**ean **F**ield
HF	**H**artree-**F**ock
GS	**G**round **S**tate
HK	**H**ohenberg-**K**ohn
XC	e**X**hange-**C**orrelation
KS	**K**ohn-**S**ham
SC	**S**elf-**C**onsistent
L(S)DA	**L**ocal (**S**pin) **D**ensity **A**pproximation
GGA	**G**eneralized **G**radient **A**pproximation
PW	**P**lane **W**ave
MT	**M**uffin-**T**in
ASA	**A**tomic **S**phere **A**pproximation
ES	**E**mpty **S**phere
LMTO	**L**inear **M**uffin-**T**in **O**rbital
BC	**B**oundary **C**ondition
FFT	**F**ast **F**ourier **T**ransform
PSP	**PS**eudo**P**otential
PAW	**P**rojector **A**ugmented **W**ave
NLCC	**N**on-**L**inear **C**ore **C**orrection
FP	**F**ull-**Potential**
DMFT	**D**ynamical **M**ean **F**ield **T**heory

OP	**O**rbital **P**olarization
FM	**F**erro**M**agnetic
AFM	**A**nti**F**erro**M**agnetic
HS	**H**igh **S**pin
LS	**L**ow **S**pin
NM	**N**on**M**agnetic
PM	**P**ara**M**agnetic
FiM	**F**erri**M**agnetic
SW	**S**pin **W**ave
INS	**I**nelastic **N**eutron **S**cattering
BZ	**B**rillouin **Z**one
R/LCP	**R**ight/**L**eft **C**ircular **P**olarization
DAC	**D**iamond **A**nvil **C**ell
SOC	**S**pin-**O**rbit **C**oupling
XAS	**X**-ray **A**bsorption **S**pectroscopy
XRD	**X**-**R**ay **D**iffraction
PBE	**P**erdew-**B**urke-**E**rnzerhof
NFS	**N**uclear **F**orward **S**cattering
SS	**S**pin **S**piral
FU	**F**ormula **U**nit
DLM	**D**isordered **L**ocal **M**oment
CPA	**C**oherent **P**otential **A**pproximation
NN	**N**earest-**N**eighbor
GTH	**G**oedecker-**T**utter-**H**artwigsen
HGH	**H**artwigsen-**G**oedecker-**H**utter
MIT	**M**etal-**I**nsulator **T**ransition

Abstract

The subject of the present thesis is the investigation of magnetic properties of transition metals and their alloys under high pressure by means of first-principles calculations.

First, the results of the K-edge x-ray magnetic circular dichroism (XMCD) experiments on Ni and Co are interpreted. It is shown that the experimental pressure evolution of the data should be compared with that of the p-projected orbital magnetization. I emphasize that the spin and orbital moments have different behavior upon compression.

In the case of FeCo alloy the structural transition occurs under the pressure of 35 GPa. I propose that the emergence of antiferromagnetism can explain the disappearance of the XMCD signal at the Fe and Co K-edges.

Then, the phase transformation in $FePd_3$, induced under pressure of 12 GPa, is investigated. I demonstrate that the system is described by an extended Heisenberg model, containing strong biquadratic exchange interactions. According to the results, $FePd_3$ undergoes a transition from the ferromagnetic to the noncollinear triple-Q state when compressed.

Finally, the implementation of the stress tensor in the `BigDFT` software package is presented. It is shown that an explicit treatment of core electrons can considerably reduce the errors introduced by the pseudopotentials. Thus the estimates of the structural properties can be improved.

Resumé

Le sujet de cette thèse porte sur l'étude des propriétés magnétiques de métaux de transition et leurs alliages sous haute pression au moyen de calculs *ab initio*.

D'abord, les résultats de mesures de dichroïsme magnétique circulaire des rayons X (XMCD) au seuil K du nickel et du cobalt sont interprétés. Je montre que les données expérimentales doivent être comparées à celle de l'aimantation d'orbite projetée sur les états p. Je mets en avant que la pression affecte différemment le spin et le moment orbitalaire.

Dans le cas de l'alliage FeCo, la transition structurelle s'effectue sous une pression appliquée de l'ordre de 35 GPa. Je propose que l'émergence de l'antiferromagnétisme peut expliquer la disparition du signal XMCD au seuil K du fer et du cobalt.

Ensuite, la transformation de phase dans $FePd_3$, induite sous une pression de 12 GPa, est étudiée. Je démontre que le système est décrit par un modèle de Heisenberg étendu, contenant interactions d'échange biquadratiques forts. Selon nos résultats, $FePd_3$ subit une transition de l'etat ferromagnétique á l'état triple-Q non-colinéaire, lorsqu'il est compressé.

Enfin, une mise en oeuvre du tenseur des contraintes dans le code `BigDFT` est présentée. Il est montré qu'un traitement explicite des électrons de coeur permet de réduire considérablement les erreurs introduites par les pseudo-potentiels. Ainsi, les estimations des propriétés structurales peuvent être améliorées.

Introduction

Understanding the processes deep inside the Earth has been a dream of humanity since antiquity. There are lots of mysteries, as, for example, the origin of our planet's magnetic field. This problem is still under debate – a few models have been proposed but none of them is able to give an unequivocal answer.

Unfortunately, the level of today's technology allows us to dig holes no deeper than a few kilometers. So there is still a very long way to the Earth's core. Nonetheless, we know the constitution of the mantle and more deeper regions of the Earth. There are such elements as oxygen, magnesium, silicon and iron. The inner core of our planet is made predominantly of iron and nickel. These transition metal elements are of the greatest interest, since at normal conditions they possess spontaneous magnetization. We can also estimate the most important thermodynamic parameters in this region: pressure in the inner core region should be about 300 GPa and temperature exceeds 4000 K [1].

Thanks to the use of diamond anvil cells it has become possible to reach pressures of the order of 100 GPa. Regarding the second parameter, today's lasers are able to heat the matter up to the necessary level. So, in principle, the Earth's core conditions can be reconstructed in a modern laboratory. In combination with element-selective techniques like x-ray spectroscopy, this becomes a powerful tool for the investigation of the electronic and magnetic properties of the Earth's interior.

Moreover, from a fundamental point of view an application of pressure to the transition metals allows us to verify existing models of magnetism. The reality is that there is no unified theory which could *a priori* describe any magnet. Hence, in studying a particular system one is forced remain in one of two frameworks, depending on the

[1] In spite of such high temperatures, the inner core is solid, since the tremendous pressure pushes the melting point of iron-nickel alloys much higher.

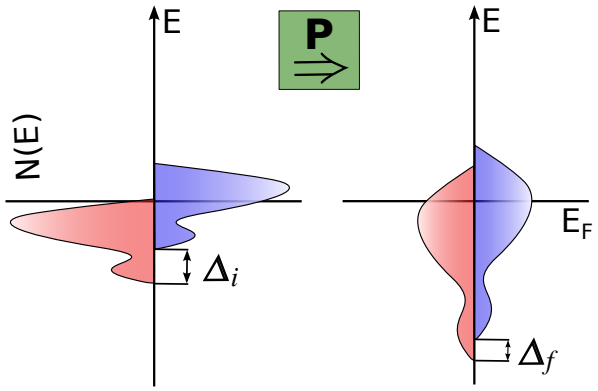


FIGURE 1: Schematic representation of densities of states ($N(E)$) in ferromagnetic system and its changes upon application of pressure. Bands become wider due to increase of orbital overlap, while magnetic splitting tends to decrease ($\Delta_i > \Delta_f$).

degree of localization of the magnetization density. Magnetic systems which consist of relatively well-localized spins (in real space) are usually studied within a Heisenberg model. On the contrary, itinerant magnets, characterized by delocalized magnetization density, are treated with the help of Stoner model [156].

The magnetism in transition metals arises from the unfilled $3d$ electron shell. The spatial distribution of $3d$ WFs is such that electrons are located right on the border between atomic localization and formation of wide electronic bands (see e.g. Ref. [155][p. 223]). As a result, the very same $3d$ states can exhibit opposite behavior depending on their environment and filling. Thus compression, i.e. a change of interatomic distances, allows one to adjust the localization in a precisely controlled way.

Effects of pressure on electronic structure of ferromagnetic metals are known. The most general trends are shown on Fig. 1. As the interatomic distance decreases, the overlap between electrons wavefunctions gets larger, which leads to their delocalization. According to Stoner theory, the density of states at the Fermi level ($DOS(E_f)$) should exceed a certain threshold in order to favour appearance of ferromagnetic order. Therefore it is reasonable to assume that application of pressure should eventually lead to the disappearance of magnetism.

This suggested tendency is indeed observed in experiments, but such a magnetic transition does not really occur for $3d$ metals. Structural transitions usually take place at lower pressures than needed to violate the Stoner criterion. For instance, such situation appears in bcc iron, which undergoes a transition to a non-magnetic hcp phase [115].

In the present thesis we will try to get deeper insight into the change of magnetic properties of $3d$ systems with the help of the Heisenberg Hamiltonian. The key quantity of the present theory is the set of interatomic exchange parameters J_{ij}. These parameters will be extracted from realistic band structure calculation for a particular system and their pressure dependence will be studied. Their change with lattice contraction is not straightforward to predict. On one hand, reduction of the lattice constant leads to increase of the overlap. Therefore the so-called *direct* exchange interaction should become larger. On the other hand, the local magnetic splitting gets smaller, as was already shown. Thus there are two general tendencies which compete with each other. The problem gets more complicated due to the fact that in metallic systems the J's are rather long-ranged in space. It turns out that magnetic moments separated by several Angströms are still coupled, and this coupling is not related to direct overlap of the orbitals. Hence, this requires the use of electronic structure calculations which are able to provide a detailed description of electronic bands.

Organization of the thesis

The thesis is organized as follows:

Chapter 1 contains an overview of *ab initio* band structure methods. It is primarily devoted to the Density Functional Theory (DFT), which is the main instrument in the present study. Drawbacks and merits of different realizations of this theory are discussed. Special attention is given to the study of structural and magnetic properties. Such quantities as stress, pressure and magnetic couplings are formulated in terms of the present apparatus.

Chapter 2 concerns analysis of K-edge x-ray magnetic circular dichroism (XMCD) data in various $3d$ systems. First, a historical overview is given of present experimental technique, as well as its theoretical modeling. Next, XMCD spectra measured on bulk Ni, Co and FeCo alloys are analyzed with the help of first-principles calculations.

In Chapter 3 an analysis of magnetic interactions in $FePd_3$ is presented. Based on these results, a new magnetic ground state is suggested to be stabilized under pressure in this system. Various experiments which could confirm these findings are proposed.

Chapter 4 is devoted to calculation of the stress tensor within a particular DFT code. The computational scheme is applied to various classes of materials and the results are compared with prior realizations of this formalism. Further, an emphasis is given to the impact of core electrons on structural properties of quantum systems. The importance of this contribution is discussed.

Finally, general conclusions and perspectives of this work are outlined.

Chapter 1

Computational methods in band structure modeling

The so-called *ab initio* (i.e. first-principles) methods for electronic structure calculations are widely used in modern science. They allow us to simulate and sometimes even predict properties of the actual materials with no use of any adjustable parameters. These methods require almost no information about the system: it is just necessary to know its crystal structure in order to start the calculation. Then any observable quantity, like equilibrium volume, magnetization, ionic charge and others can be extracted from the calculation and sometimes directly compared with experimental data. The range of application of these methods spreads from the material science, solid state physics, chemistry and biology. This is how science is made nowadays, but such progress was achieved only recently. Therefore, before describing the state-of-the-art methods this chapter will start by the historical overview of the electronic structure modelling.

1.1 Hartree-Fock method

To have such powerful approaches, able to deal with the quantum systems consisting of many particles, was one of the biggest challenges for physics of XX'th century. One of the first methods was proposed by Hartree in 1928 [76]. At that time it was already known that the properties of quantum systems are governed by the Schrödinger equation. In particular, a system which consists of N atoms and n electrons coupled via

electromagnetic interaction is described by the following Hamiltonian:

$$\begin{aligned}\hat{H} = &-\frac{1}{2}\sum_{i=1}^{n}\nabla_{r_i}^2 + \frac{1}{2}\sum_{i\neq j}\frac{1}{\mid \vec{r_i} - \vec{r_j} \mid} - \sum_{I=1}^{N}\sum_{i=1}^{n}\frac{Z_I}{\mid \vec{R_I} - \vec{r_i} \mid} \\ &-\sum_{I=1}^{N}\frac{1}{2M_I}\nabla_{R_I}^2 + \frac{1}{2}\sum_{I\neq J}\frac{Z_I Z_J}{\mid \vec{R_I} - \vec{R_J} \mid},\end{aligned} \tag{1.1}$$

where $\vec{r_i}$ and $\vec{R}_I$ are the positions of electrons and atoms, respectively. Letters Z and M denote charge and mass of each nucleus. This equation is written in the atomic units: mass is in the units of electron mass m_e and charge is measured in electronic charge $\mid e \mid$. We are eventually interested in finding the eigenvalues and eigenvectors of the corresponding operator, which will give an access to all observable properties. But the Hilbert space dimension is $3(N+n)$, which makes it certainly impossible to diagonalize the matrix explicitly.

Nonetheless, the last two terms in the right-hand side (r.h.s.) of Eq. (1.1) describe the dynamics of ions, which are at least ≈1836 times heavier than electrons. Therefore, it is well justified to decouple these degrees of freedom from electronic ones. This can be done using so-called Born-Oppenheimer approximation [17], which consists in treating the ions classically. It is assumed that the ionic positions are completely frozen and they form an electrostatic potential which acts on electrons. Hence the atomic positions and charges enter the Eq. (1.1) as the external parameters in our quantum problem.

This way the dimension of the problem is reduced (to $3n$ variables) and is associated with electronic degrees of freedom solely. However, the Hilbert space dimension is still too large for the real compounds.

Therefore we are forced to use approximations in order to simplify the initial problem. The idea of Hartree was to map the many-body problem into a non-interacting particle problem in an effective potential. Hence, each electron is moving in some central field created by nucleus and other electrons. Within the proposed method the many-electron wavefunction (WF) $\Psi(r_1, r_2, ..., r_n)$ is represented as a product of one-particle wavefunctions:

$$\Psi(r_1, r_2, ..., r_n) = \psi_1(r_1)\psi_2(r_2)\dots\psi_n(r_n), \tag{1.2}$$

each of those satisfies the one-particle Shrödinger equation:

$$\Big[-\frac{1}{2}\nabla^2 + V_{ext} + \Phi_i\Big]\psi_i(r_i) = \varepsilon_i\psi_i(r_i), \tag{1.3}$$

where V_{ext} is external lattice potential and Φ_i is a potential of electron-electron interaction. So the influence of all other electrons on a certain particle is taken into account in a mean-field (MF) manner and enters the Hamiltonian via the terms of the following type:

$$U_{ij} = \iint d\vec{r}_1 d\vec{r}_2 \mid \psi_i(\vec{r_1}) \mid^2 V_{ee}(\vec{r}_1 - \vec{r}_2) \mid \psi_j(\vec{r_2}) \mid^2, \tag{1.4}$$

where U_{ij} is a direct Coulomb interaction between wavefunctions corresponding to the states i and j. It has the form of interaction between two charge densities like in classical electrodynamics. This was a so-called Hartree approximation.

Later it was shown that during the construction of a many-body WF it is necessary to satisfy rules of Fermi statistics: i.e. the antisymmetry of fermionic operators with respect to the swap of two particles [53]. The r.h.s. of Eq. (1.2) becomes a determinant of different ψ's, called "Slater determinant" [151], namely:

$$\Psi(r_1, r_2, ..., r_n) = \begin{vmatrix} \psi_1(r_1) & \psi_1(r_2) & \dots & \psi_1(r_n) \\ \psi_2(r_1) & \psi_2(r_2) & \dots & \psi_2(r_n) \\ \dots & \dots & \dots & \dots \\ \psi_n(r_1) & \psi_n(r_2) & \dots & \psi_n(r_n) \end{vmatrix}. \tag{1.5}$$

This is the base of the Hartree-Fock technique. Reformulation of $\Psi(r_1, r_2, ..., r_n)$ has an important consequences and results in the appearance of additional contributions to Φ_i - the non-local *exchange* terms of the following type:

$$J_{ij} = \iint d\vec{r}_1 d\vec{r}_2 \psi_i^*(\vec{r_1})\psi_j^*(\vec{r_2})V_{ee}(\vec{r}_1 - \vec{r}_2)\psi_j(\vec{r_1})\psi_i(\vec{r_2}). \tag{1.6}$$

It is worth emphasizing that this is a purely quantum effect, which originates from Pauli exclusion principle. However, exchange term is an essential quantity in the theory of magnetism[1]. So the quantity J_{ij} is important in the present context and will be widely

[1] It is fascinating to realize that we have actual magnetic materials *solely* thanks to laws of quantum mechanics.

used throughout this thesis.

Concerning the Hartree-Fock method, it is worth noting, that in some cases the system's WF should be described via a linear combination of Slater determinants, corresponding to the states with similar energies. In principle, this procedure gives a reasonably exact wavefunction, but the computational effort grows very fast with increase of the number of particles. Hence, in practice, the method is only used if the quantum problem is (or can be reduced to) relatively small.

1.2 Density Functional Theory

Due to the above-mentioned reasons, it is clear the use of WFs is not so efficient for realistic systems. A big step forward in the problem of finding ground state (GS) energy was made by Hohenberg and Kohn in 1964 [78, 96]. They suggested to operate with electronic density (ρ) instead. Their celebrated Hohenberg-Kohn (HK) theorem states that for a given n particles the GS charge density determines *uniquely* the external potential of the electronic Hamiltonian. In the other words, there is a one-to-one correspondence between GS density and external potential, which controls the inhomogeneity of the electron gas. The total energy (E) is a functional of ρ and reaches its minimum for true GS density ρ_0:

$$E[\rho] = T_0[\rho] + \int d\vec{r}\rho(\vec{r})V_{ext}(\vec{r}) + \frac{1}{2}\iint d\vec{r}d\vec{r'}\frac{\rho(\vec{r})\rho(\vec{r'})}{\mid \vec{r} - \vec{r'} \mid} + E_{xc}[\rho], \tag{1.7}$$

where T_0 is the kinetic energy contribution and E_{xc} is the exchange-correlation (XC) term. The second and third terms are electron-ion Coulomb interaction and electron-electron interactions, respectively. The latter contribution has exactly the same form as in Hartree method and therefore is called Hartree potential. Instead of Fock contributions, one introduces the E_{xc} term which is called to mimic the exchange part and also many-body (correlation) effects. We can define a new quantity $\epsilon_{xc}(\vec{r})$ – the so-called *XC density per particle* which will be associated with E_{xc}, so that:

$$E_{xc}[\rho] = \int d\vec{r}\rho(\vec{r})\epsilon_{xc}[\rho](\vec{r}). \tag{1.8}$$

DFT would be an exact theory if we knew the true form of this term, which is missing. Hence it is inevitable to use some approximations to E_{xc} and their choice plays a crucial role in the theory. This problem will be addressed later in more details.

Having defined a suitable XC term, the GS of the system can be obtained. We can use an advantage of the DFT that it is not important from which WFs the electron density is built. Therefore for practical applications ρ can be defined as:

$$\rho(\vec{r}) = \sum_{i=1}^{n} |\psi_i(\vec{r})|^2, \tag{1.9}$$

where n is a number of electrons (which is fixed). Varying the Eq. (1.7) with respect to new variables $\psi_i(\vec{r})$ with an additional constraint for their normalization leads to the system of coupled Kohn-Sham (KS) equations:

$$\Big[-\nabla^2 - \sum_I \frac{2Z_I}{\mid \vec{r} - \vec{R}_I \mid} + 2\int \frac{\rho(\vec{r'})}{\mid \vec{r} - \vec{r'} \mid} d\vec{r'} + V_{xc}(\vec{r})\Big]\psi_i = \varepsilon_i \psi_i, \tag{1.10}$$

where ε_i are the Lagrange multipliers that form the spectrum of single-particle states; The XC potential is a functional derivative of E_{xc}, i.e.:

$$V_{xc} = \frac{\delta E_{xc}[\rho]}{\delta \rho(\vec{r})} = \frac{d}{d\rho}(\rho \epsilon_{xc}[\rho]). \tag{1.11}$$

System of Eq. (1.10) has to be solved iteratively. One can start calculation with trial WFs, for example a set of isolated ionic states, and solve the Poisson equation to find Hartree potential. Then one has to diagonalize the KS Hamiltonian and construct the new electronic density. The procedure has to be repeated until one reaches the minimum of the total energy $E[\rho_0]$. This is the basic representation of a self-consistent (SC) loop. In practice, there are different strategies for updating the density and several possible choices of the convergence criteria, but we shall omit these details at this stage.

1.3 XC Approximations

As it has already been mentioned, the biggest problem of the DFT is the lack of an exact form of the XC term. There is no universal approximation which could correctly

describe properties of any material. However, for wide range of systems the so-called Local Density approximation (LDA) is rather successful.

In the present framework the XC density is taken in the form for homogeneous interacting electron gas (h.g.) of the density $\tilde{n}$, but at each point in space $\tilde{n}$ is substituted for an *actual* density ρ. Hence $\epsilon_{xc}[\rho] = \epsilon_{xc}^{h.g.}(\rho(\vec{r}))$ and one can write explicitly:

$$E_{xc}[\rho] = \int \rho(\vec{r})\epsilon_{xc}(\rho(\vec{r}))d\vec{r}. \tag{1.12}$$

Spin-polarized version of LDA, called local spin density approximation (LSDA), is used for magnetic systems. This method introduces two separate densities of electrons with positive and negative spin projections on quantization axis, $\rho_\uparrow$ and $\rho_\downarrow$, respectively. The quantity ϵ_{xc} can be parametrized using results of numerical calculations and several realizations are present nowadays [134, 167, 168].

L(S)DA was implemented in the first realizations of the DFT and immediately showed an impressive performance. Such a simple approximation led to a rather good prediction of band structures of the whole class of conventional semiconductors, alkali and transition metals [88]. In principle, LDA provides the most accurate results for systems, whose electronic density varies rather slowly in space.

The next generation of the XC functionals was built using not only the electronic density but also its gradient, i.e. :

$$\epsilon_{xc}(\vec{r}) = \epsilon_{xc}(\rho(\vec{r}), |\vec{\nabla}\rho|(\vec{r})). \tag{1.13}$$

In this case, XC potential, according to Eq. (1.11), is given by:

$$V_{xc}(\vec{r}) = \frac{d}{d\rho}(\rho\epsilon_{xc}[\rho]) + \int d\vec{r'}\rho(\vec{r'})\frac{\partial\epsilon_{xc}}{\partial|\nabla\rho|}\frac{\delta|\nabla\rho|(\vec{r'})}{\delta\rho(\vec{r})}. \tag{1.14}$$

The first term in the current expression is the same as in the case of the LDA, while the second one represents an additional correction. The present approach is called Generalized Gradient Approximation (GGA) [135].

In most cases, L(S)DA and GGA provide with very similar ground states. GGA often provides better estimates of structure-related quantities, like bulk moduli (B) and equilibrium volume (Ω_0) [73]. In terms of other properties, magnetic for instance, usually there are no significant differences between results provided by these two methods.

However, these results are not general and there is no *a priori* knowledge about the choice of the XC approximation for a particular system. A well-known example is elementary iron: LDA predicts its paramagnetic fcc phase to be more stable than ferromagnetic bcc one, which is a real GS of iron in nature, while GGA is able to overcome these unphysical outcomes [176]. On the other hand, GGA faces problems in predicting correctly the stable crystal structure of Fe_3Al alloy [104].

In general, GGA shares the same problems with LDA in modeling a certain class of materials, so-called "strongly correlated" systems. This problem will be addressed in the next section.

It's worth mentioning that these days the list of available functionals is not limited to LDA/GGA types only. An improvement of XC potentials is a stand-alone field of research which develops very fast. For instance, there are attempts to add a fraction of the *exact* exchange energy, i.e. provide a combination of the DFT with HF methods [12]. The results for some molecular systems have proven that these "Hybrid" functionals provide a more accurate bond length and ionization energy estimations as compared with experimental data [11].

For deeper insight into the constellation of existing functionals the reader is referred to Ref. [113] and references therein. Present study concerns the investigation of magnetic properties of pure transition metals and their alloys. For this type of systems classical LDA/GGA-type functionals are known to be suitable (see e.g. [8]) and will be used throughout this thesis work.

1.4 Realizations of the DFT

In last decades plenty of DFT-based codes have appeared, in spite of the fact that they all implement the same theory. The main reason for these developments is related with an increase of accuracy and ability to treat bigger systems on a reasonable time-scale.

Moreover, certain physical quantities can be accessed more easily depending on the employed formalism.

Different realizations of the DFT can be characterized according to the basis functions used for expressing the KS orbitals. These basis sets can be divided in two major groups: the ones which are *more* localized in reciprocal space (plane waves [PW], for example) and in direct one (like Gaussian-type orbitals [GTO][2]).

As a limiting case one can think of a completely isolated (non-periodic) molecular system. Clearly, the WFs are difficult to treat using PWs, since they contain too many components in the expansion. Atomic-like functions would be more efficient for this study.

Therefore, before starting the band structure simulation of a certain compound, it is reasonable to inquire whether the system is mainly characterized by highly mobile (delocalized) electrons, which is a typical situation in metals, or it is an insulator with quite localized WFs. Indeed, periodic systems are more difficult to sort: they sometimes exhibit a mixed behavior, but normally can be attributed to one of two groups. Thus an appropriate set of basis functions can be chosen. In other words, the most efficient way is to choose the basis set according to particular needs.

It is sometimes necessary to work with several realizations of the DFT and balance between them. Here we wish to make an overview of several basis sets, each of whose will be used in the present work. Note that the list is not exhaustive, but represents a diversity of the DFT codes. Interested reader is referred to the book by R. Martin [114].

1.4.1 Muffin-tin orbitals

At the time of the first developments of the DFT codes the computers performance was much lower than today. The codes which were written 40 years ago aimed to reduce the computational effort, so the state-of-the-art machines were capable to solve the problem. Thus the first realizations of the DFT contained some additional approximations (beyond intrinsic), which in principle can be avoided nowadays thanks to the progress

[2] These functions are widely used in the field of quantum chemistry for studying molecular compounds. Minor attention is paid to this topic in the present thesis, since it is primarily concerns metallic systems.

of computational technology. However, the methods developed at whose times are still used and there are reason for that.

One of the first approaches which incorporated the DFT was similar to the tight-binding method. In this spirit WF of each electron, which is a solution of KS equation (Eq. (1.10)), is approximated as a sum of atomic-like orbitals, centered on a certain atom. Due to the symmetry of the Hamiltonian under consideration, it is reasonable to define a sphere of a certain radius (R_{MT}) around each atom and assign it to this ion. O.K. Andersen [4] suggested to extend these regions so that the entire system will be represented by a sum of overlapping spheres. This way of the space partitioning is called called the atomic sphere approximation [ASA]. For not-so-close-packed crystal structures we can fill the interstitial space with the empty spheres (ES), possessing zeroth charge.

At this stage we can make an approximation to the potential and require it to be spherically symmetric inside each sphere and constant outside, so that:

$$V(\vec{r}) = \begin{cases} V(|\vec{r}|), & \text{if } |\vec{r}| \leq R_{MT} \\ C, & \text{if } |\vec{r}| > R_{MT} \end{cases} \tag{1.15}$$

A potential defined this way is called the muffin-tin (MT) one. Inside the sphere our problem is reduced to the Shrödinger equation with spherical potential, which solution is known. Core electrons in each ion form localized levels with practically no dispersion which are relatively easy to calculate. Valence electrons that participate in formation of bands, certainly require a more thorough treatment.

Outside of each sphere there is the Laplace equation which has to be solved: $\nabla^2\Phi_i = 0$. Hence a true valence WF has to match the boundary conditions (BCs) on the spheres. Therefore it becomes not only a function of position, but also that of *energy*.

Andersen's idea was to linearize this energy-dependence [4], i.e. take first two terms in corresponding Taylor expansion :

$$\psi_i(\vec{r}) = \sum_{lm} \left[A_{lm}\phi_l(\vec{r}, E_\nu) + B_{lm}\frac{\partial\phi_l}{\partial E}(\vec{r}, E_\nu) \right] Y_{lm}(\vec{r}), \tag{1.16}$$

where the sum is over angular momentum quantum numbers (l), ϕ_l is a solution of the radial Shrödinger equation for the energy E_ν inside a MT sphere; and Y_{lm} are Legendre polynomials. Coefficients A_{lm} and B_{lm} are fitted in order to fulfill the BCs.

The linearization energy E_ν is usually chosen to be in the center of the corresponding band. Thanks to such choice, the errors due to linearization are efficiently canceled.

On the first sight, this looks as a rather crude approximation of the real band structure. In reality this approach was a real breakthrough. It turned out to be quite accurate for real applications and quickly became an essential tool of computational solid state physics.

Why is this method still used ? Its main advantage, especially nowadays, is performance. A band structure of simple metal can be calculated in few seconds. Use of the ASA is not always physically motivated, but on the other hand it allows to access the local quantities (via occupation matrices) straightforwardly. Since entire space is partitioned, one can immediately obtain the magnetization per atom, ionic charge and other important properties. Additionally, an analogy with the tight-binding method makes interpretation of the results quite simple and intuitive.

1.4.2 Plane waves

In one of the most wide-spread realizations of the DFT, the KS wavefunction is represented as a linear combination of orthogonal plane waves:

$$\psi_l(\vec{r}) = \sum_{|\vec{G}|<G_{max}} C_G^l \exp\left(i\vec{G}\cdot\vec{r}\right), \tag{1.17}$$

where $\vec{G}$ is a vector of reciprocal space. In principle there is only one parameter which has to be adjusted– the *energy cut-off* which sets the maximal modulus of reciprocal vectors G_{max} used in Eq. (1.17). The cut-off is a variational parameter, namely its increase results strictly in lowering the absolute value of the total energy. Hence the accuracy is straightforward to control.

In general this basis set is very convenient to operate with. For instance, in Fourier space the kinetic part of the Hamiltonian is just diagonal. In addition, these codes widely use the Fast Fourier Transform (FFT), which gives an almost linear ($\sim n \log n$) scaling of computational time with respect to number of electrons.

On the other hand, wavefunctions have to be re-orthonormalized on each iteration and this step is the most demanding in the whole SC process. As a result, the overall

computational cost grows as n^3 and limits the domain of application of PW's up to the systems containing few hundred atoms. Nonetheless, PWs is a suitable basis set for periodic and highly-symmetric systems.

1.4.2.1 Pseudopotentials

In practice, the KS WFs strongly oscillate in the vicinity of atomic core. In order to represent such function in Fourier space one will need to drastically increase the size of PW set to obtain reasonable accuracy. This is not efficient and sometimes not even feasible. However, the nucleus charge is largely screened by core electrons. Thus valence electrons – the ones which we are primarily interested in – do not "feel" this bare charge. So the total ionic (i.e. combined nucleus and core electrons) potential can be substituted by another operator, called "pseudopotential" (PSP), which mimics *true* potential in some region of space. Usually this region is located outside of the sphere of a certain radius (R_{core}).

Pseudopotentials are meant to provide a detailed representation of ionic charge influence on valence electrons. They normally consist of two terms: local and non-local ones. The first part is a function, which depends solely on the distance from the nucleus, being purely isotropic. However, in general case, core electrons occupy orbitals with different l quantum numbers. This brings some anisotropy on the produced potential. In the PSP present effect is taken into account via an introduction of $l-$dependent terms, called "non-local" ones. Thanks to these terms, valence states, characterized by different l-numbers, are affected differently by core electrons.

With the help of the PSP, the dimension of the problem is reduced (only valence electrons are considered) and size of the basis set is decreased. Although it is highly beneficial, the method has certain drawbacks.

First of all, core electrons do not enter the simulation explicitly and their action is not updated during the SF loop. This is usually not a problem if the system is next to equilibrium volume. However, can cause some undesired effects if one wants to study

properties at ultra-high pressures. As a solution one has to use "harder" PSPs (which require higher cut-off) with semi-core states treated explicitly [3].

Secondly, the construction of the pseudopotential is a procedure, which is rather complex and not easy to automatize. In most cases, users of the PW codes have to use PSPs provided by developers within the same package. In practice, it turns out that a certain PSP represents some physical properties better than others in comparison with all-electron calculations taken as reference. This is not related with the accuracy of the DFT formalism itself and is just due to self-introduced computational errors.

Hence, the construction of a PSP has to be done with care and special attention must be paid to its *transferability*, i.e. the ability to reproduce well the all-electron behavior of a given atom independently of its chemical environment.

1.4.2.2 Non-linear Core Correction (NLCC)

One of the possibilities to improve the quality of PSPs is inclusion of nonlinear core corrections (NLCC) [108], where the core charge density (ρ_c) is explicitly introduced. Yet, it is considered to be independent of chemical environment and is frozen during the self-consistent process. Usually, for simplicity, the distribution of the core electrons is represented in a simple analytical form.

In order to understand the importance of such treatment of ρ_c, it is useful to consider the overall spin polarization of a system, i.e. the following quantity: $\xi(\vec{r}) = (\rho_\uparrow(\vec{r}) - \rho_\downarrow(\vec{r})) \,/\, (\rho_\uparrow(\vec{r}) + \rho_\downarrow(\vec{r}))$, where $\{\uparrow,\downarrow\}$ denote spin projections. Clearly, ξ is poorly represented, if core electrons are neglected. In most cases the primary contribution to the total charge density comes from low-lying levels. Even though the spin density is negligible in the core region, accounting for $\rho_{c\uparrow(\downarrow)}$ affects ξ dramatically. Let us imagine, for instance, an ionic configuration where all valence electrons have the same spin projection, e.g. $|\uparrow\uparrow\uparrow\uparrow\uparrow\rangle$. If only valence electrons are considered, then: $\xi \to 1$. Taking into account core electrons (suppose that $Z >> 1$) results into: $\xi \to 0$. Since ξ is an important quantity, the NLCC is expected to improve the description of spin-polarized valence states.

[3] This is especially important in the case of Projector Augmented Wave (PAW)[15] formalism. Here the "core " sphere radius is much larger comparing with classical PSP, so even moderate pressure can cause an overlap of these regions which is, strictly speaking, forbidden.

1.4.3 Linearized Augmented Plane Waves (LAPW)

Present approach is a sort of combination of the methods described above. Here, MT spheres are also introduced, but in a different manner: they do not overlap, leaving the interstitial space untouched.

Within MT sphere the potential is not assumed to be isotropic ($\sim Y_{00}$), but also contains higher-order expansion coefficients, so that :

$$V(\vec{r}) = \begin{cases} \sum\limits_{lm} V_{lm}(\vec{r}) \cdot Y_{lm}(\vec{r}), & \text{if } |\vec{r}| \leq R_{MT} \\ \sum\limits_{\vec{G}} V_G \cdot \exp\left(i\vec{G}\vec{R}\right), & \text{if } |\vec{r}| > R_{MT} \end{cases} \tag{1.18}$$

Since there is no approximation to the shape of the potential, this method is called "full-potential" (FP). Core levels are re-calculated at each iteration and corresponding contribution to the potential is updated. This is a dramatic difference with respect to previously mentioned techniques. In fact, it allows also to access such nuclear quantities as isomer shifts, hyperfine fields and electric field gradients.

Concerning the WF of valence electrons, it has the same form as given by Eq. (1.16) inside the MT sphere. Outside of this region the WF shows a delocalized character and is expanded in PWs (Eq. (1.17)). Such division results into a very efficient flexibility in the WF representation.

The FP-LAPW method is considered to provide the most precise modeling of the band structure. Usually the results of calculations produced with this technique are used as a reference for comparison with other DFT realizations. The price to pay is computational time: since there are less approximations, the method is more demanding. In addition, access to local quantities is not always straightforward. Projections on atoms are performed within MT spheres, so the interstitial charge density is not attributed to any site. Hence, an attention has to be payed to the choice of R_{MT}.

1.4.4 Wavelets

Wavelets is a special type of functions which was introduced in order to analyze frequency components of data. Their name already implies that wavelets must look like local perturbations which starts at some point, oscillates with finite amplitude and then

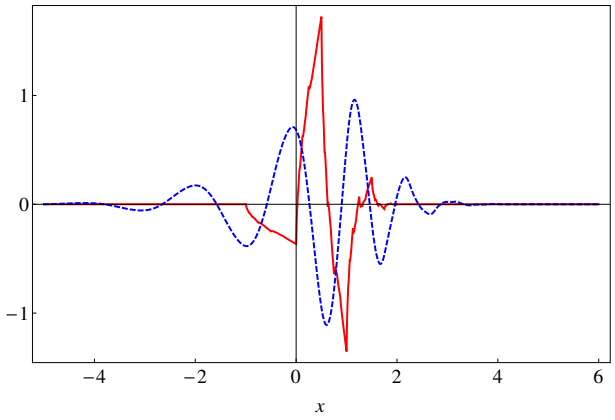


FIGURE 1.1: Daubechies wavelet functions of order 2 (red line) and 8 (blue dashed line).

attenuates back to zero. Indeed, the shape of these functions reminds particle wave packets from the course of quantum mechanics.

All families are characterized by two fundamental functions in wavelet theory, which are the scaling function $\phi(x)$ and the wavelet $\psi(x)$[4].

Fig. 1.1 shows the 2-nd and 8-th order wavelets from the Daubechies family [31]. It is clearly seen that the support length (i.e. an interval where functions are nonzero) widens as the order of wavelets increases. The most important property of wavelet families is that their degrees are in relation. Namely, the functions $\phi(x)$ and $\psi(x)$ are defined in such a way that they obey so-called refinement relations:

$$\begin{aligned} \phi(x) &= \sqrt{2} \sum_{j=1-m}^{m} h_j \phi(2x-j) \\ \psi(x) &= \sqrt{2} \sum_{j=1-m}^{m} g_j \phi(2x-j), \end{aligned} \tag{1.19}$$

where h_j and g_j are the elements of a filter that characterizes the wavelet family, and m is the order of the wavelet family. In fact, there is no analytical expression for wavelets, but components of these filter coefficients can be computed exactly, so they are tabulated. Depending on the form of $\{h_j\}$ and $\{g_j\}$, wavelets can be be either orthogonal, biorthogonal or semiorthogonal. In orthogonal wavelets families the following relations

[4]Not to be mixed with WFs

between filter coefficients take place:

$$\begin{aligned} g_j &= (-1)^j h_{-j+1}, \\ \sum_l h_{l-2i} h_{l-2j} &= \delta_{ij}, \\ \sum_l g_{l-2i} g_{l-2j} &= \delta_{ij}, \\ \sum_l g_{l-2i} h_{l-2j} &= 0. \end{aligned} \tag{1.20}$$

Eq. (1.19) together with (1.20) establishes correspondence between the scaling functions on a discretized grid of spacing h and another one of spacing $h/2$. All wavelets properties can be obtained from these expressions. The entire basis set can be built from all possible translations of the mother function centered at the origin by a certain grid spacing h. The mother function is localized and has relatively compact support.

As we have seen, wavelets form a smooth basis set that is localized in both direct and reciprocal space. Thanks to these unique properties, they are of great potential applications. Wavelets have recently became a useful tool for solving differential equations [61]. Since such type of mathematical problems appears almost everywhere, wavelets enter more and more fields of nowadays research.

Just a few years ago an efficient method for solving Poisson equation in different BCs, based on the wavelet-like functions, was suggested[57, 58]. Soon after wavelets were already applied to realistic band structure caculations. Daubechies family as a basis set are incorporated with the PSP formalism and realised in the `BigDFT` code [59], which will be used in the present thesis.

The primary merit of this approach is an ability to treat systems with different BCs on equal footing. For example, in case of surface BCs one direction, say y, is isolated while two others are periodic. In majority of the DFT codes the modeling of such system would require an enlargement of the unit cell in y-direction, preserving its periodicity. Thus the system becomes well-separated from its y-translated replica. But the simulation box has to be extremely large to ensure the cancellation of the long-ranged Coulomb interactions. Hence, an explicit treatment of mixed BCs becomes very advantageous from computational viewpoint. Moreover, charged systems can be treated without introduction of an artificial compensating background, as done, for example, in Ref. [111].

In addition, the code is young, massively parallelized and shows fair performance on nowadays computers [60].

1.5 Drawbacks of DFT-based methods

In previous section a brief overview of several realizations of the DFT was made. Some of them are more accurate than the others due to the presence of approximations to the ionic potential.

However all codes share the same drawbacks which arise from the basic DFT formalism. For instance, there is an intrinsic problem of self-interactions. Since all electrons contribute to the Hartree term, it leads to the unphysical consequence that each electron is affected by the field which is partially produced by itself.

Another shortcoming of this technique is that it provides only with the GS at zero temperature ($T = 0$). But in reality we have to deal with materials at finite temperature, thus the lowest state gets mixed with excited ones, like in Boltzmann's ansatz. Unfortunately, there is no direct access to excited states in the present framework. Moreover, the information about higher-lying states is essential, since most often in an experiment the system under consideration is subjected to some perturbation and gets excited from its GS. Post-DFT approaches like time-dependent DFT (TD-DFT)[143] and the *GW* method[80] were suggested in order to overcome this problem. They are on the level of development.

A serious problem of the DFT is the lack of the many-body (correlation) effects. In the present approach the electrons experience *the same* average potential which depends on total electron density solely. The corresponding Hamiltonian can be diagonalized resulting in a set of independent particles moving in some MF. In the context of the Hubbard model[79], it means that only the band term (containing hopping) is present. The four-particle (i.e. coupling) term which is responsible for the multiplet structure formation and atomic-like behavior is completely omitted within the DFT formalism.

For strongly correlated systems these effects dramatically affect the band structure and therefore the DFT can not provide an accurate model for them. This is exactly the case, for instance, in transition metal oxides and unconventional superconductors like cuprates

and pnictides. Nowadays there are several techniques exist, able to go beyond conventional DFT and include some part of correlation effects. Among such approaches the most widely-used are LDA+U [5] method and a conjunction of the DFT and Dynamical Mean Field Theory (DFT+DMFT) [97].

There is another drawback of the conventional DFT which is important for magnetic systems. It is the well-known problem of underestimation of orbital magnetism [26, 28]. There are at least two ways to improve these assessments: the already mentioned LDA+U and the orbital polarization (OP) [20, 44, 45] techniques. The first one, taking into account part of local correlations, essentially leads to electron localization, which usually results into an augmentation of local quantities like spin and orbital moments. Within second approach an additional term to the Hamiltonian, which reflects the second Hund's rule, is introduced. Both methods require some *ad hoc* parameters, even though the possibilities of *ab initio* determination of them were proposed [45, 70].

In the context of the present work it was already mentioned that the DFT provide quite detailed description of transition metals band structures. However, the drawbacks have to be kept in mind while using this technique to study new classes of materials, where *a priori* knowledge is missing.

1.6 Practical applications of the DFT formalism

Using the DFT it is possible to simulate vast amount of physical and chemical properties of the matter. The aim of the present work does not imply to cover the whole spectrum of its applications, so we will restrict ourselves to few classes.

Since the present work concerns the properties of transition metals under extreme pressures, we will be interested in seeing how stress affects electronic and crystal structure of particular systems. Transition metals mainly attract attention of physicists because they exhibit spontaneous magnetism, so the pressure evolution of their magnetic properties should be studied as well.

In the following paragraphs it will be explained in more detail how structural and magnetic properties of solids can be studied by means of the DFT calculations.

1.6.1 Structural properties

A problem of finding an atomic configuration corresponding to the *local* minimum of the total energy is very important in the context of *ab initio* simulations. These methods can shed light on real physical origins of a certain crystal structure formation and relate it to electronic and magnetic properties of the compound. For example, according to the Stoner model the appearance of spontaneous magnetization tends to decrease system's equilibrium volume [156]. And first-principles calculations based on the DFT are able to reproduce this physics together with a detailed description of the band structure. However, the so-called structural optimization problem is not always straightforward to solve.

If a periodic system is characterized by one atom per unit cell one can identify few degrees of freedom related with the change of the lattice vectors, i.e. the shape and the volume of a cell. For example, if the symmetry is cubic then the problem becomes easy and has an intuitive solution with the help of the DFT simulations. Namely, one can just vary the lattice constant in order to find the value which corresponds to the energy minimum.

On the other hand, if we consider a system with several atoms per unit cell, the problem becomes much more complicated. The number of degrees of freedom is too high and the "random walk" in these variables is not efficient at all. Instead, thanks to the use of Hellman-Feymann theorem [50], local forces acting on each atom within unit cell can be directly extracted from the calculation. Then the atomic positions can be moved in the direction of the forces (if a used method does not restrict it). After each displacement the density has to be re-calculated to reach self-consistency. In practice few such interactions are enough to find an optimal atomic configuration.

An optimization of geometry of the unit cell requires another quantity as a source of information and is treated differently. For this purpose a quantity called "stress tensor" has to be computed [124–126]. To introduce it, let us consider a general transformation of particles coordinates in a quantum system due to space deformation:

$$r'_{i,\alpha} = r_{i,\alpha} + \sum_{\beta} \varepsilon_{\alpha\beta} r_{i,\beta}, \tag{1.21}$$

where i numerates the particles, $\{\alpha, \beta\} = \{x, y, z\}$ are projections on Cartesian axes and $\varepsilon_{\alpha\beta}$ is a so-called "strain tensor", which in the present context describes deformation of the lattice.

In spirit of the linear response theory, the stress tensor $T_{\alpha\beta}$ is defined as a variation of the total energy with respect to infinitesimal perturbation governed by $\varepsilon_{\alpha\beta}$:

$$T_{\alpha\beta} = -\frac{\partial E_{tot}}{\partial \varepsilon_{\alpha\beta}}. \tag{1.22}$$

Hence $T_{\alpha\beta}$ describes the reaction of the system on certain changes of the lattice. The trace of T defines internal pressure (i.e. $P = \frac{1}{3}\sum_{\mu} T_{\mu\mu}$) and shows preferable direction for the change of the volume of the unit cell. Off-diagonal terms are responsible for shear deformations. In general, stress tensor has 9 components, but only 6 are independent due to the space isotropicity. Moreover, the symmetries of the crystal structure relate different components of the tensor. As an example, in the most symmetrical case, i.e. cubic symmetry, the only one independent component remains, i.e. $P = T_{xx}$. In equilibrium, internal stresses disappear, so all components of $T_{\alpha\beta}$ should vanish. While in order to obtain the structure corresponding to a given external (hydrostatic) pressure P_{targ}, one should aim to reach the following relation: $T_{xx} = T_{yy} = T_{zz} = P_{targ}$.

In general, the structural optimization has to be done in two steps. A good way of doing it is to start from experimental structure and minimize interatomic forces. Once it is done, the stress tensor can be used to adjust the geometry of the lattice. It is worth emphasizing that the predicted structure depends on the choice of XC potential. If the chosen approximation does not properly describe the GS band structure, there is, in principle, no reason to rely on the results for structural properties (see e.g. [162]).

1.6.2 Magnetism: Mapping on the Heisenberg model

As was already mentioned (2), there are two major models in modern theory of magnetism: Heisenberg and Stoner ones. In spite of the fact that Stoner mechanism is well reproduced within the DFT [68], this model does not provide an adequate explanation of finite-temperature magnetism. The Curie-Weiss behavior which is reported for nearly any $3d$ system can not be reproduced: according to the Stoner theory the magnetic moments should disappear above Curie point. Hence it is not surprising that Curie

temperatures (T_c) of transition metals estimated from density of states at Fermi level ($DOS(E_f)$) are reported to be highly overestimated [69].

Thus, if we want to get a deeper insight into magnetic properties, for instance, to get realistic prediction for T_c or probe the stability of particular magnetic state, it is more useful to use the Heisenberg model for localized spins. Indeed, such approach is not always well-justified when applied to any $3d$ metal. For example, bulk nickel possessing magnetization of $\approx 0.6\mu_B$ per atom, can be barely considered as a Heisenberg magnet. Indeed, present analysis is supposed to work better for systems like iron and cobalt alloys, which are characterized by significant magnetic moment per ion of the order of few μ_B.

A phenomenological Heisenberg Hamiltonian in one of its forms can be written as:

$$\hat{H}_{exch} = -\sum_{i \neq j} J_{ij} \vec{e}_i \cdot \vec{e}_j \tag{1.23}$$

where J_{ij} denotes the exchange integral between magnetic atoms at sites i and j, and $\vec{e}_i$ and $\vec{e}_j$ are unit vectors in the directions of the local magnetization on sites i and j, respectively. The *classical*[5] model treats magnetic moments as vectors of constant magnitude, which interact with each other via parameter J_{ij}. In present notation (Eq. (1.23)), positive J reads ferromagnetic (FM) coupling.

In real magnetic systems J_{ij}'s have several different contributions. A direct exchange given by Eq. (1.6) is only one of them. It can be either FM or antiferromagnetic (AFM), depending on the degree of overlap of two WFs. If we speak about transition metals whose magnetic moments are mainly carried by $3d$ states, this contribution should decay fast with increase of the distance between spins.

However, there are other exchange mechanisms, like superexchange due to virtual hopping from occupied levels of ligands. The sign of this coupling depends on the local geometry and on orbitals involved in the hopping processes [66]. More often superexchange mechanism results in an effective AFM interaction between spins.

[5] A quantum version of Eq. (1.23) also exists. According to the basic laws of quantum mechanics, one has to substitute magnetization vectors by corresponding operators.

Conduction electrons are also able to mediate magnetic interactions. Due to their high mobility, $J_{ij}(|\vec{r}|)$ can become a rather long-ranged function, having an oscillatory character such that couplings of both signs (FM/AFM) can appear between different pairs. Current mechanism is called Ruderman-Kittel-Kasuya-Yosida (RKKY) [142] interaction and is very common in metallic systems.

Other effective interactions such as "kinetic" or "double" exchange can be also important in the context of $3d$ metals and their alloys. A book by Fazekas[49] gives a brilliant overview of different exchange mechanisms and explains in detail how they can be derived from many-body Hamiltonians.

Thus J_{ij} is the key quantity of present theoretical method, but in practice has a rather complicated structure with several contributions. Different impacts compete with each other and therefore it is rather difficult to predict even a sign of the total interaction.

It was shown by Lichtenstein *et al.*[105] that there is a way to extract J parameters from the GS DFT calculation.

The primary idea of the suggested approach is to consider an infinitesimal rotation of the spin i on angle θ and then write second variation of the total energy with respect to this perturbation. Starting from the FM state from Eq. (1.23) one obtains:

$$\hat{H} = -\sum_{i \neq j} J_{ij} |\vec{e}_i| \cdot |\vec{e}_j| \cos\theta \approx -\sum_{i \neq j} J_{ij} + \sum_{i \neq j} J_{ij} \frac{\theta^2}{2}. \tag{1.24}$$

Then the same procedure has to be performed on a real spin-polarized Hamiltonian, which comes from converged DFT calculation. Projected on atomic states Hamiltonian can be expressed in the matrix form as $\hat{H}^{\sigma\sigma'}_{ijmm'} =< im'\sigma'|\hat{H}|im\sigma >$ where i denotes site, m is magnetic quantum number and $\sigma = \{\uparrow, \downarrow\}$ is electron spin projection. It is also useful to formally define the corresponding Green's function as $\hat{G}(z) = (z - \hat{H})^{-1}$. Such quantities are more easily accessed within LMTO formalism which is the most widely-used approach for such type of studies.

In terms of electronic Hamiltonian the above-mentioned transformation corresponds to an application of the following operator:

$$\hat{U} = \exp\left[i\vec{\theta} \cdot \hat{\vec{S}}\right] \approx 1 + i\vec{\theta} \cdot \hat{\vec{S}} - \frac{1}{2}(\vec{\theta} \cdot \hat{\vec{S}})^2, \tag{1.25}$$

where $\hat{\vec{S}} = \frac{\hat{\vec{\sigma}}}{2}$ and $\hat{\vec{\sigma}} = \{\hat{\sigma}_x, \hat{\sigma}_y, \hat{\sigma}_z\}$ is a vector of Pauli matrices.

Using "local force theorem" [129], which states that variation of the total energy with respect to to some perturbation (δE) is a sum of changes in one-electron energies, it can be shown that for small values of θ there is an exact mapping of real electronic Hamiltonian on the Heisenberg one. So one obtains the same form of variation as given by Eq. (1.24), where intersite exchange J_{ij} is expressed in terms of band structure quantities:

$$J_{ij} = \frac{1}{4\pi} \Im \int_{-\infty}^{E_f} \mathrm{Tr}_{\{m\}} (\Delta_i G_{ij}^{\uparrow} \Delta_j G_{ji}^{\downarrow}) dz. \tag{1.26}$$

Here $\Delta_i = (\hat{H}_{ii}^{\uparrow} - \hat{H}_{ii}^{\downarrow})$ is an exchange potential on the i-th site and G_{ij}^{σ} is a matrix of intersite Green's function, which describes propagation of an electron with spin σ from site i to j. Here z is a complex energy variable of the form $E + i\epsilon$. Integration has to be performed over z, in order to avoid poles of the Green's function.

Suggested approach allows to compute exchange integrals between any pair of spins in a real magnetic system, assuming that the DFT provides a correct description of its electronic structure. This approach was applied to series of transition metal alloys and provided nice estimations of T_c as compared with experimental data [56, 74, 130]. In practice it turns out that the agreement is better for compounds with larger values of magnetization. This is understandable, since the squared magnitude of a quantum spin S is $|S|^2 = S(S+1)$, while in classical Heisenberg model it equals S^2. Both these expression coincide in the case of infinitely large spin S, meaning that the larger the spin value the closer its behavior to the classical one. This gives an idea about the range of application of Lichtenstein's approach.

It has to be emphasized that calculated J-parameters are extracted from the GS with a certain (assumed) magnetic order. Therefore these parameters are not universal quantities and in principle there is no guarantee that extracted from different reference states values will coincide.

However this information can be useful for studying the stability of a particular magnetic state. For this purpose obtained J's can be used to find low-energy magnetic excitation (i.e. frozen magnon) spectra [130].

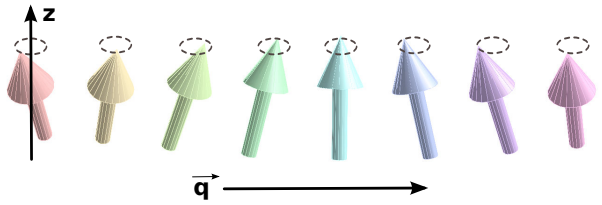


FIGURE 1.2: Schematic representation of a frozen magnon. Arrows show the direction of local magnetization, which is initially aligned along Z axis.

1.6.2.1 Frozen magnons simulations

Magnons or spin waves (SWs)[6] are quasiparticles representing a certain type of excitations in the spin density. They can be seen as infinitesimal deviation of one spin's orientation which then propagates through the entire periodic system with a given wavevector $\vec{q}$. Real SWs are observed in inelastic neutron scattering (INS) experiments and provide information about system's dynamical magnetic susceptibility $\chi(\omega, \vec{q})$.

In the framework of "frozen magnons" there is no *real* motion. Imagine that we take a snapshot of a SW at a certain time – it will look like a spin spiral with small transverse components, as shown on Fig. 1.2.

This is a valid representation of real magnons in adiabatic limit, i.e. when spin dynamics is defined on a much shorter time-lengths than changes in the electronic potential energy. Indeed, one of the possibilities to model SWs is to directly calculate the total energy of such spin spirals. This can be done with the help of generalized Bloch theorem [146].

We will follow another strategy and use extracted J_{ij} parameters. For this purpose we consider a simple gyroscopic equation of motion which governs SW dynamics:

$$\frac{d\vec{S}_j}{dt} = -\frac{1}{\hbar}\left[\vec{B}_j \times \vec{S}_j\right], \tag{1.27}$$

where $\vec{S}_j = |S_j|\vec{e}_j$ is a vector of the magnetic moment located at the position $\vec{R}_j$; $\vec{B}_j$ is an effective field acting on the corresponding spin, which appears from the spin Hamiltonian :

$$\vec{B}_j = -\frac{\partial \hat{H}}{\partial \vec{S}_j}. \tag{1.28}$$

[6]This term must be distinguished from the spin density waves (SDW), which are related to the modulation of the spin density. SDW does not imply systems's excitation.

In the simplest case of FM system containing one magnetic atom per unit cell and described by Heisenberg Hamiltonian (Eq. (1.23)) it is easy to show that energies of spin waves propagating with wavevector $\vec{q}$ are given by:

$$E(\vec{q}) = \frac{4\mu_B}{|S|} \sum_{j \neq 0} J_{0j} \left[1 - \exp\left(i\vec{q} \cdot \vec{R}_j\right) \right] \tag{1.29}$$

Eq. (A.1) can be generalized for the case of several magnetic sublattices and different their arbitrary orientations. A detailed derivation of the corresponding formulas is given in the Appendix A. In these cases one has to deal with a linear system of coupled equations, which solution will give few branches of spin waves. One of them will necessarily possess the following property: $\lim_{q \to 0} E(q) = 0$. This is a so-called "Goldstone" mode which is responsible for low-energy excitations, we will be interested in. Appearance of negative/imaginary eigenmodes in this mode will indicate instability of the assumed magnetic order.

In this thesis the calculation of SWs Goldstone mode will be performed for certain magnetic alloys. Note that higher-lying ("optic") modes will not always be shown in present work since it is out of the scope of the study. In reality, these branches will be considerably attenuated due to presence of another type of spin excitations called "Stoner excitations". They appear when majority-spin electron jumps to unoccupied spin-down state. This process requires to flip the spin and, therefore, costs some finite energy of the order of intra-atomic exchange ~ 1 eV.

1.7 Conclusions

In this chapter we have introduced the standard methods, which are used for first-principles modeling of the electronic structure in solids. It has to be emphasized that the DFT is an exact theory. Yet, its realizations should be called "*ab initio*" with certain provisos. Within this theory, there is a choice of the XC potential which implies some approximations. For many systems these approximations are acceptable and the method can be used to investigave microscopic mechanisms, which define the overall system's behavior.

It is a powerful and widely used tool in nowadays condensed matter physics. In the next chapters we shall see how the present theory can be applied to study magnetic and structural properties of various $3d$ metal-based systems.

Chapter 2

K-edge XMCD study of transition metals under high pressure

2.1 Introduction: experimental technique

It was Faraday who first pointed out peculiarities in the interaction between a light and magnetized matter [48]. He discovered that if a sample is exposed to a magnetic field, shining a linearly polarized light in the direction of the field on it causes rotation of the corresponding polarization vector. Later Kerr found the same phenomenon for a reflected light, which permitted to the observe domain structure in ferromagnetic compounds (see e.g.[169]). These findings opened a new branch of effects called "magneto-optical" and since then their number increased dramatically. Nowadays they are one of the primary tools to study magnetic materials.

Magneto-optical experiments were initially carried out using solely the visible light. However, the same phenomena take place for other parts of the spectrum of electromagneti radiation. And the biggest achievements in this field are related with the use of x-ray photon energies.

The main merit of x-rays is the element-selectivity. A simple estimates for hydrogen-like atom show that energy of $1s$ level of an element with atomic charge Z should be

proportional to Z^2 [16]. Therefore, absorption edges[1] of all atomic species are well-separated in the absolute energy scale. Corresponding energies for the majority of elements from periodic table fall into the range, which is covered by soft and hard x-ray regimes[2]. Thus exposing a sample to the x-ray beam of a certain wavelength permits to investigate the states of this particular element and not the others.

In terms of absorption of electromagnetic waves, there is an interesting magneto-optical effect: magnetic samples absorb the light with right and left circular polarization (RCP and LCP) differently. The effect is called Magnetic Circular Dichroism (MCD). Its manifestation in x-ray regime (XMCD) was predicted theoretically by Erskine and Stern [47] for $M_{2,3}$-edges of Ni. However, the first experimental confirmation of the XMCD effect was obtained more than ten years later by van der Laan *et al.* [164].

It can be shown that the change of incident light helicity is equal to the invertion of magnetic field direction, since both operations have a meaning of the time inversion. So the XMCD signal is defined by taking the difference between X-ray absorption spectra measured with parallel and antiparallel (μ^+ and μ^-, respectively) orientations of the magnetization with respect to beam helicity:

$$\mu_{XMCD}(\omega) = \mu^+(\omega) - \mu^-(\omega). \tag{2.1}$$

The pioneering experimental study of the XMCD in transition metals was performed by Schütz *et al.* [149] at the K-edge of iron. However, the biggest challenge was to address $L_{2,3}$-edges, since the final state of this process is in $3d$ shell, where main magnetic properties come from. Chen *et al.* [29] were the first who succeeded in carrying out such experiment on pure nickel. Since few years after this work the XMCD has already become one of the most widely-used tools to probe orbital magnetism [139]. Using this technique one is able to resolve different contributions to spin and orbital magnetizations originating from inequivalent atomic species (see e.g. Ref. [38]).

[1] This is the energy which is needed to move an electron from corresponding bound state to the continuum. Notations $K, L_1, L_{3,2}$ mean that $1s, 2s, 2p$ electron levels are, respectively, involved.

[2] Soft x-rays are usually called the ones whose energies are in the region between 0.1 and 1 keV, e.g. $L_{2,3}$-edges of $3d$ metals. Hard x-rays regime is in between 1 and 10 keV, e.g. K-edges of the same class of elements

In nowadays x-ray experiments an achievement of ultra-high pressure is possible thanks to the use of diamond anvil cells (DACs). This is one of the hardest and least compressible materials on the Earth. DAC allows us to reach pressures of the order of Mbar (∼100 GPa). Moreover, its another advantage is transparency with respect to a big fraction of electromagnetic waves; so it does not affect measured spectra. However, characteristic energies of $L_{3,2}$ edges of $3d$ metals are exceptions in this list. And diamond's opacity is the main reason why spectroscopic measurements with DAC are made at the K-edge of transition metals. It is still an element-specific tool, but the final state is not in a localized $3d$ shell. This fact complicates data interpretation and this issue will be addressed in the next section.

2.2 Theoretical interpretation of XMCD spectra

The easiest way to quantitatively understand the XMCD effect is to look on a photon as a bosonic particle with angular momentum quantum number $L = 1$ (in units of $\hbar$)[3]. As usual, we can choose a certain quantization axis, which in our case is along propagation direction, and define projection of L on this axis, called L_z. It can be shown that $L_z = 1$ corresponds to the RCP of a wave and $L_z = -1$ – to the LCP. Let us consider a pure $3d$ metal. If a photon undergoes an elastic collision with $1s$ ($L = 0$) electron, conservation of the total momentum implies that final state of electron will be different, solely depending on the "handedness" of incident light. Of course, total $\langle L_z \rangle$ should be non-zero in the final state, which is $4p$ level in this particular case. If it was not the case, no dichroism would be observed. Any features in the XMCD spectrum clearly shows presence of non-zero orbital moment, i.e. breaking of time-reversal symmetry.

One has to make one step forward and state that the presence of $\langle L \rangle$ implies non-zero spin magnetization. Opposite situation is not known to be realized in nature. Thus, by looking on K-edge XMCD data, we can clearly judge whether the system is ferromagnetic or not.

Total orbital moment in transition metals is much smaller than the one predicted by Hund's rules: it is efficiently quenched by the crystal field. It means that in resulting wavefunctions $\{d_{xy}, d_{xz}, d_{yz}, d_{z^2}, d_{x^2-y^2}\}$ the angular momentum components $Y_{l,\pm m}$ are

[3] In fact, it gives an intuitive justification of a dipole-selection rule: $\Delta l = \pm 1$, widely used for interpretation of x-ray spectra

mutually compensated[4]. For example, in fcc Ni its value is about $0.05\mu_B$ [3]. The quenching is not complete mainly thanks to spin-orbit coupling (SOC) in the d-shell. Spin-orbit coupling constant for these states is estimated to be of the order of $\sim$0.05 eV. If we look on SOC as a perturbation to crystal field potential, then current value defines the bare energy scale of energy levels shifts associated with this interaction. SOC partially lifts the degeneracy of $Y_{l,m}$ and $Y_{l,-m}$ states and gives rise to a finite L_z. Since d bands are strongly hybridized with p levels, the latter also gets spin- and orbitally-polarized. This is a physical origin of magnetic signal observed in K-edge XMCD experiments on transition metal.

Quantitative understanding of XMCD in realistic systems is usually based on the use of the so-called "sum rules". These expressions allow us to estimate real values of spin and orbital moments in μ_B right from the measured spectra. Sum rules for different edges and light polarizations were derived by several authors [25, 158, 170]. In most cases formula derivation was based on atomic multiplet theory. This is certainly an appropriate model of f-states in rare-earth materials, where degree of localization is relatively high, so the electronic structure is well described in the atomic limit. Indeed, in this case atomic multiplet approach is able to reproduce experimental data rather well.

The situation, described above, is very different from $3d$ metals, where itinerant electron picture is more appropriate one. As was already mentioned, $3d$ states are strongly affected by crystal field and hybridization effects. Thus the modeling of experimental data should be based on a detailed description of the band structure. Present philosophy was used by Ebert *et al.* who initialized an approach to simulate XMCD spectra using outcomes of relativistic DFT calculations [39, 40]. Yaresko and co-workers implemented similar technique within LMTO formalism and applied it to various transition-metal compounds [8]. In spite of the fact that experimental quantities became accessible, there are some intrinsic problems in the GS, like orbital moments underestimation (mentioned in Chapter 1), which have to be remembered.

It was reported that the use of the sum rules is still appropriate for $L_{2,3}$-edge studies on $3d$ metals [28], since d-levels are rather well-defined with the dispersion of the order of

[4] In each cubic harmonic $Y_{l,\pm m}$ appear solely in pairs, preventing appearance of a finite L_z value

≈5 eV. On the other hand, the K-edge data are more tricky to analyze, since the final state is in a broad $4p$ band.

One of the first attempts to understand K-edge XMCD of pure $3d$ metals was made by Ebert and co-workers [39]. Igarashi and Hirai [81] developed a tight-binding-based method for calculating XMCD probabilities, where spin-orbit coupling was treated as a perturbation. They were the first who showed numerically that the spin-polarization of the d levels is the primary origin of XMCD signal in the present case. Later Guo [71] derived an expression for the K-edge sum rule, which looks the following way:

$$\frac{\int_{E_f}^{E_c} d\omega \left[\mu^+(\omega) - \mu^-(\omega)\right]}{\int_{E_f}^{E_c} d\omega \mu^0(\omega)} = -\frac{3\langle L_z\rangle_p}{n_p^h} \tag{2.2}$$

where n_p^h is the number of holes and $\langle L_z\rangle_p$ is p-projected ground state orbital moment. E_f and E_c are Fermi and cut-off energies, respectively. Cut-off is determined in a such way that XMCD intensity must not have any features above this energy.

Above-mentioned formula is rigorous upon few approximation. One of them is a neglect of quadrupole transitions ($1s \rightarrow 3d$). Otherwise, a relatively small admixture of d-orbital moment should be added to the right-hand side. However, previous results for fcc Ni reassured that dipole approximation is quite appropriate for pure transition metals.Among other approximations the most rude one is assumption of energy-independence of transition matrix elements of the type: $\langle 1s|\hat{r}|4p\rangle$. This is quite far from reality for the case of highly delocalized $4p$ bands.

Therefore it is quite difficult to extract absolute quantitative information on the magnetic moment from the K-edge XMCD spectra.

2.3 Bulk Ni: an example of persistent ferromagnet

Ni is a nice case study for magnetic properties investigation. It is a "strong" ferromagnet[5], meaning that its majority d-levels are fully occupied and the DOS(E_F) has only contributions coming from spin-down electrons. This class of magnets is characterized

[5]For this classification, consult Ref. [120]

by a small susceptibility and very stable magnetic moment with respect to a change of external parameters.

Moreover, Ni is crystallized in the closed-packed fcc structure. Opposite to the cases of bcc iron and hcp Co, which exhibit pressure-induced structural transitions along with magnetic ones, Ni persists its structure up to very high pressures [33]. Therefore, Ni's case allows us to reduce amount of degrees of freedom and investigate solely how lattice constant contraction affects its electronic and magnetic properties. It gives an ideal opportunity to check the very theory of band magnetism.

An x-ray absorption spectroscopy (XAS), XMCD and x-ray diffraction (XRD) measurements using DAC were made on the beamlines ID27 and ID24 at the European Synchrotron Radiation Facility (ESRF). The data obtained for polycrystalline Ni sample is shown on Fig. 2.1.

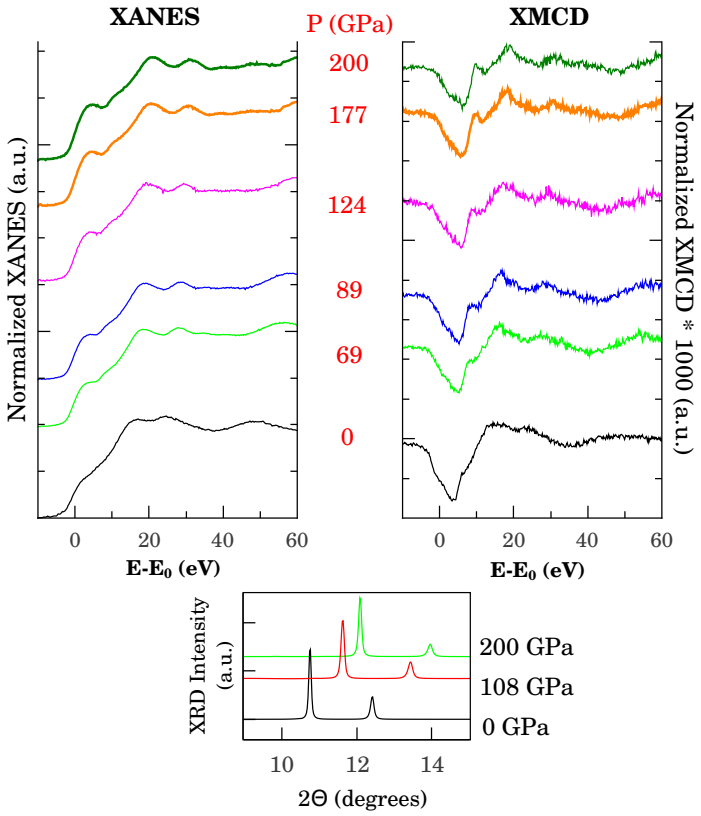


FIGURE 2.1: Upper panel: XAS (left) and XMCD (right) spectra in compressed Ni. (E_0 = 8323 eV). Lower panel: selected angle-dispersive XRD patterns, showing no structural changes up to maximal pressure considered.

First of all, one clearly sees that both XAS and XMCD curves do not change significantly upon sample's compression. A global shift of features in high-energetic region of XAS

spectra corresponds to the change of interatomic distances. Neither structural, nor magnetic transitions were observed, as suggested by the obtained data. There is a gradual decay of peak intensities in XMCD signal, while its overall shape remains the same for the entire pressure range. We can conclude that Ni is ferromagnetic under applied pressure at least up to 200 GPa.

As was already mentioned, quantitative information on a sample's magnetic state is more difficult to extract, since the K-edge XMCD signal does not probe total spin magnetization directly.

In order to understand the results of experiments, we have computed differential XMCD signal of Ni with the help of `PY-LMTO` [8] code, defined as:

$$d_{XMCD}(E) \equiv \sum_{n\mathbf{k}} \left[|\langle \Psi_{n\mathbf{k}} | \Pi^{+} | \Psi_{1s} \rangle|^2 - |\langle \Psi_{n\mathbf{k}} | \Pi^{-} | \Psi_{1s} \rangle|^2 \right] \delta(E - E_{n\mathbf{k}}) \tag{2.3}$$

where $\Pi^{+(-)}$ is the dipole interaction operator of an electron with a photon of right(left) helicity ; sum goes over bands and k-points from the first BZ.

The comparison of the present quantity with $p-$projected orbital magnetization density $dm_l(E) = d\langle L_z \rangle / dE$ is shown on Fig. 2.2.

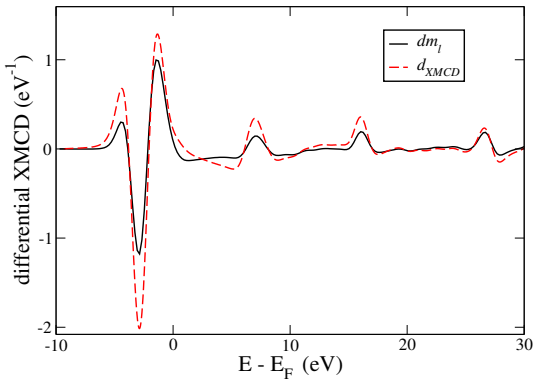


FIGURE 2.2: Calculated orbital magnetization density of $4p$ states and the K-edge differential XMCD for bulk Ni (ambient pressure)

The similarity between these quantities, which is mainly due to smooth energy dependence of transition matrix elements [9, 67], allows us to assume that integrated K-edge XMCD signal[6] can be expected to be proportional to the $p-$orbital moment and their evolution with pressure can be compared.

[6]Integration of XMCD spectrum has to be done in the region, sensitive to the electronic structure (close to the edge). At higher energies the behavior is governed by local atomic structure

In order to check this, we carried out a series of first-principles calculations of the $l-$projected orbital and spin contributions to the total magnetization for different unit cell volumes of bulk Ni. Two implementations of the DFT were used: `PY-LMTO` and `WIEN2K` [14], which realized FP-LAPW method. In both codes the SOC is added to the Hamiltonian through so-called second-variational method[7] [37, 109]. We benefit from the use of present approach, since it permits to artificially "turn off" SOC on certain orbitals. This information can be useful for understanding the origin of magnetic moments.

To verify the dependence of the results on the choice of XC-potential, we have performed series of calculations using several functionals [135, 136]. However, all results appeared to be in the same trend.

It has to be mentioned that in spite of a common difficulty in predicting orbital magnetism, the DFT-based calculations in LSDA provide a fair estimate for Ni, slightly underestimated by not more than 5% [26, 46].

The outcomes of our calculations are shown on Fig. 2.3. The results are in good agreement with previous theoretical simulations and experiments [46, 81, 86, 119, 174].

The results indicate that, as the pressure is raised, the total spin moment first decreases slowly, but from a certain pressure value onwards a fast attenuation begins, presumably indicating the violation of the Stoner criterion. Interestingly, the p and d orbital moment components show a different dependence with respect to the total spin magnetization. Although the decay rates of the moments are not the same, they all quench simultaneously which is not surprising, as they are all induced by spin polarization of the $d-$bands, i.e. the $d-$spin moment.

Some deviations in the absolute values of the magnetic moments can be due to different definition of MT spheres (see Chapter 1). The discrepancy between the predicted values of FM-to-nonmagnetic transition provided by different implementations is presumably due to the approximations to the potential made for the LMTO method. However, one has to be cautious with the latter estimates, since DFT models the ground state at zeroth temperature. In reality it is not excluded that the T_c will decrease with pressure and at some point will drop below the room temperature. Thus, if one studies stability

[7] A set of independent fully-relativistic calculations, based on the non-perturbative treatment of SOC effects, as appears in the Dirac equation, was also performed. However, we report no differences with respect to the results obtained with second variational technique.

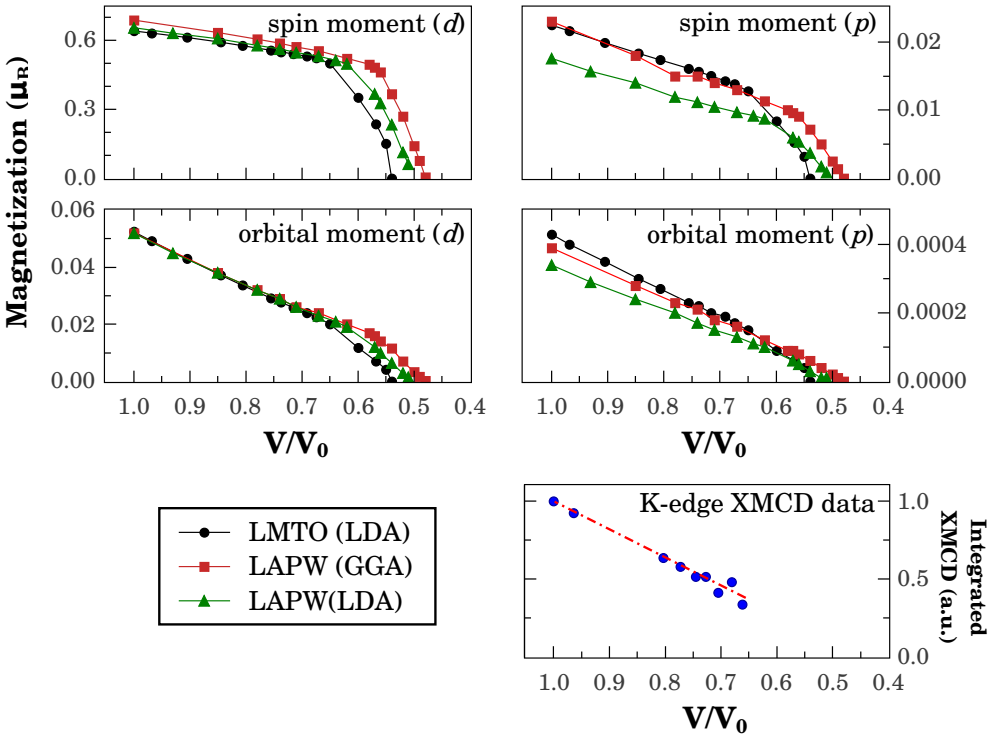


FIGURE 2.3: Volume evolution of different calculated components of Ni magnetization along with normalized integrated XMCD signal. V_0 reads experimental equilibrium volume. Note that absolute values are plotted; S_p is antiparallel to S_d.

of different phases, then both external parameters (P and T) have to be controlled simultaneously during the experiment.

According to our results, for values of the relative compression V/V_0 ranging from 1 to 0.66 (corresponding to the experimentally applied pressure values up to 2 Mbar) the total spin magnetization decreases by roughly 20%, while the $p-$ and $d-$orbital moments fade by 60% as does the integrated K-edge XMCD signal (Fig. 2.3).

Constrained calculations revealed that $p-$orbital moment originates from SOC on $3d$ and $4p$ levels. Opposite to the results of previous calculations, we report that the latter impact is not negligible: it contributes approximately 35% of overall magnitude of the moment at ambient pressure, while at relative compression rate of 0.66 it reaches 50%.

In general, this yields an interesting result that the integrated K-edge XMCD signal closely follows $\langle L_z \rangle_p$, the pressure behavior of which is different from the one of total spin moment. Whereas the latter was usually used to interpret this type of measurements [82, 84].

The article which contains these results is published in the journal *Physical Review Letters* [160].

2.4 Orbital magnetism in hcp Co under pressure

Next, a similar analysis was conducted on bulk cobalt. It is known that the FM hcp phase is stable against applied pressure. A martensitic-type hcp-fcc transition appears to be sluggish and is spread in the region between 100 and 150 GPa [175]. According to several theoretical predictions, the low-volume phase has to be non-magnetic [82, 118, 144]. An interesting behavior of elastic and vibrational properties as a function of pressure was reported for this system [6, 7, 63].

Recently two experimental groups performed high-pressure XMCD measurements on pure cobalt [83, 161]. Obtained data are depicted in Fig. 2.4.

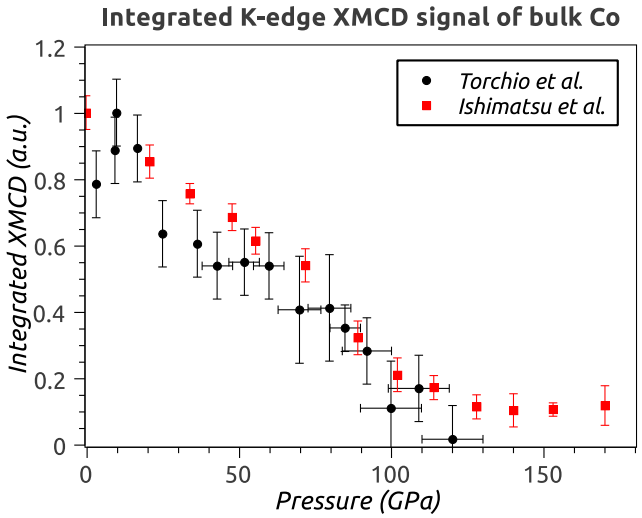


FIGURE 2.4: Pressure evolution of normalized integrated XMCD signal measured at the K-edge of bulk Co. Data is taken from Ref. [83, 161].

Results reported by two groups are similar for the low-pressure hcp phase, but high-pressure data are in contradiction. Ishimatsu *et al.* suggest that fcc phase is paramagnetic with anomalously large susceptibility, while Torchio and co-workers report a complete disappearance of a magnetic signal. Present issue is still under debate. However, it was clear that pressure evolution of integrated XMCD signal does not follow that of total spin magnetization. The latter is predicted to decrease much slower in a volume range close to equilibrium.

First, we have modeled the phase diagram by comparing total energies of magnetic and non-magnetic crystal structures. Present set of calculations was carried out in the `VASP` code, using GGA (Perdew-Burke-Ernzerhof [PBE][135]) functional. In agreement with prior studies, ferromagnetic hcp Co is predicted to undergo an hcp-fcc transition at approximately 100 GPa. Its fcc phase loses magnetization at lower pressures (≈80 GPa), which is a *virtual* transition, and in reality one obtains a non-magnetic fcc phase, as suggested by XMCD measurements by Torchio *et al.*

Next, we have investigated various contributions of the total magnetization, and tried to relate XMCD results with the outcomes of first-principles calculations. For present study the simulations were conducted using `WIEN2k` [14] code. Following the approach by Antonangelli *et al.* [7], we obtained c/a ratio which corresponds to the minimum of the total energy for a fixed volume of the cell.

Opposite to the case of Ni, d-orbital moment of hcp Co is strongly underestimated in the conventional DFT [26, 28, 46]. In order to improve this, we applied OP correction to the d-states, as implemented in `WIEN2k` code. Results obtained with GGA and GGA+OPC schemes for various compressions of the unit cell are shown in Fig. 2.5.

It is seen that spin moments are barely modified by the presence of the OP term. Whereas orbital moments are strongly enhanced, providing results which are in better agreement with ambient pressure estimates. However, their collapse is predicted for the same value of pressure. This is predictable, since the magnitude of the OP correction is in proportion to the orbital moment itself. Hence, the smaller the $\langle L \rangle_d$, the smaller its enhancement.

Interestingly, the pressure dependence of magnetization in both crystal stuctures dramatically changes at ≈80 GPa. Analysis of the band structure revealed that at such compressions the magnetic splitting is not sufficiently strong to keep the entire majority-band occupied. As a result, spin-up states start to cross the Fermi level and this makes the magnetic moment more sensitive to pressure. Measured XMCD signal also changes its behavior at ≈75 GPa, but at these compressions the hysteresis of the hcp-fcc transition already emerges, as seen in the XAS data [161]. It is reasonable to assume that all these band structure features are interconnected. Most likely, the above-mentioned change of the Fermi surface is responsible for destabilization of the hcp structure.

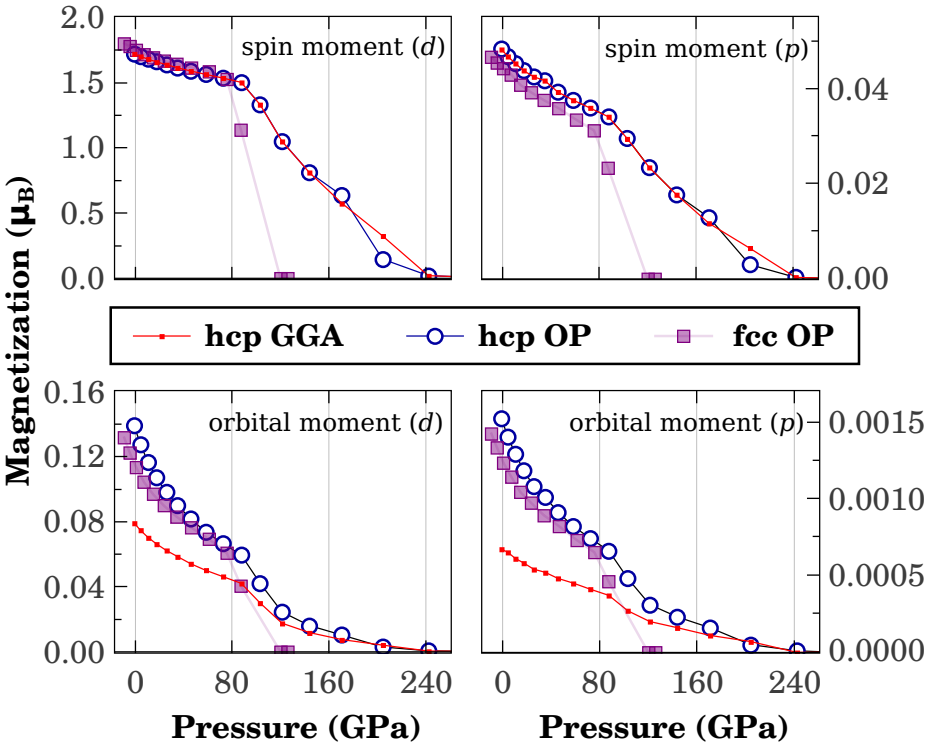


FIGURE 2.5: Calculated spin and orbital components of $l-$projected magnetic moments in hcp and fcc Co as a function of applied pressure. Note that absolute values are plotted; $\langle S \rangle_p$ is antiparallel to $\langle S \rangle_d$.

Since absolute values of magnetizations are not accessible with the K-edge XMCD, it is rather difficult to judge whether the OP term really improves the result. The overall physical picture is unchanged: we again witness that quenching of orbital moment upon compression is much faster than that of spin one.

2.4.1 Simple view on the evolution of L and S under pressure

On the first sight, it looks counter-intuitive, that orbital and spin moments behave differently under pressure. We will show that a simple quantum-mechanical picture is able to explain it.

Let us consider the d-electron shell in a cubic environment and add SOC as a perturbation. If exchange splitting is bigger than the crystal field, one can neglect the possibilities of the spin-flip transitions and re-write the SOC operator in a simpler form (as done in

e.g. [21]):

$$\hat{H}_{SO} \approx \lambda L_z S_z, \tag{2.4}$$

where λ is SOC coupling constant. Terms associated with $S_\pm$ are omitted. This way $\hat{H}_{SO}$ has only few non-zero matrix elements, namely:

$$\langle d_{xy}|\hat{H}_{SO}|d_{x^2-y^2}\rangle = \big(\langle d_{x^2-y^2}|\hat{H}_{SO}|d_{xy}\rangle\big)^* = 2i\lambda S_z. \tag{2.5}$$

First-order corrected d_{xy} orbital will take admixture from $d_{x^2-y^2}$ state:

$$|d'_{xy}\rangle = |d_{xy}\rangle - \frac{2i\lambda S_z}{E_{xy} - E_{x^2-y^2}}|d_{x^2-y^2}\rangle, \tag{2.6}$$

where E_i is the energy of unperturbed i-th level. The denominator, therefore, equals to the unique crystal field parameter Δ_{cf}. The contribution from this electron state to the total orbital moment can be estimated as (see e.g. Ref. [155][p. 303]):

$$\langle d'_{xy}|L_z|d'_{xy}\rangle \sim \frac{\lambda}{\Delta_{cf}}\langle d_{xy}|S_z|d_{xy}\rangle. \tag{2.7}$$

Effect of pressure leads to the increase in Δ_{cf} and presumably modifies λ. If we assume that λ is not much sensitive to the pressure, one immediately sees that the orbital moment attenuates faster than the spin one. Similar tendency was reported for $5f$ systems [19], but perturbative treatment of SOC would be doubtful for such "heavy" orbitals.

Generally, there is no direct relation between spin and orbital moments. The latter results from an interplay between crystal structure, band filling and spin-orbit coupling. Present situation takes place in $3d$ metals and our experimental and theoretical studies of the XMCD show that the analysis of S and L has to be done separately.

2.5 Competing phases in FeCo alloy

Iron and cobalt are neighboring elements in the periodic table and, therefore, have similar electronic properties. Bulk phases of both metals exhibit spontaneous ferromagnetism with a rather well-developed magnetic moments. The difference of single electron in a

valence band seems to be negligible for magnetic properties. However, due to this fact pure iron is on the edge between "strong" and "weak" ferromagnets, while elemental Co has majority band fully occupied (see e.g. p.82 in ref. [120]).

FeCo alloy in its CsCl-structure is a nice textbook example of so-called covalent magnetism [150]. Due to similar ionic electronegativities, charge transfer processes between iron and cobalt atoms are strongly suppressed. Their states efficiently hybridize and form bonds of mainly covalent character. Bound together, Fe and Co able to further increase Fe spin magnetization: in FeCo alloy its value per unit cell reaches almost 3 μ_B. As a result, this system is known to have one of the largest values of the Curie temperature (>1500 K). It is interesting to investigate how such well-pronounced magnetic properties will be affected by uniform compression.

2.5.1 X-ray experiments

Measurements of x-ray diffraction, along with the XAS and XMCD at Fe and Co K-edges were carried out on two types of $Fe_{0.5}Co_{0.5}$ samples, depending on their preparation conditions. One of the them was annealed up to 350^{o}C for one day, while second one was use as it is (called "as prepared" onwards).

Results of the XAS and XMCD experiments made on "as prepared" sample are shown on Fig. 2.6.

One can see that overall fine structure at both Fe and Co edges have very similar shape. The pressure evolution of spectral features share the same degree of similarity. As a sample gets compressed, the peak "c" located at ≈50 eV becomes more pronounced, whereas features "d" and "d′" merge into a single oscillation. The same changes in Fe K-edge were observed in the case of bcc-to-hcp transformation of iron [115]. Above 32 GPa the structure is stable and further compression does not change it. Formation of this low-volume crystal structure was confirmed by diffraction measurements. It starts at the pressure of 31 GPa and reaches saturation at 35 GPa.

It is worth noting that the degree of chemical order is rather difficult to extract from the present experiments. As it was mentioned, x-rays are too insensitive to such similar elements like Fe and Co.

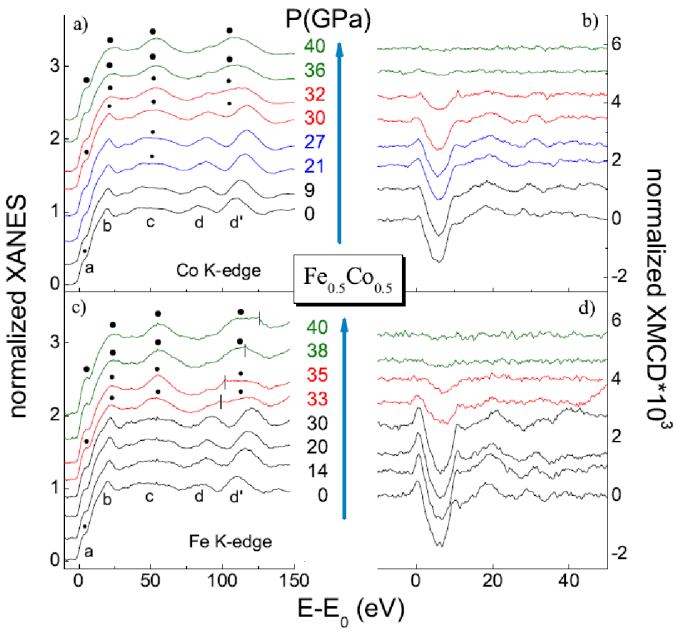


FIGURE 2.6: Normalized XAS and XMCD spectra of $Fe_{0.5}Co_{0.5}$ at Co K-edges (panels "a" and "b", respectively.); and that at Fe K-edge (panels "c" and "d"). Pressure axes are indicated by blue arrows.

The results of XAS and XRD experiments for annealed sample are not shown here, since majority of properties are the same as in the "as prepared" one. However, slight differences in crystal structures were found. We report that annealed samples are characterized by larger lattice constant in bcc phase and anomalous c/a ratio in hcp one. The changes are minor, but considerably affect the magnetic properties.

Concerning XMCD spectra, both samples are characterized by rather stable XMCD signals at both Fe and Co absorption edges. It is very pronounced down to transition pressure, where it suddenly drops. Disappearance of the signal takes place along with the structural transition, indicated by other techniques. Fig. 2.7 shows integral of the main peak of the Co K-edge XMCD spectra for annealed and "as prepared" samples.

According to the data, the way how sample is prepared indeed affects magnetic properties and is able to push the magnetic transition towards lower volumes range. Indeed, annealed sample showed disappearance of magnetic signal close to 40 GPa.

2.5.2 Phase diagram from first principles

Clearly, the observed drop-off of XMCD under pressure is an indication of restoring of the macroscopic time-reversal symmetry, i.e. disappearance of the net magnetic moment

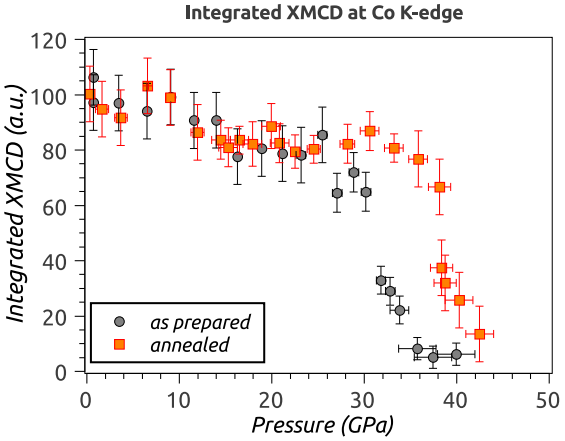


FIGURE 2.7: Integrated main peak intensity of Co K-edge XMCD signal as a function of applied pressure for annealed and "as prepared" samples.

(which, however, does not exclude antiferromagnetism).

Hence, the question we are going to pose is whether a given crystalline phase has a preference to be magnetic or not under certain external conditions. Spin-polarized DFT calculations without SOC are already able to answer this question. For this purpose we carried out first-principles simulations using `VASP` code [99], which is a realization of PW+PSP method. An XC potential of PBE [135] type was used, since it is known to yield fair estimates of equilibrium volume for this system. The enthalpy $H = E_{tot} + PV$, where E_{tot} is total energy, was used as a criterion to establish the most convenient structure as a function of the pressure. Magnetization around Co and Fe atoms was measured within a Wigner-Seitz radii of 1.3 Å and 1.16 Å, respectively.

Due to lack of unambiguous information about chemical order of studied FeCo samples, we decided to investigate how different possible structures would react on applied pressure from *ab initio* viewpoint. Calculations were carried out for the CsCl-type crystal structure of FeCo alloy (Fig. 2.8(a)), which is the most preferable one from thermodynamical viewpoint at ambient conditions. Its hcp counterpart shown in Fig. 2.8(c) was constructed, following the same transition path, as proposed for elemental iron [22, 42]. In this scenario, the bcc-hcp transformation is of martensitic type, where two neighboring (110) planes are shifted and sheared, hence forming a proper hcp stacking [8]. In order to study the effect of chemical environment, we have also considered a Zintl-type

[8] In principle, transformations involving diffusion of some atoms can not be omitted. However, it is likely to be separated from initial state by rather high energy barriers. Present issue requires an additional investigation.

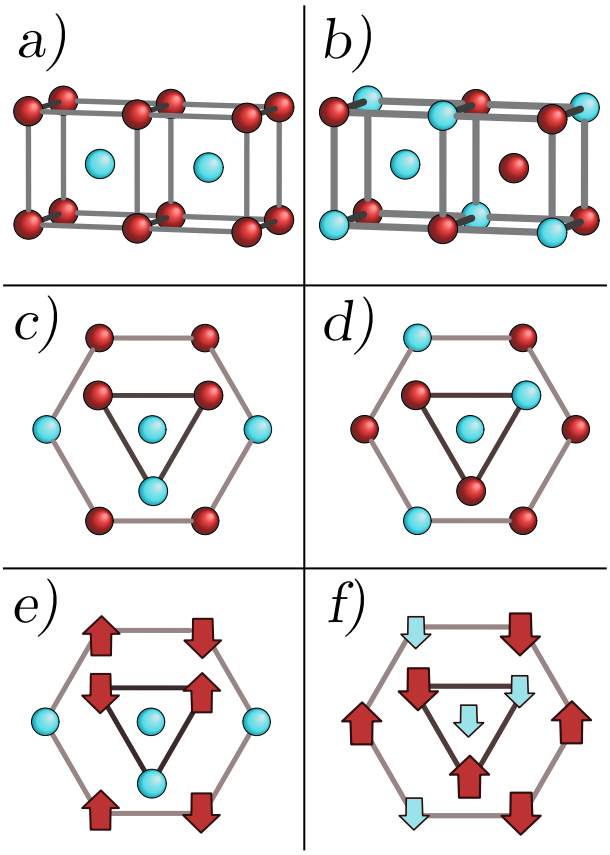


FIGURE 2.8: (colors on line) Considered crystal structures of equiatomic FeCo alloy. Panels “a” and “b”: bcc CsCl and Zintl phases. Their hcp counterparts are depicted in panels “c” and “d”, respectively. Vinous and cyan (dark and light) spheres represent two atomic sorts (Fe and Co). Shaded areas indicate the (110) planes in bcc structures, which become (0001) and (0002) ones in the hcp states. Mentioned planes are represented by a hexagon and a triangle in the hcp phase; Panels ”e“ and ”f“: suggested spin configurations in high-pressure hcp phases (see text).

structure, characterized by each atom being coordinated with 4 atoms of the same element and 4 of the other type This way the amount of homoatomic bonds is maximized. Corresponding bcc and hcp crystal structures are shown in Fig. 2.9 (panels ”b“ and ”d“).

Then, for a given crystalline phase, several magnetic configurations were studied, for instance: high(low)-spin [H(L)S] FM, AFM and non-magnetic (NM) states. Note, that the list of considered states is not exhaustive; however, it order to find the magnetic ground state one has to extract and thoroughly analyze exchange integrals (see e.g. Ref. [110]), which is beyond the scope of the present study. Starting from a particular spin structure, the Bravais vectors of the lattice were optimized to provide a certain value of isotropic stress. We report that the assumed magnetic state strongly influences

corresponding crystal structures. In particular, pronounced deviations of c/a ratio in hcp phase are reported.

The comparison between calculated enthalpies for different phases, shown in Fig. 2.9 (top panel), confirms that the ferromagnetic CsCl-type bcc structure is energetically the most preferable at ambient pressure. Interestingly, that neglecting spin polarization,

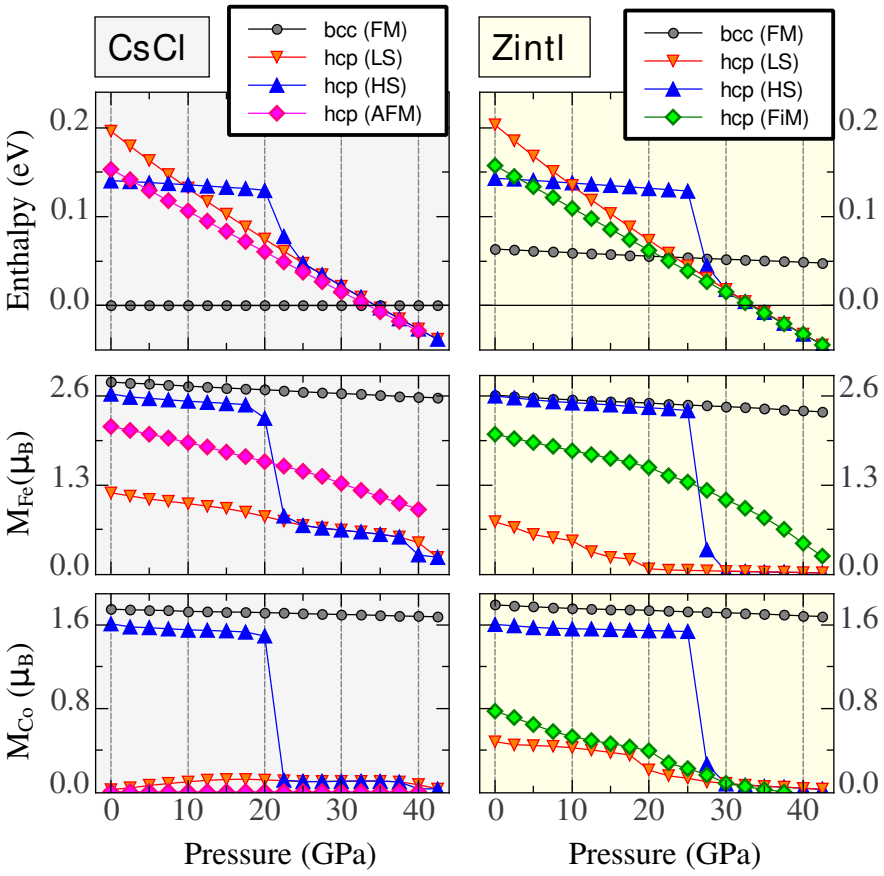


FIGURE 2.9: Calculated relative enthalpies per atom and saturated magnetic moments in various phases of equiatomic FeCo alloy. Left panels: CsCl structures, right: Zintl. Enthalpy of CsCl bcc phase at each pressure is taken as reference.

hcp structure becomes a preferable one at equilibrium. Hence, it is magnetism that plays a key role in the stabilization of the bcc phase, as was already pointed out in several prior studies [1, 34, 100]. However, as the applied pressure is raised, the system's tendency for compact atomic arrangement starts to dominate. This leads to the hcp phases having lower enthalpies at ≈33 GPa, in agreement with experimental outcomes. At this point, several magnetic configurations are almost degenerate in energy, due to smallness of corresponding magnetic moments. Among the studied spin configurations in the hcp structure, the AFM one, shown in Fig. 2.8(e), has a lower enthalpy than any

other configurations, starting already from 2.5 GPa of applied pressure. Notably, in this state, Co ions, surrounded by iron moments pointing "up" and "down", turn out non-magnetic. The present result agrees with the outcomes of prior studies on disordered FeCo alloys, where strong dependence of Co magnetization on its magnetic environment was pointed out [85]. Therefore, Co exhibits a Stoner-like behavior of magnetism in this case.

Similarly, the occurrence of antiferromagnetism in the high-pressure hcp phase of pure iron was suggested by several research groups [55, 154]. The AFM exchange interactions (J) between nearest neighbor Fe atoms are suspected to be the origin of stabilization of this state [93]. However, triangular lattice is frustrated for such sign of J, thus might give rise a non-collinear spin arrangements [106].

In the case of FeCo, total energy analysis of various magnetic states suggests the same sign of Fe-Fe interactions. However, opposite to the case of pure iron, the presence of another atomic sort permits to reduce the symmetry and remove the frustration. Indeed in CsCl hcp phase, Co atoms become NM, therefore do not participate in magnetic couplings, and all Fe-Fe interactions can be satisfied within the geometry, shown in Fig. 2.8(e).

Concerning Zintl phase, the martensitic bcc-hcp transformation is predicted to happen at lower pressure, as compared with CsCl structure, i.e. around 22 GPa (Fig. 2.9). According to our results, its hcp phase also shows a tendency to antiferromagnetism among nearest neighboring Fe atoms. However, environment of Co atoms is less symmetrical in this case and we found that it can acquire a non-zero magnetization. These moments show the preference for FM ordering and thus we found that a kind of ferrimagnetic (FiM) state, shown in Fig. 2.8(f) to have lower enthalpy than other FM and AFM states. Here, net Fe magnetization is compensated, whereas the one originated from Co is finite. It equals $\approx 0.77 \mu_B$ per atom at ambient pressure and gradually decreases upon volume compression. As a consequence of the small (or absent) Co magnetization, Fe is pushed back to the "weak ferromagnet" limit and its magnetic moment becomes more sensitive to the application of pressure as compared with FM bcc states (Fig. 2.9).

In both suggested high-pressure magnetic configurations iron magnetic moments order antiferromagnetically. Since K-XMCD is not sensitive to such spin arrangements, the emergence of the present state is a possible explanation for a drop of magnetic signal in

this experiment. We suggest that this scenario may be confirmed by linear dichroism measurements.

The "as prepared" sample, which is presumably less ordered, undergoes a transformation at around 35 GPa, whereas calculations for disordered Zintl structure suggest transition to take place at much lower pressures. This is a possible indication of existence of a chemical short-range order, invisible to XRD because of the short coherence length of ordered domains and the closely similar scattering factors of Fe and Co, which weakens the superlattice reflections. Moreover, considered Zintl phase is not supposed (and not meant) to be a good representation of actual disorder. These findings again emphasize that the chemical order (and the preparation route) play a crucial role in tuning the high pressure magnetic and structural response.

2.6 Conclusions

The studies of Ni and Co with the K-edge XMCD technique showed that spin and orbital moments in $3d$ metals respond differently to applied pressure. This is clearly seen in measured spectra and quantitatively well described with the help of the DFT simulations. Present result does not violate intrinsic electron properties, such as Landé factor, but is a consequence of perturbative character of the SOC in these systems.

An example of FeCo alloy showed that experimental tools are not always able to provide all necessary information about studied system. But when computational methods are known to give reliable results for a class of compounds, they can be used as an additional source of information about certain system. In the present case the DFT-based calculations helped to understand structural preference of specifically prepared samples of FeCo alloy.

In general, such a co-operative experimental and theoretical study of transition metals under pressure is very beneficial. Being able to be combined with DACs, the X-ray diffraction yields an unequivocal information about structural changes, while the K-edge XMCD detects the presence of magnetization at the atoms of a particular element.

The DFT can help to establish the connection between these structural and magnetic properties. Of course, its ability to play role of a tool of prediction is not unlimited.

Approximations which we make for exchange and correlation effects within this method can sometimes result in a poor quality of electronic structure modeling.

However, above-mentioned experimental techniques provide with enough information, which can be used as a reference points for theory and, first, should be tried to be reproduced using computational tools. Once some of these reference points are passed, one can try to proceed with predictions of particular properties.

In general, use of all these techniques together is the best way for understanding the influence of volume compression on the properties of $3d$ systems.

Chapter 3

High-pressure phase of $FePd_3$ ordered alloy from first principles

3.1 Introduction

Elemental iron, being the base of steels, is of big importance for modern technology [133]. It has a very rich phase diagram, but the face-centered cubic form is exceptionally interesting. In pure γ-Fe first-principles calculations predict the stabilization of a spin spiral state [147]. For some fcc-based alloys, like Fe-Ni and Fe-Pt ones, it was shown that the sign of effective magnetic couplings (FM or AFM) is volume-dependent [94, 128, 140]. It turned out that interactions are more ferromagnetic at higher volumes and opposite at lower ones. ones. AFM couplings on frustrated and chemically disordered lattices give rise to the stabilization of non-collinear GSs at certain volume range, as was predicted by van Schilfgaarde and co-workers [165]. According to theoretical calculations, this transition can be achieved by application of external pressure [2, 141].

Several experiments at high pressures were carried out on disordered Invar Fe-Ni alloys [32, 35, 116, 117]. These measurements confirmed the stabilization of a spin-glass state under pressure in Fe-Ni and Fe-Pt alloys [116, 117] and compression-induced change of the magnetic state (magnetovolume instability). These observations are in agreement with predictions of a sharp deviation of exchange interactions with pressure reported for these systems [92, 128, 140].

Thus the magnetism of iron on fcc lattice gives rise to all these peculiar properties and is a very important subject of the research.

$FePd_3$ is one of the systems where this situation is realized. This alloy has recently attracted a strong interest due to its Invar behavior. One experimental group has recently observed that under an applied pressure of 7 GPa the system shows an anomalously small thermal expansion [172]. Same effect was reported for $Fe_{50}Ni_{50}$ disordered alloy [35]. Moreover, as it will be shown below, non-collinear spin states are stabilized in $FePd_3$ at low volumes, similarly to the $Fe_{50}Ni_{50}$ case.

Winterrose *et al.* [172] carried out a joint experimental and theoretical study of $FePd_3$ under pressure. According to results of the XRD measurements, the system sustains a significant volume collapse under pressure of 12 GPa. However, its $L1_2$ structure is preserved. Moreover, under the same applied pressure they observed a disappearance of quantum beats in a Nuclear Forward Scattering (NFS) experiment, which implies the loss of long-range magnetic order in the system.

By means of DFT-based calculations the authors modeled elastic properties of few possible magnetic configurations of $FePd_3$ and compared it with measured data. They came to the conclusion that the system undergoes a HS-LS transition under pressure. This supposition is supported by the fact that the obtained magnetic moments in the LS state are very tiny (of the order of 10^{-2} μ_B) and therefore it can explain the disappearance of signal in the NFS experiment. On the other hand, the LS state was never found to possess lower total energy than the FM one in the studied pressure range. Nevertheless, the authors emphasized that T_c can be seriously affected by volume compression, and, therefore, there is a possibility of paramagnetic phase formation.

$FePd_3$ is composed of rather localized (Fe) and itinerant (Pd) magnetic moments. One of the first attempts to account for coexisting magnetism of different types was carried out by Mohn and Schwarz [121]. They proposed a model where local spins produced an effective Weiss field acting on itinerant magnetic sublattice. The parametrization of the model was based on the results of *ab initio* calculations. The developed model was applied for Fe-poor Fe_xPd_{1-x} ($x < 0.1$) alloys and estimated Curie temperatures were found to be in good agreement with experiment.

Influence of induced moments on overall magnetic properties of Fe-based alloys was intensively studied by Mryasov and co-workers [122, 123]. For instance, it was pointed out that polarized Pt atoms are responsible for anomalous temperature behavior of magnetocrystalline anisotropy in FePt; magnetization of intrinsically neutral Rh atoms modifies phase stability of FeRh alloy.

Polesya and co-workers [137] proposed a model where induced magnetization was defined via vector sum of adjacent magnetic moments. The approach was applied to series of Fe-Pd and Co-Pt solutions yielding T_c values in a fair agreement with experimental data.

First-principles study of magnetic properties of $FePd_3$ under pressure was recently performed by another research group [36]. In order to interpret previous experimental results [172], the authors probed different disordered states and arrived at a conclusion that none of them is the true GS of the compressed system. However, a strong competition between commensurate (FM/AFM) and incommensurate magnetic phases was observed. This is an indication that the system may transform to some non-collinear state under pressure, but its topology is unknown.

3.2 Modeling of incommensurate magnetic structures

Mainly motivated by the results of Winterrose *et al.* [172], we decided to investigate different non-collinear magnetic orderings in $FePd_3$. Of course, it is impossible to probe all configurations; therefore, we have concentrated only on the most plausible ones. Moreover, a "random walk"-like search of magnetic moments orientations is a difficult task, since the differences in energies associated to spin deviations are quite small (∼meV), so the total energy profile is shallow and in addition has many local minima. For this reason the directions of iron magnetic moments were prescribed and kept frozen during the simulations. Magnitudes and orientation of Pd moments were obtained self-consistently with no constraints on these parameters. Present strategy is used throughout the text, unless another one is specified.

Electronic structure was modeled using `PY-LMTO` code. Correlation effects were treated within LSDA with the parametrization of Vosko, Wilk and Nusair [168]. The crystalline structure of the system under consideration, shown in Fig. 3.1, was preserved during all simulations. The only parameter which was varied is a lattice constant. Its equilibrium

experimental value (a_0) equals 3.849Å [75, 172] and we shall refer to its corresponding volume V_0 throughout this Chapter.

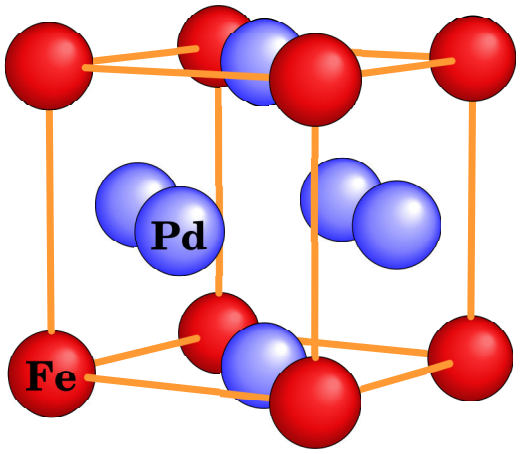


FIGURE 3.1: Schematic representation of ordered $FePd_3$. The alloy has an fcc-based $L1_2$ (Cu_3Au) structure, where Fe atoms are located at the corners of the cube and Pd atoms are at the centers of the faces.

3.2.1 Spin spirals

We started our analysis from calculations for various spin spiral (SS) states. These simulations were carried out on the basis of the generalized Bloch theorem [146], where lattice translations are accompanied by certain rotations of the spin moment. It is worth emphasizing that that these calculations are still scalar relativistic, so spin degrees of freedom are decoupled from the lattice ones. This implies conservation of a global spin rotational invariance and therefore the direction of quantization axis can be chosen arbitrarily; we shall align it along the z axis. Hence, SS states are defined by four parameters: the propagation vector [$\vec{Q} = (q_x, q_y, q_z)$] and the angle Θ between magnetization and the z axis. Once these parameters are chosen, the magnetization of the iron atom in neighboring cells is simply rotated by an angle $\phi_i = \vec{Q} \cdot \vec{R}$, where $\vec{R}$ denotes a translational vector. In our calculations the initial phases of Pd moments, located at positions $\vec{t}_i$, were set to $\phi_i^0 = \vec{q} \cdot \vec{t}_i$, but were free to choose preferred orientation during the self-consistent loop.

First, a manifold of the states characterized by $\Theta = 90^o$ was studied. The energies of these states as a function of a wave vector are shown in Fig. 3.2. According to the obtained results, the FM state (corresponds to Γ point) has the lowest energy among

all considered configurations. In addition there are two local minima at X and M high

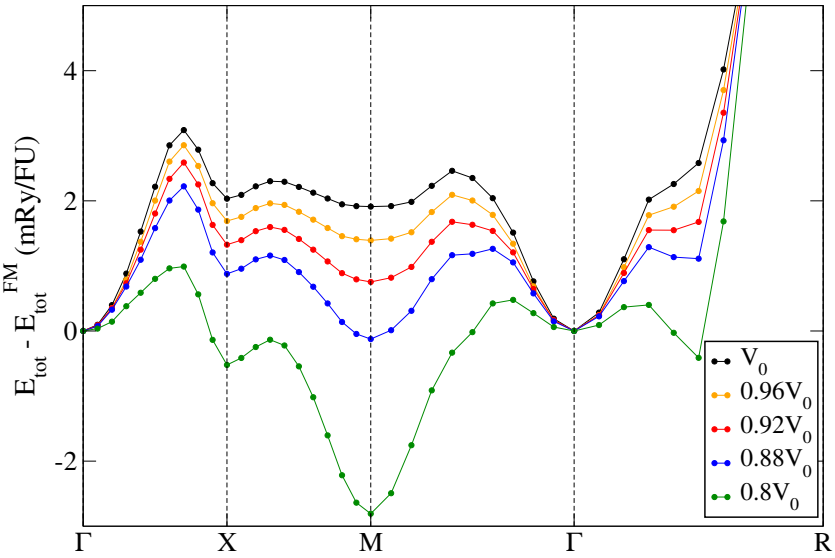


FIGURE 3.2: Total energies of spin spiral states ($\Theta = 90^o$) relative to the energy of the FM state at a given volume in $FePd_3$. Directions $R - X$ and $R - M$ are not shown, since wave-vector dependence of E_{tot} was found to be monotonic along these paths. The energies are given per chemical formula unit (FU).

symmetry points. These points correspond to antiferromagnetic states with ordering vectors [100] and [110], respectively. Another minimum is lying along $\Gamma - R$ direction and corresponds to wave vector $\mathbf{q}$=$(\frac{\pi}{2a}, \frac{\pi}{2a}, \frac{\pi}{2a})$.

Present magnetic structures have been already studied by another research group [36] using FP-LAPW method. Our results obtained with LMTO are in fair agreement with those calculations, which are supposed to be more accurate ones.

As the cell is compressed, the stability of the FM state is reduced and at the volume about $0.88V_0$ we observe the magnetic transition at the point M corresponding to the AFM[110] phase, as was previously reported by Winterrose and co-workers [172] (see Fig. 3.2). Augmentation of pressure leads to further destabilization of the ferromagnetic configuration.

It should be noted that iron has a quite rigid magnetic moment in the entire considered volume range: For majority of configurations, as volume is decreased by 20%, its magnetization M_{Fe} lowers by not more than 11%.

It is also worth noting that, for a given volume the magnitude of the iron magnetic moment in different SS states are very similar. The highest difference was observed

between the FM and AFM[110] states and was estimated to be ≈0.1 μ_B per atom. Whereas the value of M_{Pd} strongly depends on orientation of adjacent Fe spins as was already pointed out by another group [137]. For example, at V_0 volume in FM state all Pd ions possess the magnetic moment of ≈0.35 μ_B per atom. In the layered AFM[100] state Pd atoms which belong to the same layer as Fe atoms have a magnetization of 0.14 μ_B per atom, pointing parallel to the iron moment. The remaining palladium atoms are non-magnetic. In the AFM[110] all Pd moments collapse to zero, because each of them is surrounded by an equal number of Fe moments pointing parallel and antiparallel to the field.

Next, various helical structures were simulated. Here we have chosen two $\vec{Q}$-vectors, corresponding to the lowest states, observed so far, namely AFM[100] and AFM[110]. After fixing these three parameters of the SS, the Θ angle was varied.

Energies of helical SS's are shown in Fig. 3.3. First, a destabilization of the FM state

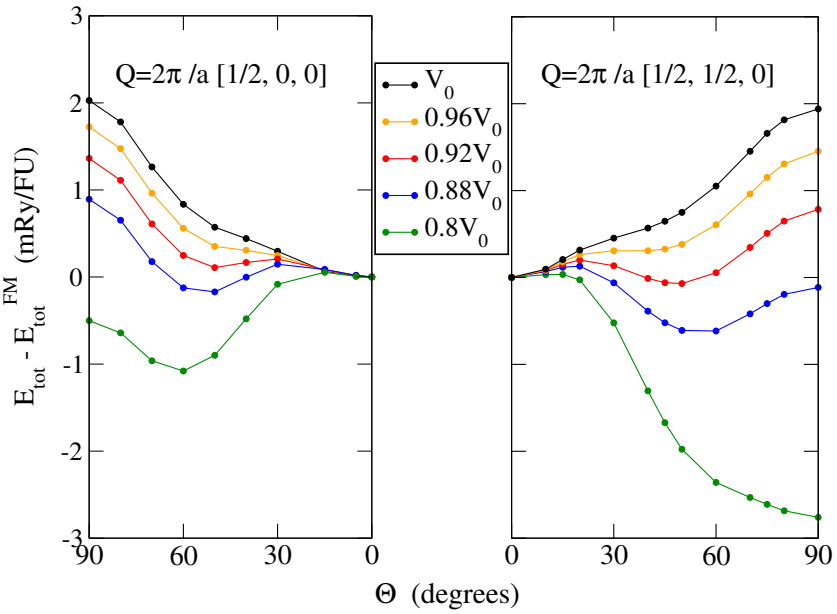


FIGURE 3.3: Energies of helical spin configurations as a function of the angle between magnetization and the z axis in $FePd_3$. Values are relative to the energy of the FM state at a given volume.

upon compression is again well-pronounced. However, for both studied directions ($\vec{Q}$), we observed a wide range of volumes where helical states were in favor. As the cell is compressed to $0.92V_0$ the FM phase becomes almost degenerate with two more states, which in the coordinate system ($\vec{Q}, \Theta$) correspond to the points (X,50^o) and (M,50^o).

In overall, the helical structures along M direction are favored. At $0.8V_0$ the AFM[110] phase possesses the lowest energy among all considered states.

3.2.2 Canted spin states

For deeper exploration of magnetic states manifold, we have constructed a 2×2×1 supercell of $FePd_3$ which contains four Fe atoms. The angle θ for iron spins was introduced in a way shown in the inset of Figure 3.4. It is easy to see that $\theta = 0$ corresponds to the AFM[110] phase and $\theta = 180^o$ – to AFM[100]. Therefore, by tuning θ one can go continuously from one state to another. At each volume self-consistent calculations were carried out for the angle θ constrained to a given value. According to the results, shown

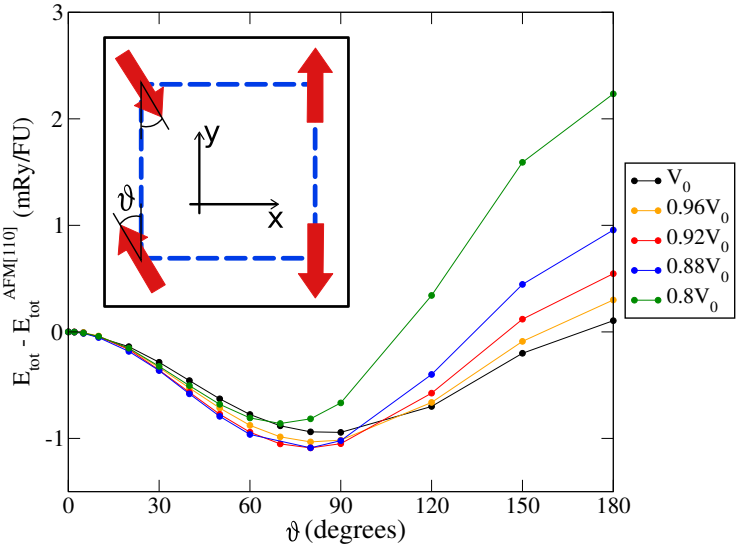


FIGURE 3.4: Results of the total energy DFT calculations of canted states in ordered $FePd_3$. The inset shows the magnetic structure under consideration. Red arrows indicate iron magnetic moments. Pd magnetization is not shown.

in Fig. 3.4, resulting function $E_{tot}(\theta)$ in addition to the points $\theta = \{0, 180^o\}$ has one more minimum at certain angle (θ_0). Such angular dependence can not be reproduced within classical Heisenberg model, which should give a "$\cos(\theta)$" curvature[1]. Present issue will be later addressed in more detail.

Hence, at this stage we can confirm that $FePd_3$ indeed has a tendency to spin non-collinearity. Application of pressure causes destabilization of the FM state, several

[1]The present shape of the total energy profile was found even without inclusion of spin-orbit coupling. Therefore, relativistic effects, such as magnetic anisotropy, are not responsible for such behavior.

configuration with lower total energies were found, but true low-volume GS is still unknown.

3.3 Heisenberg exchange parameters

In order to have a deeper insight into magnetic properties of the system, we have extracted Heisenberg exchange integrals from several spin configurations. Then, calculated J_{ij}'s were used to model low-energy magnetic excitation spectra, following the approach discussed in Chapter 1. Indeed, such analysis is expected to be valid for Fe spin subsystem, since it is characterized by relatively large and rigid magnetization. However, application of the magnetic force theorem to systems with induced local moments is doubtful (see e.g. [148]) Therefore, our first idea was to possibly suppress Pd degrees of freedom.

For this purpose we have considered a disordered local moment (DLM) [72] configuration, which is supposed to model high-temperature paramagnetic (PM) phase. In present context it means that we have constructed a pseudo-ternary alloy ($Fe^{\uparrow}$,$Fe^{\downarrow}$)Pd_3, where spins pointing parallel and antiparallel ($Fe^{\uparrow}$ and $Fe^{\downarrow}$, respectively) to the field, are randomly distributed. The effect of disorder is taken into account within the Coherent Potential Approximation (CPA), as implemented in TB-LMTO-CPA [163]. The DLM approach is used to describe properties of the system consisting of randomly distributed magnetic impurities embedded in a non-magnetic medium. Its major advantage is that induced magnetization on intrinsically non-magnetic ions, collapses to zero in this phase.

According to the obtained results, magnetization of Fe atoms in the DLM state is almost unchanged with respect to FM one. This is also true for a compressed unit cell and therefore there is no tendency to suppression of the magnetic moment as suggested by the HS-LS scenario [172]. Present conclusions have already been reported [36].

As expected, in the DLM state Pd magnetic moments have collapsed to zero due to random orientations of Fe spins. We made one step forward and extracted effective exchange integrals as a function of inter-atomic distance for a few fractions of equilibrium volume. Results are shown in Fig. 3.5. The results suggest that the first and second nearest-neighbor (NN) interactions are dominant. While the first NN interactions (6

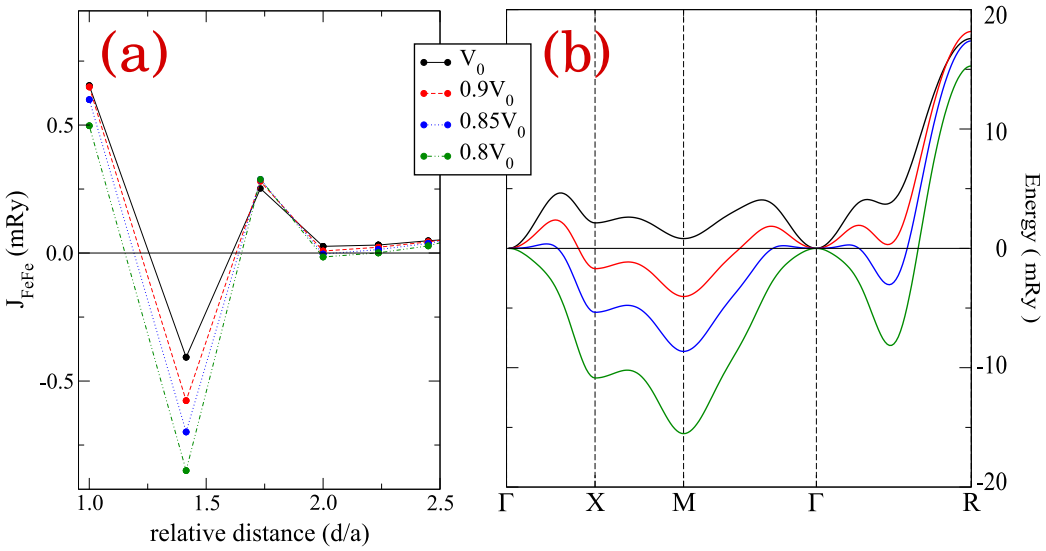


FIGURE 3.5: (a)The Fe-Fe exchange interactions in $FePd_3$ as functions of the relative inter-atomic distance d/a, where a is the lattice parameter. (b) corresponding frozen magnon-dispersion relations. 83 neighbor shells were used for the Fourier transform of J. The results obtained from the DLM reference state calculated for different cell compressions.

neighbors) are FM, the second NN (12 neighbors) couplings are AFM. Third NN exchange parameters, which are FM, are also important. Such oscillatory behavior is due to the RKKY [142] exchange mechanism and is similar to that reported for pure bcc Fe [130].

Remarkably, we observe a strong increase of second NN AFM interactions with pressure while all other couplings depend on volume much more weakly. Moreover, the corresponding neighborhood forms the fcc lattice, which is frustrated for this sign of interaction. Here the frustration, being a natural source of noncollinearity in spin systems, is found to effectively increase its contribution at lower volumes.

Magnon dispersions, calculated using Eq. (1.29), are shown in the panel "b" of Fig. 3.5. It is seen that instabilities at X and M points become more pronounced as the pressure is raised. Interestingly, the overall shape of this function is very similar to the energies of transverse SS's (Fig. 3.2). A one-to-one correspondence between two plots should not be expected, since they describe propagation of different spin waves: the ones characterized by $\Theta \to 0$ and $\Theta = 90^0$, respectively. However, the observed agreement implies that extracted J_{ij} parameters are meaningful.

Next, the same analysis of J's was done for the AFM[110] state. Two iron sublattices which appear in this state are denoted as Fe_A and Fe_B. Present structure is defined on a tetragonal $\sqrt{2} \times \sqrt{2} \times 1$ supercell. Extracted exchange integrals for compressed cell ($0.8V_0$) are shown in Fig. 3.6. Calculated magnon energies (Fig. 3.7) indicate a few

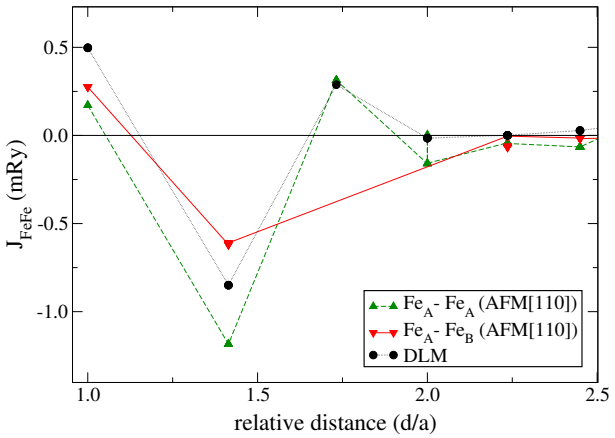


FIGURE 3.6: Iron-iron exchange parameters obtained from DLM and AFM[110] states for $0.8V_0$. Two magnetic sublattices are denoted as Fe_A and Fe_B.

instabilities and the primary one corresponds to the $Z = \frac{2\pi}{a}(0, 0, \sqrt{2})$ point. In spite of

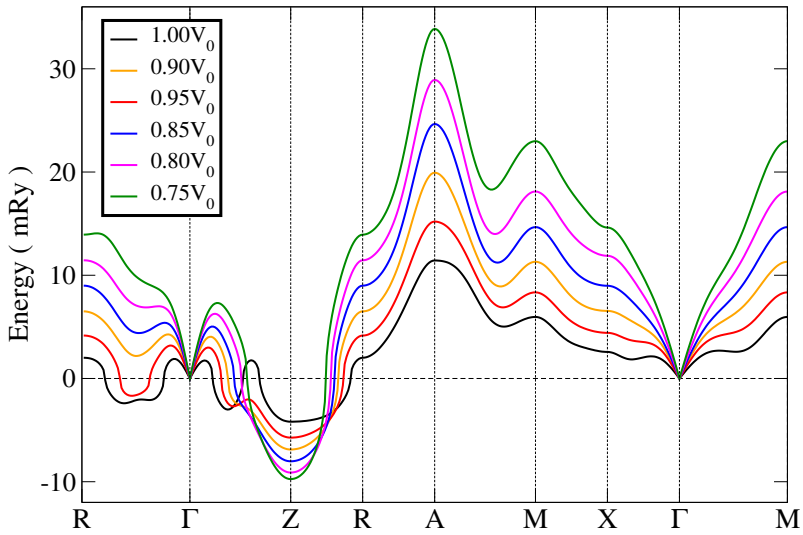


FIGURE 3.7: Volume dependence of frozen magnon energies for $FePd_3$ in the AFM[110] state.

the fact that under applied pressure this state has lower energy than the FM one, its magnetic instability further develops and corresponding minimum is enhanced.

Hence, in a low-volume region all considered phases have demonstrated local magnetic instabilities, indicating that any small perturbation would destroy the state. In other

words all these magnetic configurations are not even local minima on a phase diagram of the system under consideration.

3.4 Extended Heisenberg model

An analysis of exchange integrals obtained from AFM[110] reference state (Fig. 3.6), suggests that the couplings of the "AA"-type are very different from "AB" ones. This effect is mostly pronounced for second NNs, whose corresponding Fe-Fe bonds pass directly through palladium atoms. Therefore it is reasonable to assume that interactions are mediated due to the presence of these paramagnetic ions.

Indeed, palladium is a rather peculiar element: its bulk phase is characterized by a high value of DOS(E_f), so the Stoner criterion is nearly satisfied. Therefore Pd can be easily polarized by putting in a contact with magnetic ions.

The underlying physics of exchange renormalization can be understood by analyzing the expression Eq. (1.26). Since the magnitude of Fe magnetic moment is almost independent of a chosen magnetic order, $|\Delta_{Fe}|$ is unchanged. Therefore what gives rise to the observed difference in exchange couplings is the intersite Green's function. For instance, in the FM state an electron, going from one iron site to another, propagates through a strongly polarized medium, while in the AFM state this polarization is missing. Since Pd magnetization is large ($\sim$0.3 μ_B per atom), being a first-order term in Δ_{Fe}, its disappearance gives a significant impact on G_{ij} and eventually on exchange integrals.

Similar behavior was already reported for FeRh compound [123]. Of course, this situation does not take place in every system and can be considered as a specific characteristic of 4*d* elements. In order to emphasize this fact, we performed additional calculations for a hypothetical system, where palladium was substituted with copper atoms within same geometry of the unit cell. Opposite to the $FePd_3$, Cu atoms are non-magnetic independently of the magnetic order. Calculated exchange integrals are represented in Fig. 3.8. In this case we found that J_2 parameters extracted from both configurations almost coincide with each other. Thus we do not observe any pronounced deviations from the Heisenberg magnet behavior. Change in J_1 can be expected, since it is mostly originated from the direct overlap of the orbitals.

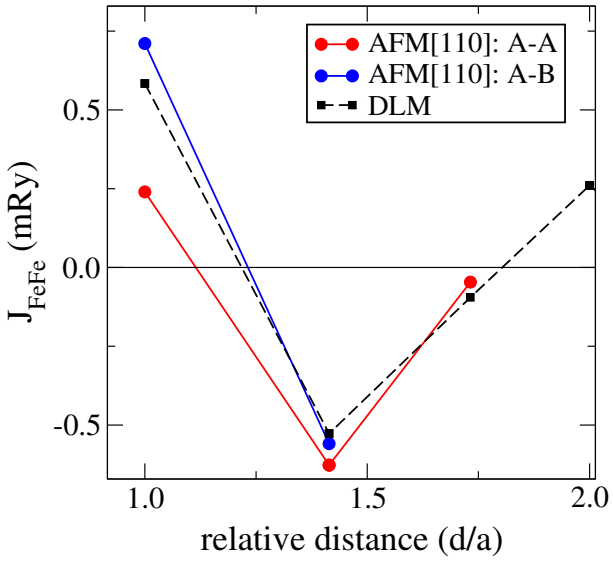


FIGURE 3.8: The Fe-Fe exchange interactions in hypothetical $FeCu_3$ alloy as functions of inter-atomic distance d/a.

Hence, in the case of $FePd_3$ a classical Heisenberg model with pairwise interactions and bilinear exchange only, cannot properly map the dependence of the total energy on the magnetic states and must be extended to include higher-order exchange terms, i.e.:

$$\hat{H} = \hat{H}_{exch} - \sum_{i \neq j} J'_{ij} (\mathbf{e}_i \cdot \mathbf{e}_j)^2, \tag{3.1}$$

where $\hat{H}_{exch}$ is given by Eq. (1.23); J' is a biquadratic exchange parameter.

Parameterization of the model was done using the outcomes of the DFT-based calculations. Interactions with first three coordination spheres (J_1, J_2, J_3) were considered, since the remainder are much smaller. As was already pointed out, the Pd-originated renormalization of J-parameters is the most pronounced for next NNs (J_2) and therefore we introduce biquadratic term only for this coupling. [2] The values which were extracted from the Fig. 3.6 and used for the model are shown in Table 3.1. It is seen that J'_2 is

TABLE 3.1: Set of parameters used for extended Heisenberg model (in mRy). The values are extracted from the results represented in Fig. 3.6.

J_1	J_2	J'_2	J_3
0.236	-0.902	-0.282	0.29

of the same order as bilinear exchange. Such situation is atypical, but not unique: for

[2] J'_2 manifests itself in the AFM state. It gives rise to the difference in the values of the effective parameters between parallel and antiparallel pairs of Fe spins.

example, a sizable value of the biquadratic term is necessary to explain properties of another class of Fe-based materials [153].

In order to check the applicability of the proposed model we came back to the results shown in Fig. 3.4, where the first manifestation of non-Heisenberg behavior was observed. We can express the magnetic energy per site as a function of θ, using Eq. (3.1). It is easy to show that it should have the following form:

$$E(\theta) = (2J_1 - 8J_3)\big[\cos(\theta) - 1\big] - 8J_2'\big[\cos^2(\theta) - 1\big]. \tag{3.2}$$

Here, biquadratic term plays a very important role and allows for existence of one additional minimum of this function at the position:

$$\theta_0 = \arccos\left[\frac{J_1 - 4J_3}{8J_2'}\right] \tag{3.3}$$

If we take a set of exchange parameters straight from the Table 3.1, then the overall profile of $E_{tot}(\theta)$ dependence will be reproduced, as seen in Fig. 3.9. With a slight

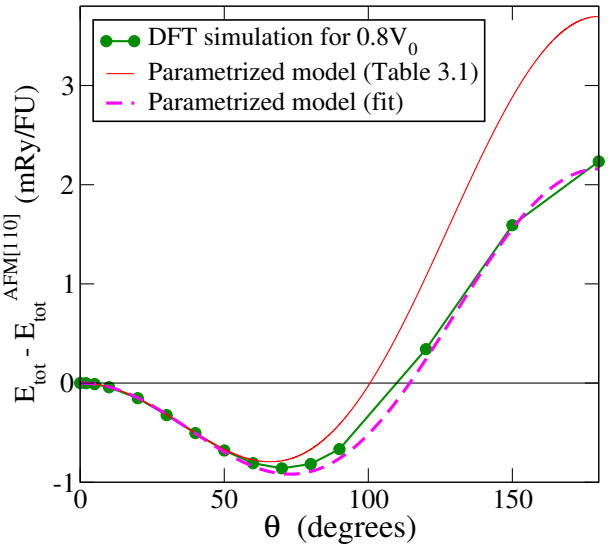


FIGURE 3.9: Comparison between $E(\theta)$ dependence (Fig. 3.4) obtained with self-consistent calculation and the one provided by Extended Heisenberg model. The parameterization of the latter is listed in Table 3.1. Parameters which provide an excellent fit are the following: $\{J_1, J_2, J_2', J_3\} \rightarrow$ {0.5, -0.902, -0.23, 0.26} (in mRy).

tuning of J-parameters one can achieve a perfect agreement with the results of the self-consistent calculations. This, however, is not our aim; The primary point here is that additional minimum θ_0 appears in a reasonable position. Present fact implies plausibility of our model.

3.5 Triple-Q phase

Once the model is parametrized (see Table 3.1), one can try to minimize magnetic energy given by Eq. (3.1). For this purpose we considered a 2×2×2 cell, which contains 8 spins. Each of them is characterized by two degrees of freedom (since its magnitude is fixed), so we have 16 parameters to tune. Due to spin rotational invariance we can fix two more of them. Such function can be minimized numerically on a modern computer.

This procedure provided us with a new ground state of the system, which is depicted in Fig. 3.10. The magnetic structure of this state corresponds to two interpenetrating

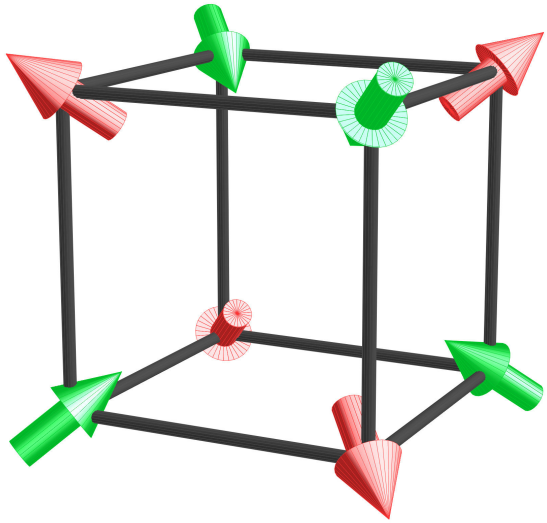


FIGURE 3.10: Proposed high-pressure magnetic order in $FePd_3$. Arrows denote iron magnetic moments and that of the same color form the so-called triple-Q phases. Note, that the state is invariant under simultaneous rotations of all spins through the same angles.

fcc lattices, whose spins form so-called triple-Q (3Q) states [43]. The angle between each pair of spins is $109^o28'$, hence the vectors point toward/opposite the vertices of an ideal tetrahedron. Analysis of the spin arrangement revealed that J_3 coupling (FM), which couples two fcc sublattices, is fully satisfied within such ordering. Remainder interactions have to compete with each other due to the geometrical frustration. Note, that negative sign of J_2' means that the interaction favors perpendicular spin orientation. This term is a driving force to the stabilization of a certain angle between spins.

In order to probe local stability of obtained spin structure, we have computed a dispersion of low-energy magnetic excitations (Fig. 3.11). According to the results, all

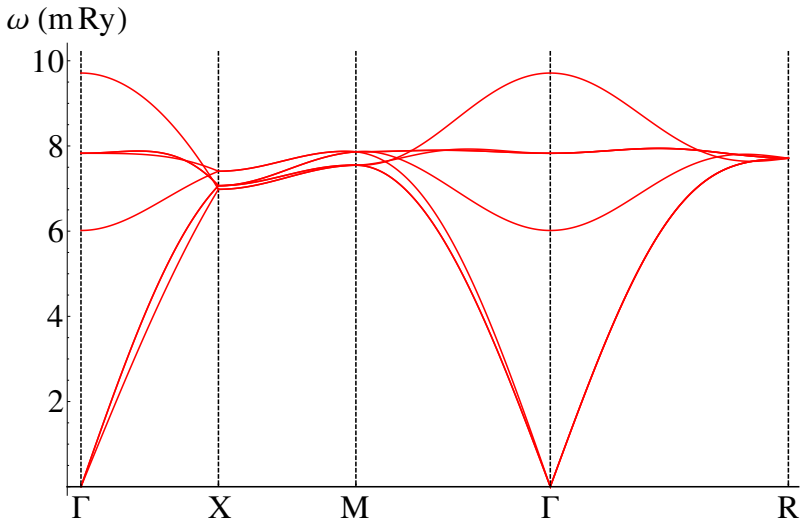


FIGURE 3.11: Frozen magnon dispersion of the 3Q state.

excitations have a positive energy, meaning that the state is stable. This is a remarkable fact, since all states which were studied before exhibited instabilities in their spectra. Second, there are several almost degenerate Goldstone modes obeying linear dispersion law at small values of the wave vector **q**. Present fact will be re-addressed in the next section.

However, up to now we have been working with the model Hamiltonian, which is supposed to reflect properties of a real compound under consideration. Finally, realistic electronic structure calculations for the 3Q state in compressed $FePd_3$ were performed. Magnitude of Fe magnetic moments was found to be $\approx 3\mu_B$, whereas Pd magnetization spontaneously disappeared during the self-consisteny process, which could be expected from the topology of the state. Upon compression, the suggested non-collinear state becomes lower in energy than the FM at small compressions (see Fig. 3.12). At higher pressure the 3Q state has the lowest total energy among all considered configurations.

It was shown before that stability of triple-Q state with respect to single-Q ones in fcc-based alloys can be related to nonlinear spin interactions [87] and/or presence of paramagnetic impurities [107]. In fact, both of these ingredients are present in $FePd_3$, so our findings are consistent with the established physical picture.

Observation of the 3Q state on $L1_2$ lattice was already reported, for instance, for $IrMn_3$ [145, 159]. Nonetheless, we found a more exotic magnetic order consisting of two 3Q phases, which are coupled ferromagnetically. To the best of our knowledge present

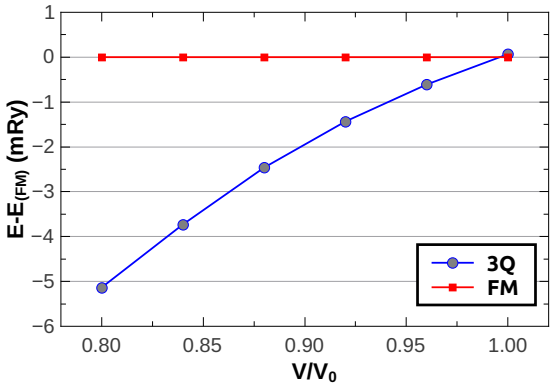


FIGURE 3.12: Relative total energy of the 3Q state in $FePd_3$ at various compressions. Results for FM solution are taken as reference.

spin structure was not observed in alloys with such a low concentration of intrinsically magnetic ions.

3.6 Relation to experiments

Experimentally, the 3Q states are not easy to distinguish from Néel antiferromagnets [98]. The measurement which helped to disentangle these two phases was proposed by Kawarazaki *et al.* [90] The method, however, requires certain elements which are the sources of the γ-rays. Thus for the case of $FePd_3$ a more useful way would be to use the Mössbauer effect in Fe, but this technique can not yield an unequivocal answer if the state is more complex than single-Q type [91].

First of all, we suspect that there should be an abrupt change in the shape of the spin-wave dispersion from parabolic to linear in $FePd_3$ under applied pressure. This would be the first indication of existence of the triple-Q state, which is necessary, but not sufficient.

Another external parameter which has to be thoroughly controlled during an experiment is the temperature. In Ref. [172] a complete vanishing of average Fe magnetization was observed in the NFS experiment under applied pressure. Present effect can be explained by a drop of T_c upon compression. A reliable *ab initio* evaluation of T_c of FM $FePd_3$ is already a difficult task and seems not to be solved in previous studies [23, 137]. Recent results on estimation of the T_c in MFA confirm its decrease upon the application of pressure [36], but it reaches the room temperature at lower volumes than observed

experimentally. Due to these contradictions from theoretical side, an experimental confirmation would be an optimal solution.

Another possible source of problems for such systems is a chemical disorder. The samples of $FePd_3$ are prepared by annealing and subsequent fast cooling (quenching). Therefore, some residual disorder can always remain in a real system. It was reported that the value of transition pressure in the alloy differs from one sample to another [173]. This fact may suggest that a small antisite disorder is present and affects a phase diagram of the compound under consideration. In principle, disorder can cause more complicated spin orderings or spin glass behavior.

3.7 Conclusions

$FePd_3$ was investigated theoretically by means of the DFT-based calculations. Analysis of different (in)commensurate magnetic configurations indicated a strong tendency to spin noncollinearity. Calculated exchange integrals between iron atoms were found to be strongly renormalized depending on Pd magnetization. As a result, magnetic properties are poorly described within classical Heisenberg model. We have extended this model by adding higher-order biquadratic couplings which are meant to mimic effect of highly paramagnetic impurities on Fe-Fe magnetic interactions. Solution of the proposed Hamiltonian corresponds to the 3Q magnetic order. Total energy DFT calculations for compressed $FePd_3$ confirm that this state has the lowest energy among studied. Hence, 3Q is a realistic candidate for a GS of the considered compound.

Essential ingredients which stabilize the 3Q states can be determined: (i) an existence of strong magnetically frustrated couplings in the system, which is J_2 in the present case; and (ii) admixture of higher-order interactions, favoring perpendicular spin alignment. The latter is supposed to appear in other alloys where $3d$ spins interact in paramagnetic medium formed by $4d$ elements, like Pd or Rh. Its not excluded that $5d$ metals (e.g. Au, Pt) can exhibit similar behavior. However, their valence states have much stronger SOC and therefore the analysis can not be done on the same footing as was done in present work. Effect of magnetocrystalline anisotropy can play an important role in this case (see e.g. [122, 157]).

Present study has shown that when it comes to noncollinear magnetism, finding of a GS is not an easy task for the DFT. Associated energy differences are relatively small (∼meV). Therefore, information about effective exchange couplings can be very useful. Instead of a "brute force" search of a GS, one can try to arrange spins in such a way that these couplings will be satisfied. However, limitations of this method (see Chapter 1) have to be taken into account; namely, there is, in general, no guarantee that the found stable solution is the global minimum.

The results presented in this Chapter are published in *Physical Review B* [103].

Chapter 4

Evaluation of stress in the DFT

4.1 Introduction

The problem of force and pressure in quantum systems was addressed by several authors since the very formulation of the quantum mechanics (for review, consult Ref. [112]). In 1927 Ehrenfest showed that the force acting on a particle is given by expectation value of the gradient of the potential [41]. Thus, a direct analogy with classical physics was pointed out. In the same spirit it was found that thermodynamical quantities in many-particle quantum systems are in the same relations as their classical counterparts. The so-called virial theorem, which states that the total pressure in the system is defined by the kinetic and potential energies was proven to hold on microscopic scale [54, 152]. Therefore, the stress in a quantum system is an intrinsic property to its ground state. The latter is known to be well-represented with a help of the DFT.

For this reason, in 1983 Nielsen & Martin [124, 125] developed a technique to extract information about the stress from a many-body Hamiltonian, which is generally written as:

$$\hat{H} = \sum_{i}^{n} \frac{p_i^2}{2m_i} + V_{int} + V_{outer}, \tag{4.1}$$

where the first term is total kinetic energy of n particles, the second one is internal part of the potential energy which is supposed to be intrinsic to the system. In our case

it is given by Coulombic interactions between particles. The last contribution to the potential energy V_{outer} arises from an external influence.

Upon strain, defined in Eq. (1.21), particle wavefunction is changed as follows [54]:

$$\Psi_\varepsilon(\vec{r}) = \frac{1}{\det \mid 1+\varepsilon \mid^{1/2}} \Psi\big((1+\varepsilon)^{-1}\vec{r}\big), \tag{4.2}$$

where the factor involving matrix determinant guarantees WFs normalization. It is also easy to show that the transformation of the momentum is given by (up to first order in ε):

$$p'_{i,\alpha} = p_{i,\alpha} - \sum_\beta \varepsilon_{\alpha\beta} p_{i,\beta}, \tag{4.3}$$

where i numerates particles and $\{\alpha, \beta\}$ denote projections on real axes $\{x, y, z\}$. The total energy associated with the Hamiltonian (Eq. (4.1)) will take the form:

$$\langle \Psi_\varepsilon \mid \hat{H} \mid \Psi_\varepsilon \rangle = \int \Psi^*(\vec{r}) \left[\sum_i^n \frac{p_i^2 - 2\varepsilon_{\alpha\beta} p_{i,\alpha} p_{i,\beta} + \varepsilon_{\alpha\beta}\varepsilon_{\alpha\gamma} p_{i,\beta} p_{i,\gamma}}{2m_i} \right] \Psi(\vec{r}) d\vec{r} + \int \Psi^*(\vec{r}) \Big[V_{int}\big((1+\varepsilon)\vec{r}\big) + V_{outer}\big((1+\varepsilon)\vec{r}\big) \Big] \Psi(\vec{r}) d\vec{r}. \tag{4.4}$$

According to the variational principle, the change in total energy with respect to the unperturbed state should be of the second order in strain, therefore the first variation must vanish:

$$\frac{\partial \langle \Psi_\varepsilon \mid H \mid \Psi_\varepsilon \rangle}{\partial \varepsilon_{\alpha\beta}} = 0 = \sum_i^n \langle \Psi \mid \frac{p_{i,\alpha} p_{i,\beta}}{m_i} - r_{i,\beta} \frac{\partial}{\partial r_{i,\alpha}} (V_{int} + V_{outer}) \mid \Psi \rangle. \tag{4.5}$$

Present approach is called "stress theorem". The term which contains V_{outer} is the stress exerted by the external environment and is defined analogously to the classical mechanics. Average stress, which is intrinsic to the quantum system, is given by a sum of kinetic and potential contributions:

$$T_{\alpha\beta} = T_{\alpha\beta}^{kin} + T_{\alpha\beta}^{pot}, \tag{4.6}$$

$$T_{\alpha\beta}^{kin} = -\sum_i \langle \Psi \mid \frac{p_{i,\alpha} p_{i,\beta}}{m_i} \mid \Psi \rangle, \tag{4.7}$$

$$T_{\alpha\beta}^{pot} = \sum_i \langle \Psi \mid r_{i,\beta} \frac{\partial}{\partial r_{i,\alpha}} V_{int} \mid \Psi \rangle. \tag{4.8}$$

Hence, the final expression contains only operators, defined for each particle. The authors showed that this quantity can be obtained using converged GS electron density as comes out from the DFT calculation. They predicted very accurately lattice constants, bulk moduli and elastic constants of Si, Ge and GaAs [126].

One of the directions for method's extension is related to the fact that $T_{\alpha\beta}$ does not represent the field nature of stress. Namely, due to averaging, the information about its space dependence is lost and therefore one has to reconsider the approach and introduce the $\vec{r}$-dependent stress density [125]. Its application was emphasized by Filippetti & Fiorentini [51, 52], who investigated stress variation at surfaces and interfaces. Nowadays, due to the wide use of epitaxial growth of samples, such studies can be of great interest. However, this quantity is beyond the scope of the present thesis, since it is dedicated primarily to bulk materials.

The stress tensor carries an important piece of information concerning system's preference for structural changes. The described method is realized in several DFT codes. Following the original paper by Nielsen & Martin [126], Eq. (4.7) and (4.8) are mostly implemented in PW codes in their reciprocal space form. Primarily, it is done so, since this representation is a more natural one for periodic systems. Thus realizations based on a real space treatment of stress are less studied in the literature.

In the present work we shall apply the stress theorem to a wavelets-based DFT package and show that there are no limitations for its computation in the real space. Then, the influence of nonlinear core correction [108] on the accuracy of pressure estimates will be addressed.

4.2 Stress contributions in the PSP formalism

As was already mentioned, the `BigDFT` is a real-space-based code which uses wavelets in conjunction with pseudotentials. We shall show explicit formulas for the stress tensor calculation in this particular realization.

First of all, it should be emphasized that summation in Eq. (4.7) runs over all particles in the system: both electrons and nuclei. Therefore, each term which contributes to the total energy also has an impact on the stress. Expressions for the stress tensor are

well-known and were studied by several authors. In the case of PSP-based approaches for the DFT, one has the following contributions to the stress:

- **Kinetic term**.

$$T^{kin}_{\alpha\beta} = -\sum_i f_i \int d\vec{r}\varphi^*_i(\vec{r})\frac{\partial}{\partial r_\alpha}\frac{\partial}{\partial r_\beta}\varphi_i(\vec{r}), \tag{4.9}$$

  where $\varphi_i(\vec{r})$ is the i-th KS (one-electron) wavefunction, f_i is its occupation number ($\in \{0, 1\}$).

- **Hartree term-originated stress**. Present component is easier to access in the Fourier space:

$$T^{H}_{\alpha\beta} = \frac{1}{2}4\pi e^2 \int d\vec{G}\left[\frac{2G_\alpha G_\beta}{G^2} - \delta_{\alpha\beta}\right]\frac{\mid \rho(\vec{G}) \mid^2}{G^2}, \tag{4.10}$$

  where $\vec{G}$ - is a vector of reciprocal space; $\rho(\vec{G})$ is a Fourier image of total electron density.

- **PSP contribution**. As was mentioned in Chapter 1, PSP has two parts. An isotropic term, called local, produces the following impact on the stress:

$$T^{\text{loc}}_{\alpha\beta} = -\sum_I \sum_{\vec{G}\neq 0} S_I(\vec{G})\rho^*(\vec{G})\left[\frac{\partial V^{\text{loc}}_I(\vec{G})}{\partial G^2}2G_\alpha G_\beta + V^{\text{loc}}_I(\vec{G})\delta_{\alpha\beta}\right], \tag{4.11}$$

  where I numerates nuclei, Z_I reads its charge, $S_I(\vec{G}) = \exp(-2\pi i\vec{G}\vec{R}_I)$ is a shift factor, associated with an ionic position $\vec{R}_I$.

  Whereas nonlocal part of the PSP, defined as $V(\vec{r}, \vec{r'})$, gives rise to another stress component, given by:

$$T^{\text{nl}}_{\alpha\beta} = E_{nl}[\Psi]\delta_{\alpha\beta} + \int d\vec{r}d\vec{r'}\Psi(\vec{r})\Psi(\vec{r'})\left[r_\beta\frac{\partial V(\vec{r}, \vec{r'})}{\partial r_\gamma}\delta_{\alpha\gamma} + r'_\beta\frac{\partial V(\vec{r}, \vec{r'})}{\partial r'_\gamma}\delta_{\alpha\gamma}\right], \tag{4.12}$$

  where Ψ is a many-body wavefunction of the system in its GS.

- **XC contribution (LDA/GGA)**. In the context of present thesis the most complex form of the XC functional, we operate with, is of GGA type. In this case the

expression for the tensor T is given by the following formula [30]:

$$T^{xc}_{\alpha\beta}[\text{GGA}] = \delta_{\alpha\beta}\int d\vec{r}\rho(\vec{r})\Big[\epsilon_{xc} - V_{xc}\Big] - \int d\vec{r}\frac{\partial(\rho\epsilon_{xc})}{\partial(\partial_\beta\rho)}\partial_\alpha\rho, \tag{4.13}$$

where ∂_γ is a γ-projection of the gradient, i.e. $\frac{\partial}{\partial r_\gamma}$.

- **Ion-ion (Ewald) part**. Interactions between point-like atomic charges contribute to the stress as follows:

$$T^{Ewald}_{\alpha\beta} = -\sum_{I\neq J}\frac{Z_I Z_J e^2}{2}\frac{(\vec{R}_I - \vec{R}_J)_\alpha(\vec{R}_I - \vec{R}_J)_\beta}{\mid \vec{R}_I - \vec{R}_J \mid^3}, \tag{4.14}$$

where $\vec{R}_I$ and Z_I denote position and charge of I-th nucleus, respectively.

Hence, each component can be computed independently from others. Such flexibility is advantageous, since some terms are easier to calculate in direct or reciprocal space. We shall balance between these two representations in order to achieve the highest performance without loss of the accuracy. A detailed derivation of the formulas, mentioned in this chapter, along with a strategy for their computation are presented in Appendix B. Relatively trivial parts are briefly discussed and computationally more challenging contributions are addressed in more detail. Note, that the expressions are given for unpolarized electron density, but the generalization for spin-polarized case is straightforward.

Present implementation is included in the standard `BigDFT` package, starting from its version `1.6`.

4.3 Tests and comparisons

4.3.1 Bulk Si

In order to check our implementation, first we considered bulk Si. Since `BigDFT` works with orthorhombic systems, a cell containing 8 Si atoms was constructed, as shown in Fig. 4.1(a). Bulk Si is a wide-band insulator, so accurate estimates of the main observables can be obtained with relatively small amount of $k-$points. To ensure convergence, we used 8×8×8 $k-$points for the BZ sampling. We compared our results with the

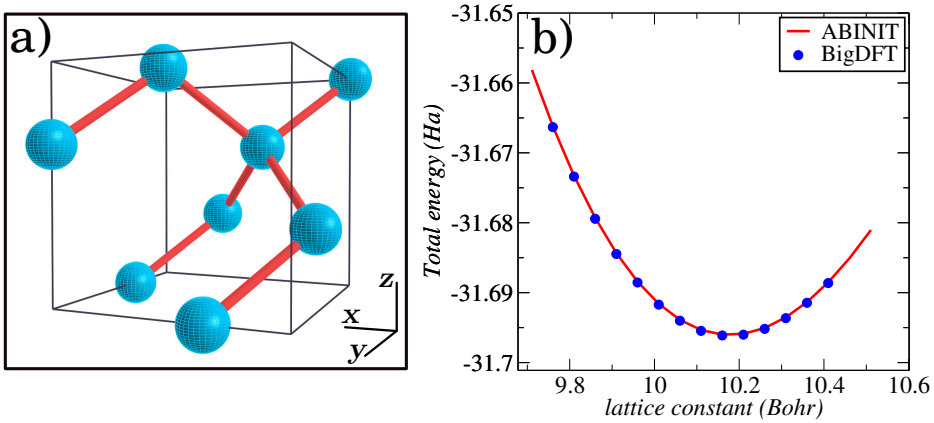


FIGURE 4.1: Panel "a": unit cell used for the calculation; "b": total energy of bulk Si as a function of lattice parameter calculated using different DFT codes. LDA functional, 8^3 k-point grid.

outcomes of a plane-wave code `ABINIT` [64, 65]. LDA-type PSP with Goedecker-Tutter-Hartwigsen (GTH) [62] parameterization was used for both sets of calculations.

First we varied the lattice parameter, preserving cubic crystal structure of the system. A comparison of the results, obtained with two codes, is shown in Fig. 4.1(b).

The agreement in absolute values of total energy is excellent. Note, that in order to obtain the same accuracy with a plane wave code, we had to use a higher cut-off as compared with the analog of `BigDFT` value.

Next, being sure that both programs yield the same GS, we have investigated the stress in the system. Cubic symmetry implies that any diagonal element of the stress tensor equals to the pressure. Moreover, in this case the latter is defined as follows:

$$P = -\frac{dE_{tot}}{dV}, \tag{4.15}$$

where V stands for a volume of the unit cell. Hence, the pressure can be directly extracted from the DFT calculation as a slope of the total energy, which allows us to compare it with the outcomes of the implemented "stress theorem". Results for this test are shown in Fig. 4.2. First of all, one can see that the stress tensor is in very good agreement with the one calculated by a plane-wave code. Equilibrium lattice constant corresponds to the minimum of the total energy (i.e. zeroth pressure) and equals to 10.18 Bohr. Present value is in good agreement with the one provided by full-potential calculations with the LDA-type functional [73]. In addition we show the volume variation

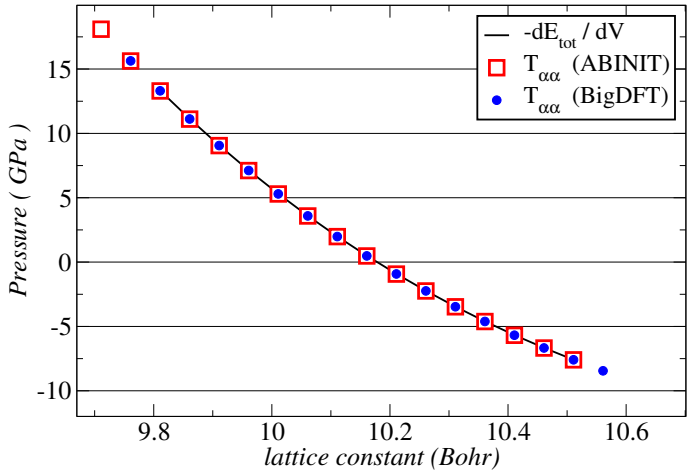


FIGURE 4.2: Calculated intrinsic pressure for different values of lattice parameter in bulk silicon. Results were obtained with the `BigDFT` and `ABINIT` codes.

of the total energy (Eq. 4.15), which precisely follows calculated curves. Current result clearly shows that the the stress tensor has a correct physical meaning.

4.3.2 $SrTiO_3$ and $LaAlO_3$

Next, we have tested our code on more complex materials. $SrTiO_3$ (STO) and $LaAlO_3$ (LAO) compounds have a perovskite structure, schematically shown in Fig. 4.3. These

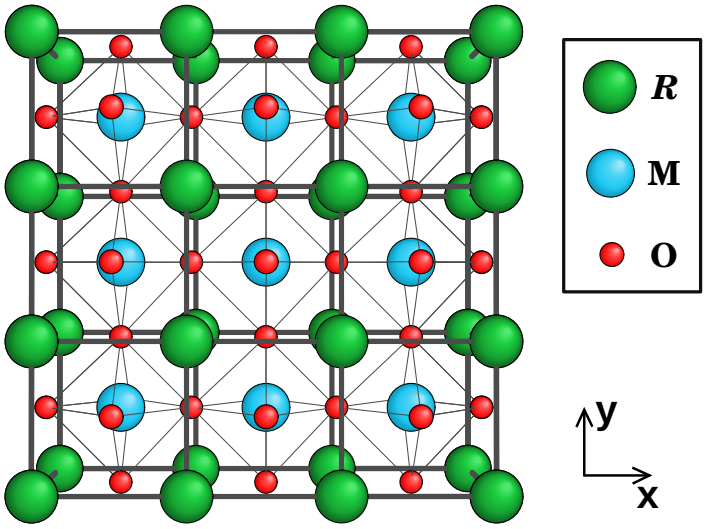


FIGURE 4.3: Crystal structure of RMO_3-type perovskite. R={La, Sr}, M={Ti, Al}.

systems are examples of nonmagnetic band insulators. However, it turned out once they are in contact, their interface becomes conducting [127]. Moreover, the indications

for emergence of magnetism [18] and superconductivity [138] at low temperatures were reported.

We have studied structural properties of the present compounds next to equilibrium. The stress tensor was calculated for bulk phases of LAO and STO for different volumes of the unit cell. Results, shown in Fig. 4.4, indicate that the lattice constants mismatch between

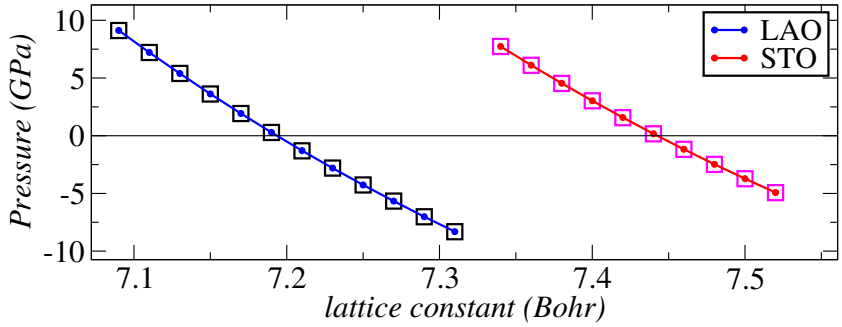


FIGURE 4.4: Calculated pressure for different values of lattice parameter in STO and LAO. Solid lines with circles show the results obtained with the `BigDFT` code. Outcomes of `ABINIT` are shown with opened squares. PBE functional was used for this set of calculations.

two structures is about 0.25 bohr, which is in fair agreement with prior studies [132]. Obviously, the tension should appear in epitaxially grown STO on LAO substrate, due to this difference in lattice parameters. As a perspective, it will be interesting to investigate the layer-resolved evolution of stress density. In this case wavelets form an optimal basis set, since, being defined in direct space, they are efficient for problems with isolated BCs. Present implementations are currently under development.

Next, we examined the convergence of the pressure and total energy estimates. We took advantage of the fact that in both PW and wavelets implementations the E_{tot} is variational with respect to certain parameters, which are PW energy cut-off (E_{cut}) and grid spacing (h grid), respectively. Hence, with increase of these quantities, the total energy strictly decreases (i.e. goes toward more negative values)[1]. The deviation in pressure versus E_{tot} convergence, obtained for STO are shown in Fig. 4.5. The curve which corresponds to `BigDFT` results passes below the one of `ABINIT` in the entire considered range of the total energy accuracy. For a given convergence of the total energy, the precision of the stress estimations is at least two times more accurate with our implementation. Present result indicates, first of all, that the stress tensor can

[1]Note that change in the BZ sampling does not meet this criterion, so the accuracy of the results has to be checked more carefully.

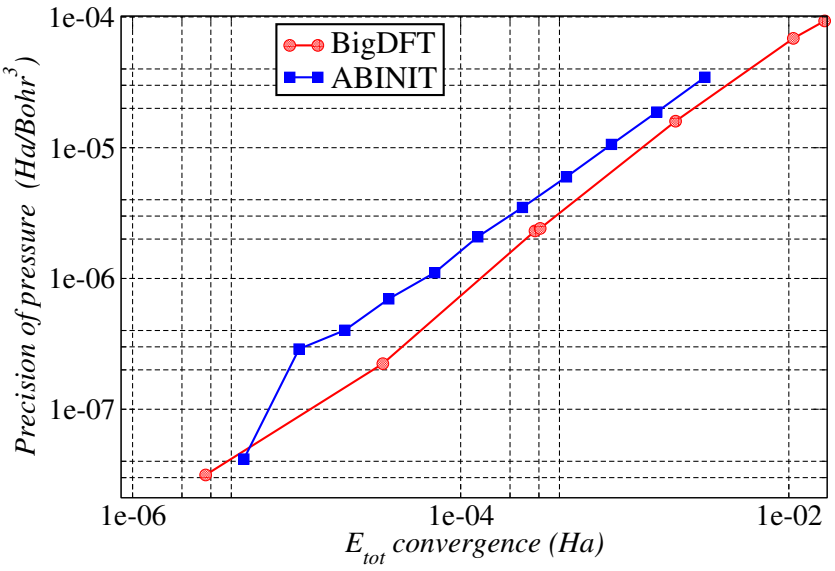


FIGURE 4.5: Convergence of pressure versus that of the total energy in bulk STO. Lattice parameter was fixed to the value of 7.3 bohr. The BZ was sampled with 6×6×6 $k-$points.

be evaluated in the direct space without any restrictions. Moreover, we report that present realization is characterized by a faster convergence of the results as compared with reciprocal space one.

In the studied cases we found that structural properties of a system next to equilibrium are well described by PSP-based DFT calculations as compared with the full-potential implementations. Thus the error, introduced due to the PSP substitution of a real ion, is not so important. However, high-pressure quantities are more sensitive to such approximation. Next section will be devoted to one of the way to overcome this issue.

4.4 NLCC and intrinsic stress

In the NLCC scheme, already mentioned in Chapter 1, the spin and charge densities (ρ_c) of core electrons is explicitly introduced in addition to valence ones. In a spirit of the GTH-type of PSPs, we shall also represent core density in a simple analytical form. It was chosen to be a gaussian function:

$$\rho_c(\vec{r}) = c_{\rm core}\frac{Z-Z_{ion}}{\left(\sqrt{2\pi}r_{\rm core}\right)^3}\exp\left[-\frac{r^2}{2r_{\rm core}^2}\right], \tag{4.16}$$

where parameters c_{core} and r_{core} are found during a fitting procedure, explained in Ref. [171]. Core charge distribution of a given element is defined once and for all, just like any other parameter of the PSP.

When the core density enters the total energy functional, the latter can be re-written as follows:

$$E_{\text{KS}} = \sum_i f_i \langle \psi_i \mid \left[-\frac{1}{2}\nabla^2 + V_H[\rho] + V_{xc}[\rho + \rho_c] + V^{psp} \right] \mid \psi_i \rangle - E_H[\rho] + E_{xc}[\rho + \rho_c] - \int d\vec{r} \rho(\vec{r}) V_{xc}[\rho + \rho_c](\vec{r}), \tag{4.17}$$

where ψ_i's are KS wavefunctions of valence electrons with occupation number f_i, whose density is denoted as ρ; E_{xc} and V_{xc} are the XC energy and potential, respectively ; V_H is the Hartree potential.

Regarding the stress tensor, the expressions for most of its contributions are the same as were described in the Section 4.2. The only term which has to be modified in the presence of core density is the XC component, which now takes the form:

$$T^{xc}_{\alpha\beta} = \delta_{\alpha\beta} E_{xc}[\rho + \rho_c] - \delta_{\alpha\beta} \int V_{xc}[\rho + \rho_c](\vec{r}) \rho(\vec{r}) d\vec{r} + \int V_{xc}[\rho + \rho_c](\vec{r}) r_\alpha \partial_\beta \rho_c(\vec{r}) d\vec{r} - \int d\vec{r} \left\{ n(\vec{r}) \dot{\varepsilon}[n](\vec{r}) \frac{\partial_\alpha n(\vec{r})}{|\nabla n(\vec{r})|} \right\} \partial_\beta n(\vec{r}) \Bigg|_{n=\rho+\rho_c}, \tag{4.18}$$

where $\dot{\varepsilon}[n] = \partial\varepsilon[n]/\partial(|\nabla n|)$ and ∂_α is an α-projection of the gradient. The expression implies a remarkable fact: off-diagonal components of $T_{\alpha\beta}$ which contain gradient of ρ_c has to be evaluated already on the level of LDA functionals. Whereas in conventional DFT such contributions appeared only in the case of GGA-type or more complex functionals. Hence, it can be expected that errors related with the choice of the XC approximation are partially excluded, thanks to the added correction.

4.5 NLCC and intrinsic stress: Results

An impact of NLCC on structural properties was investigated on a set of the following bulk systems: diamond-types Si and C, SiC, BN and LiCl. Again, for simplicity we

have chosen band insulators, but there are no limitations in application of the formalism to metallic (and magnetic) systems. We have chosen to work with the GGA(PBE) functional in present study, and its different realizations were adopted.

All-electron calculations were carried out using augmented plane wave plus local orbitals (APW + lo) method as implemented in the `WIEN2k` package. Reduced radii of atomic spheres were used in order to avoid their overlap up to the highest studied pressures. However, the radii were fixed for the entire range of volumes, so the total energies could be compared. Semicore states were treated as valence ones, since high compressions can lead to an overlap of their wavefunctions, which will affect the E_{tot} estimates. Inside the spheres, the partial waves were expanded up to $l_{max} = 10$. The number of plane waves was limited by a cut-off parameter $R_{MT}K_{max} = 9.0$ for all systems under consideration. The charge density was expanded in Fourier space up to $G_{max} = 14\ \sqrt{Ry}$. In most of calculations a very dense k-point grid (15×15×15) was used. Pressure was evaluated using directly Eq. (4.15). Results of all-electron calculations were taken as reference.

Then, the stress was extracted from two sets of calculations performed with the `BigDFT` package. The results, produced with standard the Hartwigsen-Goedecker-Hutter (HGH) [77] PSPs, were compared with the NLCC-including ones. Note that the parameters of these two types of the PSP are generated independently. Hence, the even the values, which are not related with the NLCC part, in general, do not coincide with each other. In most of calculations the cut-off parameter *hgrid* was set in such a way to achieve the total energy convergence about 10^{-5} Ha. An additional set of computations was conducted using the PAW [15] computational scheme, as implemented in the `VASP` package.

The results, shown in Fig. 4.6, clearly indicate that inclusion of NLCC to the bare HGH PSPs improves description of the stress. Present behavior is reported for all compounds under consideration. Another tendency is that the absolute error in calculated pressure grows with lattice contraction for all considered PSP-based computational methods. However, the deviation never exceeded 5% of the corresponding pressure value. In general, results of the PAW scheme show better agreement with all-electronc calculations as compared with HGH pseudopotentials. However, in case of carbon we found that NLCC is able to overcome this issue and achieve even higher accuracy of intrinsic stress estimates.

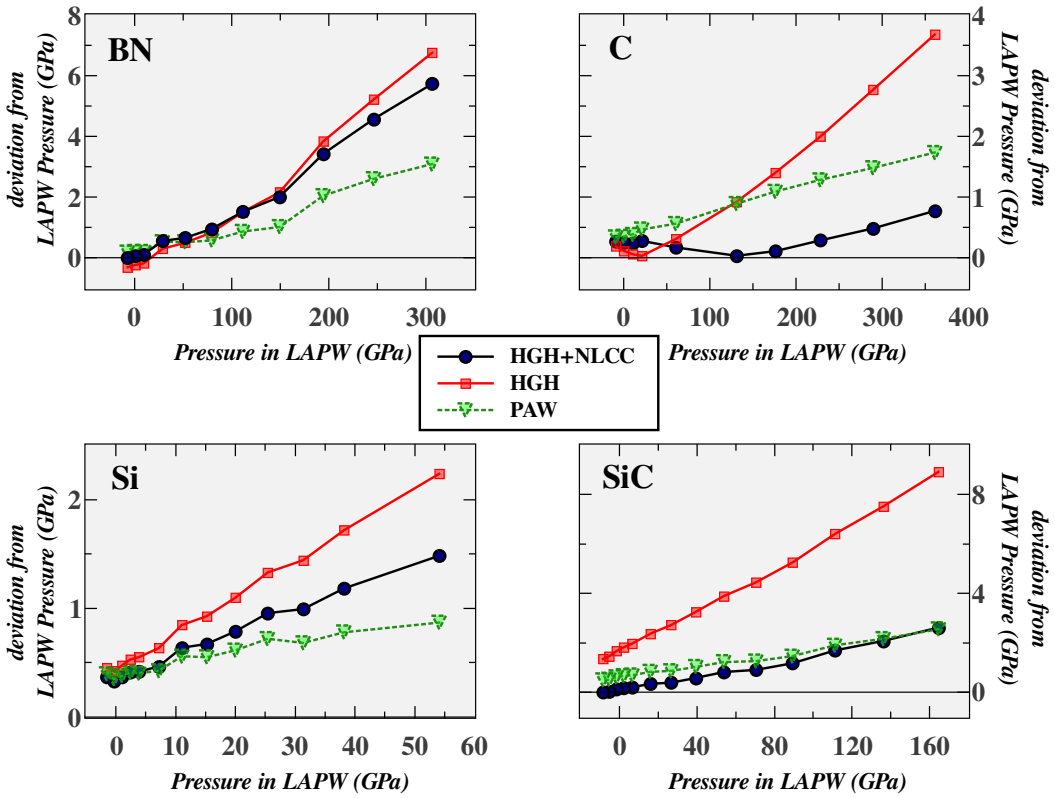


FIGURE 4.6: Intrinsic pressure, obtained using HGH, HGH+NLCC and PAW methods as compared with the outcomes of all-electron calculations. Absolute error with respect to the LAPW results is plotted along y axis.

4.6 Conclusions

A real-space formulation of the stress tensor in the DFT, so far modestly presented in the literature, was studied. We have described a strategy for efficient calculation of all contributions to the stress in a wavelet basis set. Present implementation shows a decent performance and precision in comparison with the PW-based ones.

According to the obtained results, the presence of PSPs affects structural properties and results into worse description of high-pressure region of volumes. On the other hand, system's properties next to equilibrium are relatively well represented. However, we report that taking into account core electrons "explicitly", as done in the NLCC and the PAW techniques, is able to significantly improve the results and provide almost the same accuracy as all-electron calculations. It is also worth emphasizing that approximations related with the choice of XC functional cause more severe inaccuracies in estimation of pressure than the use of the PSP. The proper choice of the functional for each particular case and thorough comparison with experiment is necessary.

As a perspective, we anticipate that study of the stress density can be rather insightful. For instance, present quantity can shed light on the stability of interfaces and epitaxially grown structures. In this context, use of real-space approach is obviously advantageous and presented developments are seen as the first step in this direction.

Results are published in the *Journal of Chemical Physics* [171].

Conclusions

In the present thesis first-principles calculations were applied to investigate the magnetic properties of transition metals and their alloys under pressure. This study led to the following conclusions.

In Chapter 2 it was shown how DFT calculations can be used to interpret the K-edge XMCD spectra measured in Ni, Co and FeCo alloys. We demonstrated that the pressure evolution of the experimental data should be compared with that of p-projected orbital moment. Moreover, we found that the spin and orbital components of the magnetization behave differently upon compression. It was shown that this observation can be explained from a simplified quantum-mechanical picture, where SOC is treated as a perturbation. As a result, L turns out to be inversely proportional to the band width and therefore decays faster than S as the pressure is raised.

We predicted an existence of antiferromagnetism among Fe spins in the high-pressure hcp phase of ordered FeCo alloy. Co magnetization disappears and, therefore, exhibits an itinerant magnet behavior. Both findings can explain the outcomes of XMCD experiments, but further experimental investigation is required.

In Chapter 3 the pressure-driven transition in $FePd_3$ was investigated. Analysis of the calculated exchange integrals revealed strong frustration due to competing interactions. We have proposed an extended Heisenberg model, which contains relatively strong biquadratic coupling to explain system's behavior. The enhancement of the biquadratic term is supposed to come from highly-paramagnetic Pd atoms, surrounding Fe moments. According to our results, $FePd_3$ undergoes a transition from the FM to the noncollinear 3Q state when compressed.

Finally, the method for the evaluation of intrinsic stress was realized in the `BigDFT` code. It allows us to calculate the shape of the system's unit cell under arbitrary external conditions. Moreover, it is shown that explicit treatment of core electrons can considerably reduce the errors introduced by the PSP. Thus the estimates of the structural properties can be improved.

Outlines and perspectives

It should be emphasized that the predictive power of the DFT is not ultimate. One of the main shortcomings is the absence of a strategy for finding the global minimum of the total energy, corresponding to the true GS of the system. Even if the electronic structure is calculated accurately and no instabilities are found in the phonon (and/or magnon) spectra, there is no guarantee that the considered state is not a metastable one. For this reason, it is always preferable to have sufficient amount of experimental data on the studied compound.

When magnetic properties are probed experimentally, attention has to be paid to the timescale of the experiment[2] It is also preferable to control both thermodynamic parameters – pressure and temperature – simultaneously. In this regard, spectroscopic techniques which use x-ray dichroism or Mössbauer effect are suitable tools for such studies.

In general, structural and magnetic properties of $3d$ metals are well described by means of *ab initio* methods. It opens a possibility for physicists to search for materials possessing particular characteristics. For instance, the DFT-based modeling is a widely used tool in the field of spintronics [24, 27]. Potentially, one can look for substitutions for the stainless steel, such a useful compound for industrial purposes.

Continuation of present work will be the study of various pressure-driven phenomena. One of the long-standing problems is the realization of the metal-insulator transitions (MITs), as suggested in Fe_2O_3 [101] and MnO [102]. These systems have a rather complex electronic structure and the treatment of dynamical correlations is important. On the other hand, it is known that structural changes can significantly affect the MIT mechanism [131]. As long as the LDA+DMFT method is concerned, the comparison of

[2] This is an important point when one estimates the local magnetization (see e.g. Ref. [166]).

the total energies of different crystal structures is not straightforward due to so-called "double counting problem" [89]. Recently realized techniques, such as GW+DMFT [10], do not suffer from this issue and are very promising. Such calculations are computationally demanding and therefore development of efficient algorithms is a necessary initiative in the advancement of electronic structure modeling.

Appendix A

General equations for the spin wave energies

A.1 Collinear magnets with several sublattices

In the presence of several magnetic sublattices in a crystal the equation of motion should be written in the more general way:

$$\frac{d\hat{\vec{S}}_j^l}{dt} = -\frac{1}{\hbar}\left[\vec{B}_j \times \hat{\vec{S}}_j^l\right] \tag{A.1}$$

where $\hat{\vec{S}}_j^l$ is the operator of j-th magnetic moment in the l-th sublattice, $\vec{B}_j$ is the effective field acting on the corresponding spin.

The Heisenberg Hamiltonian defined in multi-subblattice case can be written as:

$$\hat{H} = -\sum_{l,l'}\sum_{\substack{i\in l' \\ j\in l}} J_{ij}^{ll'}\,\hat{\vec{S}}_i^{l'}\,\hat{\vec{S}}_j^{l} \tag{A.2}$$

where $J_{ij}^{ll'}$ is the exchange interaction parameter between i-th magnetic moment belonging to the sublattice l' and j-th moment from sublattice l.

Thus the produced effective field takes the form:

$$\vec{B}_j = -\frac{\partial E}{\partial \vec{S}_j^l} = 2\sum_{i\in l'} J_{ij}^{ll'}\,\hat{\vec{S}}_i^{l'} \tag{A.3}$$

Substituting Eq. (A.3) into Eq. (A.1) , we obtain the following expression:

$$\hbar \frac{d\left[\hat{S}_j^l\right]_\alpha}{dt} = -2 \sum_{i \in l'} J_{ij}^{ll'} \varepsilon_{\alpha\beta\gamma} \left[\hat{S}_i^{l'}\right]_\beta \left[\hat{S}_j^l\right]_\gamma \tag{A.4}$$

where $\{\alpha, \beta, \gamma\} = \{ x, y, z\}$ is a set of projections and ε is the Levi-Civita tensor.

If we restrict ourselves to the low-energy excitations, the deviation of S_z from its initial value (S_x and S_y) can be considered as a small quantity and hence we can approximate $S_z^l \sim |S^l| \equiv S^l$. Then we decouple the above system of equations using transformation to the $S_\pm = S_x \pm i S_y$ operators.

At this stage one obtains:

$$\hbar \frac{d\left[\hat{S}_j^l\right]_\pm}{dt} = -2 \sum_{l'} \sum_{i \in l'} J_{ij}^{ll'} (\mp i) \left\{ S_j^l \left[\hat{S}_i^{l'}\right]_\pm - S_i^{l'} \left[\hat{S}_j^l\right]_\pm \right\} \tag{A.5}$$

After that we can use the system periodicity and perform so-called Lattice Fourier Transform (LFT):

$$\left[\hat{S}_{\vec{q}}^l\right]_- = \frac{1}{\sqrt{N}} \sum_{j \in l} \exp\left(-i\vec{q} \cdot \vec{R}_j^l\right) \left[\hat{S}_j^l\right]_- \tag{A.6}$$

The application of time-dependent Fourier transform ($\frac{\hbar}{i}\frac{d}{dt} \to \hbar\omega$) results into the following system of equation:

$$\hbar\omega \left[\hat{S}_{\vec{q}}^l\right]_- = -2 \sum_{l'} \sum_{i_{l'}} J_{ij}^{ll'} \left\{ \exp\left[i\vec{q} \cdot \left(\vec{R}_i^{l'} - \vec{R}_j^l\right)\right] S_j^l \left[\hat{S}_{\vec{q}}^{l'}\right]_- - S_i^{l'} \left[\hat{S}_{\vec{q}}^l\right]_- \right\} \tag{A.7}$$

Now we can define the Fourier image of the exchange parameters as:

$$J^{ll'}(\vec{q}) = \sum_{i \in l'} \exp\left[i\vec{q} \cdot \left(\vec{R}_i^{l'} - \vec{R}_j^l\right)\right] J_{ij}^{ll'} \tag{A.8}$$

Let us split this system of equations in diagonal and off-diagonal parts, using the following definition of the total interaction of the spin from sublattice l with the sublattice

l' :

$$J_0^l(l') = \sum_{i \in l'} J_{ij}^{ll'} \tag{A.9}$$

Resulting formula takes the form:

$$\hbar\omega \left[\hat{S}_{\vec{q}}^l\right]_- = -2 \sum_{l' \neq l} J^{ll'}(\vec{q}) S_j^l \left[\hat{S}_{\vec{q}}^{l'}\right]_- + 2 \left\{ (\sum_{l'} S_i^{l'} J_0^l(l')) - J^{ll}(\vec{q}) S_j^l \right\} \left[\hat{S}_{\vec{q}}^l\right]_- \tag{A.10}$$

Now we have to take into account the fact that exchange integrals are calculated within Lichtenstein's approach [105], where the Heisenberg Hamiltonian is in the following form:

$$\hat{H}_M = -\sum_{ij} \widetilde{J}_{ij} \hat{\vec{e}}_i \hat{\vec{e}}_j \tag{A.11}$$

where $\hat{\vec{e}}_i$ is operator of the unit vector along the direction of the magnetization on i-th site. In the case of several sublattices the magnitude of spin moment can be different, so it is useful to rescale them before insertion into the Eq.(A.10):

$$J_{ij} = \frac{\widetilde{J}_{ij}}{S_i S_j} \tag{A.12}$$

The final expression is given by:

$$\boxed{\hbar\omega \left[\hat{S}_{\vec{q}}^l\right]_- = -2 \sum_{l' \neq l} \widetilde{J}^{ll'}(\vec{q}) \frac{\left[\hat{S}_{\vec{q}}^{l'}\right]_-}{S^{l'}} + 2 \left\{ (\sum_{l'} \widetilde{J}_0^l(l')) - \widetilde{J}^{ll}(\vec{q}) \right\} \frac{\left[\hat{S}_{\vec{q}}^l\right]_-}{S^l}} \tag{A.13}$$

Then knowing $J(q)$ at each q-point one has to diagonalize the corresponding matrix in order to obtain spin wave energies $\hbar\omega(\vec{q})$.

Eq.((A.13)) can be applied to ferromagnetic systems with arbitrary number of magnetic sublattices as well as to the antiferromagnetic systems. The only difference is that in the latter case case the corresponding matrix is not symmetrical. For instance in the case of two antiferromagnetic sublattices (A and B) the matrix to be considered is of the following form:

$$\begin{pmatrix} -J^{AA}(\vec{q}) + J^{AA}(0) - J^{AB}(0) & -J^{AB}(\vec{q}) \\ J^{AB}(\vec{q}) & J^{BB}(\vec{q}) - J^{BB}(0) + J^{BA}(0) \end{pmatrix}. \tag{A.14}$$

It has to be understood, that in this case the matrix is written in the following basis: $\{S_+^A, S_-^B\}$. Hence, strictly speaking, one has to perform Bologyubov transformation in order to couple "+" components. However, the correct spectrum is already contained in the expression Eq. (A.14).

A.2 Noncollinear magnetic structures

In case of non-collinear magnetic systems one has to define a local coordinate system for each spin, such that new z-axis lies along the corresponding spins direction. Let us define the corresponding unitary transformation matrix which is related to the i-th spin as $\hat{U}_i$.

Using this matrix a scalar product of two non-collinear spins can be re-expressed as:

$$\vec{S}_i \cdot \vec{S}_j = \hat{U}_i\vec{S}_i \cdot \hat{U}_i\vec{S}_j = \hat{U}_i\vec{S}_i \cdot \hat{U}_i\hat{U}_j^{-1} \cdot \hat{U}_j\vec{S}_j = (0;0;S_i) \cdot \hat{T}_{ij} \cdot (0;0;S_j)^t, \tag{A.15}$$

where $\hat{T}_{ij} = \hat{U}_i\hat{U}_j^{-1}$ is a matrix which connects reference frames i and j. Such form of scalar products becomes advantageous, when deviations of moments are introduced.

In this case a tilt of each spin in its own reference frame can be treated as a small parameter :

$$\vec{e}_i = \big(0;0;S\big) \quad \rightarrow \quad \vec{e_i}' = \left(S_{ix}; S_{iy}; S - \frac{S_{ix}^2 + S_{iy}^2}{2S}\right) \tag{A.16}$$

where $\vec{S}_{ix}$ and $\vec{S}_{iy}$ are components related to the spin waves. With respect to these new variables the Heisenberg Hamiltonian (Eq.(1.23)) appears to be in quadratic form. Thus the produced effective fields are linear quantities equation of motion leads to linear system of equations:

$$\begin{cases} \frac{dS_{ix}}{dt} = -\frac{1}{\hbar}B_{iy} \\ \frac{dS_{iy}}{dt} = \frac{1}{\hbar}B_{ix}. \end{cases} \tag{A.17}$$

Hence for N spins there are $2N$ degrees of freedom, related to x and y components of spin waves, and this defines the dimension of the matrices which have to be diagonalized.

Appendix B

Derivation of expressions for stress tensor in the DFT

A thorough derivation of majority of formulas mentioned in Chapter 4 will be presented. We shall remain the same order of different contributions to the stress, as in the main text.

B.1 Kinetic stress

Taking into account that many-body WF in the DFT is a product of one-electron ones (like in Eq. (1.2)), it is easy to show that expression for kinetic part of the stress, generally defined by Eq. (4.7), will reduce to Eq. (4.9). The KS WFs, which we have to deal with, are three-dimensional objects. Since one dimensional function is represented via wavelet and scaling function, the corresponding 3D basis set is built up as a tensor product of those one-dimensional functions. There are 8 possible combinations of ϕ's and ψ's in this case (see e.g. Ref. [59]) and they form so-called mixed representation.

Clearly, diagonal coefficients of $T^{kin}_{\alpha\alpha}$ coincide with projections of the total kinetic energy on Cartesian axes. Hence, these quantities are already computed on each iteration of the DFT calculation. Matrix elements of the kinetic energy operator between the basis functions of the mixed representation are calculated analytically, following the method described in Ref. [13]. Using wavelets algebra one can derive an eigenvalue equation for these coefficients. Off-diagonal elements of T^{kin} can be found in the same manner.

In this case one has to deal with the integrals of the following type:

$$K_i = \int dx \phi(x) \frac{d}{dx} \phi(x - i) \tag{B.1}$$

It is easy to show, using Eq. (1.19), that one eventually gets the following relation:

$$K_i = \sum_{\nu\mu} 2 h_\nu h_\mu K_{2i+\mu-\nu}. \tag{B.2}$$

Hence, K_i terms can be computed analytically once and for all. These coefficients are defined uniquely by wavelets filters h and g.

B.2 Stress tensor from the Hartree energy

By definition (Eq. (4.8)), this contribution is defined as:

$$T^H_{\alpha\beta} = \int d\vec{r} \rho(\vec{r}) r_\beta \frac{\partial}{\partial r_\alpha} V_H(\vec{r}), \tag{B.3}$$

where Hartree potential V_H is given in its general form:

$$V_H(\vec{r}) = \int d\vec{r'} \rho(\vec{r'}) \hat{\mathbf{G}}(\vec{r} - \vec{r'}), \tag{B.4}$$

where $rho(\vec{r})$ is the total electron density and $\hat{\mathbf{G}}$ denotes the Green's function of the corresponding Laplace operator.

Eq. (B.3) involves the integral of the function, which we shall define as:

$$F(\vec{r}) = \rho(\vec{r}) r_\beta \frac{\partial}{\partial r_\alpha} V_H(\vec{r}), \tag{B.5}$$

In reciprocal space such integral will correspond to the zeroth component of the Fourier image of function F (i.e. $\tilde{F}(\vec{G} = 0)$).

Let us represent the function $F(\vec{r})$, as a product of two functions:

$$f(\vec{r}) = \rho(\vec{r}) r_\beta \tag{B.6}$$

$$g(\vec{r}) = \frac{\partial}{\partial r_\alpha} V_H(\vec{r}). \tag{B.7}$$

Reciprocal space counterparts of these expressions are given by:

$$\tilde{f}(\vec{G}) = \int d\vec{r}\rho(\vec{r})r_\beta e^{-i\vec{G}\vec{r}} = i\frac{\partial}{\partial G_\beta}\rho(\vec{G}) \tag{B.8}$$

$$\tilde{g}(\vec{G}) = iG_\alpha\tilde{V}_H(\vec{G}) = iG_\alpha\tilde{\rho}(\vec{G})\tilde{\hat{\mathbf{G}}}(\vec{G}). \tag{B.9}$$

Multiplication of f and g in real space will correspond to a convolution in the Fourier one. Hence, we can write an expression for zeroth component of our function under consideration as:

$$\tilde{F}(\vec{G}=0) = -i^2\int d\vec{G}'G'_\alpha\rho(\vec{G}')\hat{\mathbf{G}}(\vec{G}')\frac{\partial\rho(-\vec{G}')}{\partial G'_\beta} = $$

$$= \int d\vec{G}\Bigg[\frac{\partial}{\partial G_\beta}\Big(G_\alpha \mid \rho(\vec{G}) \mid^2 \hat{\mathbf{G}}(\vec{G})\Big) - $$

$$\int d\vec{G}\delta_{\alpha\beta} \mid \rho(\vec{G}) \mid^2 \hat{\mathbf{G}}(\vec{G}) + G_\alpha \mid \rho(\vec{G}) \mid^2 \frac{\partial\hat{\mathbf{G}}(\vec{G})}{\partial G_\beta} + G_\alpha\frac{\partial\rho(\vec{G})}{\partial G_\beta}\hat{\mathbf{G}}(\vec{G})\rho(-\vec{G})\Bigg]. \tag{B.10}$$

Surface-type integral is assumed to vanish. Then, we can benefit from the fact that $\rho(\vec{r})$ is a purely real function and therefore the following relation is obeyed: $\rho^*(\vec{G}) = \rho(-\vec{G})$.

Finally, one obtains:

$$T^H_{\alpha\beta} = \tilde{F}(\vec{G}=0) = \frac{-1}{2}\int d\vec{G}\Bigg[G_\alpha\frac{\partial\hat{\mathbf{G}}(\vec{G})}{\partial G_\beta} + \delta_{\alpha\beta}\hat{\mathbf{G}}(\vec{G})\Bigg] \mid \rho(\vec{G}) \mid^2 . \tag{B.11}$$

The expression is rather general and can, in principle, be applied to different boundary conditions. In a particular case of 3D BCs, the Fourier image of the Hartree potential is diagonal in $\vec{G}$-space and is given by:

$$\tilde{V}_H(\vec{G}) = \frac{4\pi e^2\rho(\vec{G})}{G^2} \tag{B.12}$$

Inserting this expression into Eq. (B.11) brings us to the following formula:

$$T^H_{\alpha\beta} = \frac{1}{2}4\pi e^2\int d\vec{G}\Bigg[\frac{2G_\alpha G_\beta}{G^2} - \delta_{\alpha\beta}\Bigg]\frac{\mid \rho(\vec{G}) \mid^2}{G^2}, \tag{B.13}$$

The only quantity which is required for evaluation of stress is the Fourier image of the electron density ($\rho(\vec{G})$), which can be computed efficiently with the help of the FFT.

B.3 Local part of the PSP

In the GTH (or HGH) pseudopotentials, employed in the `BigDFT`, the local part of the PSP consists of two terms:

$$V^{psp}(\vec{r}) = \sum_I V_I^{\mathrm{erf}}(\vec{r}) + V_I^g(\vec{r}), \tag{B.14}$$

$$V_I^{\mathrm{erf}}(\lambda_I) = -\frac{Z_{ion}}{r_{loc}}\frac{1}{\lambda}\mathrm{erf}\left(\frac{\lambda_I}{\sqrt{2}}\right), \tag{B.15}$$

$$V_I^g(\lambda_I) = e^{-\frac{{\lambda_I}^2}{2}}(C_1 + C_2{\lambda_I}^2 + C_3{\lambda_I}^4 + C_4{\lambda_I}^6), \tag{B.16}$$

where I denotes ions, Z_{ion} reads ionic charge, r_{loc} is the localization radius, $\lambda_I = \frac{|\vec{r}-\vec{R}_I|}{r_{loc}}$ and $\vec{R}_I$ is the ionic position.

Associated contributions to the stress can be computed independently. Moreover, as it will be shown, the real space treatment is a more appropriate one for gaussian part of the PSP.

B.3.1 Long-range part

The long range (error function) part of stress can not be evaluated in a real space, because of the occurence of a surface term which should vanish due to system periodicity. Hence, the most rigorous way is to calculate this contribution in reciprocal space. By definition, V^{erf} is the solution of the Poisson equation for a Gaussian-type density, which is given by:

$$\rho_e(\lambda_I) = -\frac{1}{(2\pi)^{3/2}}\frac{Z_I}{r_{loc}^3}\exp\left(-\frac{\lambda_I^2}{2}\right). \tag{B.17}$$

Its Fourier image is known to be:

$$\rho_e(\vec{G}) = Z_I \exp\left(-2\pi^2 r_{loc} G^2\right). \tag{B.18}$$

Therefore, the Fourier image of the corresponding potential takes the form:

$$V_I^{\mathrm{erf}}(\vec{G}) = -\frac{\rho_e(\vec{G})}{\pi G^2}. \tag{B.19}$$

Being the function of G^2, the derivative of V_e^I with respect to its argument can be calculated straightforwardly:

$$\frac{\partial V_I^{\text{erf}}(G^2)}{\partial G^2} = \frac{Z_I}{\pi G^2}\exp\left(-2\pi^2 r_{loc} G^2\right)\left[\frac{1}{G^2} + 2\pi^2 r_{loc}\right]. \tag{B.20}$$

Reciprocal space version of Eq. (4.8) is given directly by Eq. (4.11). Hence, the final expression for the long range contribution is obtained analytically.

B.3.2 Short-range part

Gaussian part of the pseudopotential can be calculated in the direct space. Using a simple chain rule for derivatives, it is easy to show that:

$$\frac{\partial}{\partial r_\alpha} V_I^g(\lambda_I) = \frac{\partial V_I^g}{\partial \lambda_I}\frac{\partial \lambda_I}{\partial \mid \vec{r} - \vec{R}_I \mid}\frac{\partial \mid \vec{r} - \vec{R}_I \mid}{\partial r_\alpha} = \\ = \frac{r_\alpha}{\lambda_I r_{loc}} \cdot \frac{\partial V_I^g}{\partial \lambda_I}. \tag{B.21}$$

Using the explicit form of the potential V^g, given by Eq. (B.16), the first term can be calculated analytically:

$$\frac{\partial V_I^g}{\partial \lambda_I} = \exp\left(-\frac{\lambda_I^2}{2}\right)\sum_{i=1}^{4}\left[2\frac{i-1}{\lambda_I^2} - 1\right]C_i(\lambda_I)^{2i-1}. \tag{B.22}$$

The final expression is relatively simple for implementation. In the code this is done at the stage of the calculation of interatomic forces.

However, the zeroth Fourier component of the integrand of Eq. (4.8) has to be subtracted from the diagonal elements of the stress tensor. This term is given by:

$$E_0 = -\delta_{\alpha\beta}\sum_I \rho^*(\vec{G}=0)\cdot V_I^g(\vec{G}=0) \equiv -\delta_{\alpha\beta}\cdot Q_{tot}\cdot\sum_I \int V_I^g(\vec{r})d\vec{r}, \tag{B.23}$$

where Q_{tot} is the total valence charge. An account for this term is essential for correct stress evaluation and must be respected.

B.4 Non-local part of the PSP

The total energy contribution coming from the non-local PSP depends on the coordinates of two particles. Hence, its change induced by the strain (Eq. (1.21)) can be written as follows:

$$E_{nl}[\Psi_\varepsilon] = \int d\vec{r}d\vec{r'}\Psi^*_\varepsilon(\vec{r})V(\vec{r},\vec{r'})\Psi_\varepsilon(\vec{r'}) = \\ = \int d\vec{r}d\vec{r'} \mid 1+\varepsilon \mid \Psi^*(\vec{r})V((1+\varepsilon)\vec{r},(1+\varepsilon)\vec{r'})\Psi(\vec{r'}). \tag{B.24}$$

The first-order variation of this quantity is related to the stress. It is given by a general expression, shown in Eq. (4.12). In a separable type of the PSP [95], like GTH, for instance, $V^{\text{nl}}(\vec{r},\vec{r'})$ has the following form:

$$V^{\text{nl}}(\vec{r},\vec{r'}) = \sum_{ij} h^{(l)}_{ij} p_i(\vec{r}) p_j(\vec{r'}) \tag{B.25}$$

where p_i is the projector operator on a certain state i, $h^{(l)}_{ij}$ is a symmetric matrix for each value of l. Projectors have a form of Gaussian-like (short range) functions, centered at the atomic position. Thanks to this property of the non-local PSP, one can simplify the expression for the stress:

$$\frac{\partial E_{nl}[\Psi_\varepsilon]}{\partial \varepsilon_{\alpha\beta}} = E_{nl}[\Psi_\varepsilon]\delta_{\alpha\beta} + 2\sum_{ij} h^{(l)}_{ij} \int d\vec{r}\Psi(\vec{r}) r_\beta \frac{\partial p_i(\vec{r})}{\partial r_\alpha} \int d\vec{r'} p_j(\vec{r'})\Psi(\vec{r'}) \tag{B.26}$$

It can be shown that this formula can be computed without any loss of computers performance. To shorten the notations, we introduce two quantities:

$$S^i_{\alpha\beta} = \int d\vec{r}\Psi(\vec{r}) r_\beta \frac{\partial p_i(\vec{r})}{\partial r_\alpha}, \tag{B.27}$$

$$C_j = \int d\vec{r} p_j(\vec{r})\Psi(\vec{r}). \tag{B.28}$$

It is worth mentioning that integration in real space should be done with respect to the atomic position, i.e. $\vec{r} \to (\vec{r} - \vec{R}_i)$. Since the total energy contribution can be expressed using these coefficients as:

$$E_{nl} = \sum_{ij} h^{(l)}_{ij} C_i C_j, \tag{B.29}$$

we can also re-write the formula for the stress tensor:

$$T_{\alpha\beta}^{nl} = \frac{1}{V}\sum_{ij} h_{ij}^{(l)}\Big[2S_{\alpha\beta}^{i} + C_i\Big]C_j. \tag{B.30}$$

As was already mentioned, in the GTH class of pseudopotentials the projectors are written in terms of gaussians and polynomials of the coordinates, such as :

$$\exp\left(-cr^2\right)\cdot x^{l_x}y^{l_y}z^{l_z}. \tag{B.31}$$

Therefore, any scalar product of the projector and a wavefunction in Daubechies basis can be factorized to a product of three one-dimensional integrals.

Now we can benefit from the fact that the derivatives of the projectors are already computed in the `BigDFT` code for the purpose of forces evaluation. So the following quantities are at hand:

$$\frac{\partial p}{\partial x} = \exp\left(-cr^2\right)\cdot \mathbf{P}(l_x, l_y, l_z), \tag{B.32}$$

where $\mathbf{P}$ is a polynomial of the following structure :

$$\mathbf{P}(l_x, l_y, l_z) = \sum_{ijk} \lambda_{ijk} x^{l_x+i} y^{l_y+j} z^{l_z+k} \tag{B.33}$$

and λ_{ijk} are real coefficients. The quantities required for stress tensor calculation have a slightly different form. Nevertheless, it is easy to see that the expressions are related, e.g.:

$$y\frac{\partial p}{\partial x} = \exp\left(-cr^2\right)\sum_{ijk} \lambda_{ijk} x^{l_x+i} y^{(l_y+1)+j} z^{l_z+k} = \mathbf{P}(l_x, l_y+1, l_z). \tag{B.34}$$

Thus there is no need to compute any additional integrals, since the only difference with calculation of the derivative of the projector is in the change of one of the coefficients in a corresponding polynomial. This computational scheme is especially advantageous when one has to deal with pseudopotentials containing many projectors of different l number (e.g. heavy elements).

B.5 XC contribution

Formula for XC contribution to stress (Eq. (4.13)) is straightforward to obtain by inserting the definition of the potential provided by Eq. (1.14) into Eq. (4.8). Evaluation of present expression can be done in a real space. The most challenging part which is associated with the calculation for density gradients.

One can see that the XC stress consists of two contributions. The first term in this expression appears already on the level of LDA-type functionals. Those are diagonal matrix elements, which do not cause changing of the unit cell's shape (deformation). Certainly, this is a shortcoming of a given approximation, but is a natural consequence of using an 'ideal gas' expression for correlation effects. However, it is seen that introduction of the gradients permits the emergence of off-diagonal elements of the stress tensor. Thus, with the GGA the XC-originated stress becomes more detailed and presumably reflects physics of real systems in a more appropriate way.

B.6 Ion-ion impact

Ion-ion energy contribution to stress is one of the easiest to calculate. This term does not involve electron density and therefore does not change during the self-consistent loop. The corresponding expression is simply given by:

$$T_{\alpha\beta}^{Ewald} = -\sum_{I\neq J} \frac{Z_I Z_J e^2}{2} \frac{(\vec{R}_I - \vec{R}_J)_\alpha (\vec{R}_I - \vec{R}_J)_\beta}{\mid \vec{R}_I - \vec{R}_J \mid^3}. \tag{B.35}$$

Present contribution is called Ewald stress. In the `BigDFT`, present formula is computed at the stage of initialization of the calculation.

Bibliography

[1] I. A. Abrikosov, P. James, O. Eriksson, P. Söderlind, A. V. Ruban, H. L. Skriver, and B. Johansson. Magnetically induced crystal structure and phase stability in $\mathrm{fe}_{1-c}\mathrm{co}_c$. *Phys. Rev. B*, 54:3380–3384, Aug 1996.

[2] I. A. Abrikosov, A. E. Kissavos, F. Liot, B. Alling, S. I. Simak, O. Peil, and A. V. Ruban. Competition between magnetic structures in the fe rich fcc feni alloys. *Phys. Rev. B*, 76:014434, Jul 2007.

[3] K. Adachi, D. Bonneberg, J.J.M. Franse, R. Gersdorf, K.A. Hempel, K. Kanematsu, S. Misawa, B. Stearns, and H.P.J. Wijn. *3d, 4d, and 5d Elements, Alloys and Compounds / 3d-, 4d- und 5d-Elemente, Legierungen und Verbindungen*. Zahlenwerte und Funktionen aus Naturwissenschaften und Technik: Kristall- und Festkörperphysik. Springer, 1986.

[4] O.K. Andersen. Linear methods in band theory. *Phys. Rev. B*, 12(8):3060–3083, 1975.

[5] V.I. Anisimov, J. Zaanen, and O. Andersen. Band theory and mott insulators: Hubbard u instead of stoner i. *Phys. Rev. B*, 44(3):943–953, 1991.

[6] D. Antonangeli, M. Krisch, G. Fiquet, J. Badro, D. L. Farber, A. Bossak, and S. Merkel. Aggregate and single-crystalline elasticity of hcp cobalt at high pressure. *Phys. Rev. B*, 72:134303, Oct 2005.

[7] Daniele Antonangeli, Laura Robin Benedetti, Daniel L. Farber, Gerd SteinleNeumann, Anne line Auzende, James Badro, Michael Hanfland, and Michael Krisch. Anomalous pressure evolution of the axial ratio c/a in hcp cobalt: Interplay between structure, magnetism, and lattice dynamics. *Applied Physics Letters*, 92(11):111911, 2008.

[8] V. Antonov, B. Harmon, and A.N. Yaresko. *Electronic Structure and Magneto-Optical Properties of Solids*. Kluwer Academic,Dordrecht, 2004.

[9] V. N. Antonov, B. N. Harmon, and A. N. Yaresko. Electronic structure and x-ray magnetic circular dichroism in fe_3o_4 and mn-, Co−, or ni-substituted fe_3o_4. *Phys. Rev. B*, 67:024417, Jan 2003.

[10] Thomas Ayral, Silke Biermann, and Philipp Werner. Screening and nonlocal correlations in the extended hubbard model from self-consistent combined *gw* and dynamical mean field theory. *Phys. Rev. B*, 87:125149, Mar 2013.

[11] Vincenzo Barone. Inclusion of hartree-fock exchange in the density functional approach. benchmark computations for diatomic molecules containing h, b, c, n, o, and f atoms. *Chemical Physics Letters*, 226(3-4):392 – 398, 1994.

[12] Axel D. Becke. A new mixing of hartree–fock and local density-functional theories. *The Journal of Chemical Physics*, 98(2):1372–1377, 1993.

[13] G. Beylkin. On the representation of operators in bases of compactly supported wavelets. *SIAM Journal on Numerical Analysis*, 29(6):1716–1740, 1992.

[14] P. Blaha, K. Schwarz, G. Madsen, D. Kvasnicka, and J. Luitz. Wien2k. http://www.wien2k.at/index.html, 2008.

[15] P. E. Blöchl. Projector augmented-wave method. *Phys. Rev. B*, 50:17953–17979, Dec 1994.

[16] N. Bohr. Xxxvii. on the constitution of atoms and molecules. *Philosophical Magazine Series 6*, 26(153):476–502, 1913.

[17] M. Born and R. Oppenheimer. Zur quantentheorie der molekulen. *Ann. Phys. (Leipzig)*, 84:457–484, 1927.

[18] A. Brinkman, M. Huijben, M. Van Zalk, J. Huijben, U. Zeitler, J. C. Maan, W. G. Van der Wiel, G. Rijnders, D. H. A. Blank, and H. Hilgenkamp. Magnetic effects at the interface between non-magnetic oxides. *NATURE MATERIALS*, 6(7):493–496, JUL 2007.

[19] M. S. S. Brooks and P. J. Kelly. Large orbital-moment contribution to $5f$ band magnetism. *Phys. Rev. Lett.*, 51:1708–1711, Oct 1983.

[20] M.S.S. Brooks. Calculated ground state properties of light actinide metals and their compounds. *Physica B+C*, 130(1 - 3):6 – 12, 1985.

[21] Patrick Bruno. Tight-binding approach to the orbital magnetic moment and magnetocrystalline anisotropy of transition-metal monolayers. *Phys. Rev. B*, 39:865–868, Jan 1989.

[22] W.G. Burgers. On the process of transition of the cubic-body-centered modification into the hexagonal-close-packed modification of zirconium. *Physica*, 1(7–12):561 – 586, 1934.

[23] E. Burzo and P. Vlaic. Magnetic properties of iron-palladium solid solutions and compounds. *J. Optoelectron. Adv. Mater*, 12(9):1869–1878, SEP 2010.

[24] W. H. Butler, X.-G. Zhang, T. C. Schulthess, and J. M. MacLaren. Spin-dependent tunneling conductance of Fe|MgO|Fe sandwiches. *Phys. Rev. B*, 63:054416, Jan 2001.

[25] Paolo Carra, B. T. Thole, Massimo Altarelli, and Xindong Wang. X-ray circular dichroism and local magnetic fields. *Phys. Rev. Lett.*, 70:694–697, Feb 1993.

[26] S. Chadov, J. Minr, M. I. Katsnelson, H. Ebert, D. Kdderitzsch, and A. I. Lichtenstein. Orbital magnetism in transition metal systems: The role of local correlation effects. *EPL (Europhysics Letters)*, 82(3):37001, 2008.

[27] Claude Chappert, Albert Fert, and Frederic Nguyen Van Dau. The emergence of spin electronics in data storage. *NATURE MATERIALS*, 6(11):813–823, NOV 2007.

[28] C. T. Chen, Y. U. Idzerda, H.-J. Lin, N. V. Smith, G. Meigs, E. Chaban, G. H. Ho, E. Pellegrin, and F. Sette. Experimental confirmation of the x-ray magnetic circular dichroism sum rules for iron and cobalt. *Phys. Rev. Lett.*, 75:152–155, Jul 1995.

[29] C. T. Chen, F. Sette, Y. Ma, and S. Modesti. Soft-x-ray magnetic circular dichroism at the $l_{2,3}$ edges of nickel. *Phys. Rev. B*, 42:7262–7265, Oct 1990.

[30] Andrea Dal Corso and Raffaele Resta. Density-functional theory of macroscopic stress: Gradient-corrected calculations for crystalline se. *Phys. Rev. B*, 50:4327–4331, Aug 1994.

[31] I. Daubechies. *Ten Lectures on Wavelets*. CBMS-NSF Regional Conference Series in Applied Mathematics. Society for Industrial and Applied Mathematics, 1992.

[32] Frédéric Decremps and Lucie Nataf. Abrupt discontinuity of the bulk modulus pressure dependence in $fe_{64}ni_{36}$. *Phys. Rev. Lett.*, 92:157204, Apr 2004.

[33] Agnès Dewaele, Marc Torrent, Paul Loubeyre, and Mohamed Mezouar. Compression curves of transition metals in the mbar range: Experiments and projector augmented-wave calculations. *Phys. Rev. B*, 78:104102, Sep 2008.

[34] A. Díaz-Ortiz, R. Drautz, M. Fähnle, H. Dosch, and J. M. Sanchez. Structure and magnetism in bcc-based iron-cobalt alloys. *Phys. Rev. B*, 73:224208, Jun 2006.

[35] Leonid Dubrovinsky, Natalia Dubrovinskaia, Igor A. Abrikosov, Marie Vennström, Frank Westman, Stefan Carlson, Mark van Schilfgaarde, and Börje Johansson. Pressure-induced invar effect in fe-ni alloys. *Phys. Rev. Lett.*, 86:4851–4854, May 2001.

[36] Biswanath Dutta, Sumanta Bhandary, Subhradip Ghosh, and Biplab Sanyal. First-principles study of magnetism in pd_3fe under pressure. *Phys. Rev. B*, 86:024419, Jul 2012.

[37] H. Ebert. Two ways to perform spin-polarized relativistic linear muffin-tin-orbital calculations. *Phys. Rev. B*, 38:9390–9397, Nov 1988.

[38] H Ebert. Magneto-optical effects in transition metal systems. *Reports on Progress in Physics*, 59(12):1665, 1996.

[39] H. Ebert, P. Strange, and B. L. Gyorffy. Theory of circularly polarized x-ray absorption by ferromagnetic fe. *Journal of Applied Physics*, 63(8):3055–3057, 1988.

[40] H. Ebert and R. Zeller. Theoretical study of the magnetic x-ray dichroism of os, ir, pt, and au impurities in fe. *Phys. Rev. B*, 42:2744–2751, Aug 1990.

[41] P. Ehrenfest. Bemerkung ber die angenherte gltigkeit der klassischen mechanik innerhalb der quantenmechanik. *Zeitschrift fr Physik*, 45:455–457, 1927.

[42] Mathias Ekman, Babak Sadigh, Kristin Einarsdotter, and Peter Blaha. Ab initio study of the martensitic bcc-hcp transformation in iron. *Phys. Rev. B*, 58:5296–5304, Sep 1998.

[43] Yasuo Endoh and Yoshikazu Ishikawa. Antiferromagnetism of γ iron manganes alloys. *Journal of the Physical Society of Japan*, 30(6):1614–1627, 1971.

[44] O Eriksson, B Johansson, and M S S Brooks. Meta-magnetism in ucoal. *Journal of Physics: Condensed Matter*, 1(25):4005, 1989.

[45] Olle Eriksson, M. S. S. Brooks, and Börje Johansson. Orbital polarization in narrow-band systems: Application to volume collapses in light lanthanides. *Phys. Rev. B*, 41:7311–7314, Apr 1990.

[46] Olle Eriksson, Börje Johansson, R. C. Albers, A. M. Boring, and M. S. S. Brooks. Orbital magnetism in fe, co, and ni. *Phys. Rev. B*, 42:2707–2710, Aug 1990.

[47] J. L. Erskine and E. A. Stern. Calculation of the M_{23} magneto-optical absorption spectrum of ferromagnetic nickel. *Phys. Rev. B*, 12:5016–5024, Dec 1975.

[48] Michael Faraday. Experimental researches in electricity. nineteenth series. *Philosophical Transactions of the Royal Society of London*, 136:1–20, 1846.

[49] P. Fazekas. *Lecture Notes on Electron Correlation and Magnetism*. Series in Modern Condensed Matter Physics. World Scientific, 1999.

[50] R. P. Feynman. Forces in molecules. *Phys. Rev.*, 56:340–343, Aug 1939.

[51] Alessio Filippetti and Vincenzo Fiorentini. Faceting and stress of missing-row reconstructed transition-metal (110) surfaces. *Phys. Rev. B*, 60:14366–14371, Nov 1999.

[52] Alessio Filippetti and Vincenzo Fiorentini. Theory and applications of the stress density. *Phys. Rev. B*, 61:8433–8442, Mar 2000.

[53] V. Fock. Approximation method for the solution of the quantum mechanical multibody problems. *ZEITSCHRIFT FUR PHYSIK*, 61(1-2):126–148, JAN 1930.

[54] V. Fock. Bemerkung zum virialsatz. *Zeitschrift fr Physik*, 63:855–858, 1930.

[55] M. Friák and M. Šob. *Ab initio* study of the bcc-hcp transformation in iron. *Phys. Rev. B*, 77:174117, May 2008.

[56] I. Galanakis and E. aolu. Ab-initio calculation of effective exchange interactions, spin waves, and curie temperature in l21- and l12-type local moment ferromagnets. *Journal of Materials Science*, 47:7678–7685, 2012.

[57] Luigi Genovese, Thierry Deutsch, and Stefan Goedecker. Efficient and accurate three-dimensional poisson solver for surface problems. *The Journal of Chemical Physics*, 127(5):054704, 2007.

[58] Luigi Genovese, Thierry Deutsch, Alexey Neelov, Stefan Goedecker, and Gregory Beylkin. Efficient solution of poisson's equation with free boundary conditions. *The Journal of Chemical Physics*, 125(7):074105, 2006.

[59] Luigi Genovese, Alexey Neelov, Stefan Goedecker, Thierry Deutsch, Seyed Alireza Ghasemi, Alexander Willand, Damien Caliste, Oded Zilberberg, Mark Rayson, Anders Bergman, and Reinhold Schneider. Daubechies wavelets as a basis set for density functional pseudopotential calculations. *The Journal of Chemical Physics*, 129(1):014109, 2008.

[60] Luigi Genovese, Brice Videau, Matthieu Ospici, Thierry Deutsch, Stefan Goedecker, and Jean-Franois Mhaut. Daubechies wavelets for high performance electronic structure calculations: The bigdft project. *Comptes Rendus Mcanique*, 339(2-3):149 – 164, 2011.

[61] S. Goedecker. *Wavelets and Their Application: For the Solution of Partial Differential Equations in Physics*. Cahiers de physique. Université, Bâtiment des sciences physiques, M.D. Reymond, 1998.

[62] S. Goedecker, M. Teter, and J. Hutter. Separable dual-space gaussian pseudopotentials. *Phys. Rev. B*, 54:1703–1710, Jul 1996.

[63] Alexander F. Goncharov, Jonathan Crowhurst, and Joseph M. Zaug. Elastic and vibrational properties of cobalt to 120 gpa. *Phys. Rev. Lett.*, 92:115502, Mar 2004.

[64] X. Gonze, B. Amadon, P.-M. Anglade, J.-M. Beuken, F. Bottin, P. Boulanger, F. Bruneval, D. Caliste, R. Caracas, M. Ct, T. Deutsch, L. Genovese, Ph. Ghosez, M. Giantomassi, S. Goedecker, D.R. Hamann, P. Hermet, F. Jollet, G. Jomard, S. Leroux, M. Mancini, S. Mazevet, M.J.T. Oliveira, G. Onida, Y. Pouillon, T. Rangel, G.-M. Rignanese, D. Sangalli, R. Shaltaf, M. Torrent, M.J. Verstraete, G. Zerah, and J.W. Zwanziger. Abinit: First-principles approach to material and nanosystem properties. *Computer Physics Communications*, 180(12):2582 – 2615, 2009.

[65] X. Gonze, G.M. Rignanese, M. Verstraete, J.M. Beuken, Y. Pouillon, R. Caracas, F. Jollet, M. Torrent, G. Zerah, M. Mikami, P. Ghosez, M. Veithen, J.Y. Raty, V. Olevano, F. Bruneval, L. Reining, R. Godby, G. Onida, D.R. Hamann, and D.C. Allan. A brief introduction to the abinit software package. *Zeitschrift fur Kristallographie*, 220:558–562, may 2005.

[66] J.B. Goodenough. *Magnetism and the chemical bond*. Interscience monographs on chemistry: Inorganic chemistry section. Interscience Publishers, 1963.

[67] H J Gotsis and P Strange. A first-principles theory of x-ray faraday effects. *Journal of Physics: Condensed Matter*, 6(7):1409, 1994.

[68] A. Gunnarsson. The stoner model in the spin-density-functional formalism. *Physica B+C*, 91(0):329 – 336, 1977.

[69] O Gunnarsson. Band model for magnetism of transition metals in the spin-density-functional formalism. *Journal of Physics F: Metal Physics*, 6(4):587, 1976.

[70] O. Gunnarsson, O. K. Andersen, O. Jepsen, and J. Zaanen. Density-functional calculation of the parameters in the anderson model: Application to mn in cdte. *Phys. Rev. B*, 39:1708–1722, Jan 1989.

[71] G Y Guo. What does the k-edge x-ray magnetic circular dichroism spectrum tell us? *Journal of Physics: Condensed Matter*, 8(49):L747, 1996.

[72] B.L. Gyorffy, A.J. Pindor, J. Staunton, G.M. Stocks, and H. Winter. A 1st-principles theory of ferromagnetic phase-transitions in metals. *Journal of Physics F: Metal Physics*, 15(6):1337–1386, 1985.

[73] Philipp Haas, Fabien Tran, and Peter Blaha. Calculation of the lattice constant of solids with semilocal functionals. *Phys. Rev. B*, 79:085104, Feb 2009.

[74] S. V. Halilov, H. Eschrig, A. Y. Perlov, and P. M. Oppeneer. Adiabatic spin dynamics from spin-density-functional theory: Application to fe, co, and ni. *Phys. Rev. B*, 58:293–302, Jul 1998.

[75] M. Hansen. *Constitution of Binary Alloys, Metallurgy and Metallurgical Engineering Series*. McGraw-Hill, New York, 1958.

[76] D. Hartree. Wave mechanics of an atom with a non-coulomb central field. *Proc.Cambridge Philos.Soc.*, 24:89, 1928.

[77] C. Hartwigsen, S. Goedecker, and J. Hutter. Relativistic separable dual-space gaussian pseudopotentials from h to rn. *Phys. Rev. B*, 58:3641–3662, Aug 1998.

[78] P. Hohenberg and W. Kohn. Inhomogeneous electron gas. *Phys. Rev.*, 136, $\mathcal{N}^{o}$ 3:B864–B871, 1964.

[79] J. Hubbard. Electron correlations in narrow energy bands. *Proceedings of the Royal Society of London. Series A. Mathematical and Physical Sciences*, 276(1365):238–257, 1963.

[80] Mark S. Hybertsen and Steven G. Louie. Electron correlation in semiconductors and insulators: Band gaps and quasiparticle energies. *Phys. Rev. B*, 34:5390–5413, Oct 1986.

[81] Jun-ichi Igarashi and Kunitomo Hirai. Magnetic circular dichroism at the K edge of nickel and iron. *Phys. Rev. B*, 50:17820–17829, Dec 1994.

[82] Valentin Iota, Jae-Hyun Park Klepeis, Choong-Shik Yoo, Jonathan Lang, Daniel Haskel, and George Srajer. Electronic structure and magnetism in compressed 3d transition metals. *Applied Physics Letters*, 90(4):042505, 2007.

[83] Naoki Ishimatsu, Naomi Kawamura, Hiroshi Maruyama, Masaichiro Mizumaki, Takahiro Matsuoka, Hirokatsu Yumoto, Haruhiko Ohashi, and Motohiro Suzuki. Paramagnetism with anomalously large magnetic susceptibility in β(fcc)-cobalt probed by x-ray magnetic circular dichroism up to 170 gpa. *Phys. Rev. B*, 83:180409, May 2011.

[84] Naoki Ishimatsu, Hiroshi Maruyama, Naomi Kawamura, Motohiro Suzuki, Yasuo Ohishi, and Osamu Shimomura. Stability of ferromagnetism in fe, co, and ni metals under high pressure. *Journal of the Physical Society of Japan*, 76(6):064703, 2007.

[85] P. James, O. Eriksson, B. Johansson, and I. A. Abrikosov. Calculated magnetic properties of binary alloys between fe, co, ni, and cu. *Phys. Rev. B*, 59:419–430, Jan 1999.

[86] T Jarlborg. Spin fluctuations, electronphonon coupling and superconductivity in near-magnetic elementary metalsfe, co, ni and pd. *Physica C: Superconductivity*, 385(4):513 – 524, 2003.

[87] T Jo. On the possibility of the multiple spin density wave state in the first-kind antiferromagnetic fcc metals. *Journal of Physics F: Metal Physics*, 13(10):L211, 1983.

[88] R.O. Jones and O. Gunnarson. The density functional formalism, its applications and prospects. *Rev. Mod. Phys.*, 61, $\mathcal{N}^{\circ}$3:689–746, 1989.

[89] M. Karolak, G. Ulm, T. Wehling, V. Mazurenko, A. Poteryaev, and A. Lichtenstein. Double counting in lda+dmft – the example of nio. *Journal of Electron Spectroscopy and Related Phenomena*, 181(1):11 – 15, 2010. ¡ce:title¿Proceedings of International Workshop on Strong Correlations and Angle-Resolved Photoemission Spectroscopy 2009¡/ce:title¿.

[90] Shuzo Kawarazaki, Kazuhiro Fujita, Katsumi Yasuda, Yutaka Sasaki, Takao Mizusaki, and Akira Hirai. Direct evidence for triple-q spin-density wave in fcc antiferromagnetic mn-ni alloy. *Phys. Rev. Lett.*, 61:471–474, Jul 1988.

[91] S J Kennedy and T J Hicks. The magnetic structure of -iron-manganese. *Journal of Physics F: Metal Physics*, 17(7):1599, 1987.

[92] S. Khmelevskyi and P. Mohn. Laves-phase $(\mathrm{Zr}, \mathrm{Nb})\mathrm{fe}_2$ alloys as model invar systems without magnetic frustration: Comparison to fe-ni invar. *Phys. Rev. B*, 82:134402, Oct 2010.

[93] S. Khmelevskyi, A.V. Ruban, and P. Mohn. Frustrated magnetism in superconducting hexagonal fe: Calculation of inter-atomic pair exchange interactions. *Physica C: Superconductivity*, 460462, Part 1(0):647 – 648, 2007. ¡ce:title¿Proceedings of the 8th International Conference on Materials and Mechanisms of Superconductivity and High Temperature Superconductors¡/ce:title¿ ¡ce:subtitle¿M2S-HTSC VIII¡/ce:subtitle¿.

[94] Sergii Khmelevskyi and Peter Mohn. Critical behavior of disordered fcc $\mathrm{fe}_{70}\mathrm{pt}_{30}$ alloy under high pressure. *Phys. Rev. B*, 68:214412, Dec 2003.

[95] Leonard Kleinman and D. M. Bylander. Efficacious form for model pseudopotentials. *Phys. Rev. Lett.*, 48:1425–1428, May 1982.

[96] W. Kohn and L.J. Sham. Self-consistent equations including exchange and correlation effects. *Phys. Rev.*, 140, $\mathcal{N}^{\circ}$ 4:A1133–A1137, 1965.

[97] G. Kotliar, S. Y. Savrasov, K. Haule, V. S. Oudovenko, O. Parcollet, and C. A. Marianetti. Electronic structure calculations with dynamical mean-field theory. *Rev. Mod. Phys.*, 78(3):865–951, JUL-SEP 2006.

[98] J.S. Kouvel and J.S. Kasper. Long-range antiferromagnetism in disordered fe-ni-mn alloys. *Journal of Physics and Chemistry of Solids*, 24(4):529 – 536, 1963.

[99] Georg Kresse, Martijn Marsman, and Jürgen Furthmüller. Vasp: Vienna ab-initio simulation package. http://cms.mpi.univie.ac.at/VASP/, 2007.

[100] J. Kudrnovský, I. Turek, A. Pasturel, R. Tetot, V. Drchal, and P. Weinberger. Magnetism-induced ordering in two and three dimensions. *Phys. Rev. B*, 50:9603–9606, Oct 1994.

[101] J. Kuneš, Dm. M. Korotin, M. A. Korotin, V. I. Anisimov, and P. Werner. Pressure-driven metal-insulator transition in hematite from dynamical mean-field theory. *Phys. Rev. Lett.*, 102:146402, Apr 2009.

[102] Jan Kunes, Alexey V. Lukoyanov, Vladimir I. Anisimov, Richard T. Scalettar, and Warren E. Pickett. Collapse of magnetic moment drives the mott transition in mno. *NATURE MATERIALS*, 7(3):198–202, MAR 2008.

[103] Y. O. Kvashnin, S. Khmelevskyi, J. Kudrnovský, A. N. Yaresko, L. Genovese, and P. Bruno. Noncollinear magnetic ordering in compressed $\mathrm{fepd_3}$ ordered alloy: A first principles study. *Phys. Rev. B*, 86:174429, Nov 2012.

[104] F. Lechermann, F. Welsch, C. Elsässer, C. Ederer, M. Fähnle, J. M. Sanchez, and B. Meyer. Density-functional study of $\mathrm{fe_3Al}$: lsda versus gga. *Phys. Rev. B*, 65:132104, Mar 2002.

[105] A.I. Liechtenstein, M.I. Katsnelson, V.P. Antropov, and V.A. Gubanov. Local spin density functional approach to the theory of exchange interactions in ferromagnetic metals and alloys. *Journal of Magnetism and Magnetic Materials*, 67(1):65 – 74, 1987.

[106] Raquel Lizárraga, Lars Nordström, Olle Eriksson, and John Wills. Noncollinear magnetism in the high-pressure hcp phase of iron. *Phys. Rev. B*, 78:064410, Aug 2008.

[107] M W Long. Effects that can stabilise multiple spin-density waves. *Journal of Physics: Condensed Matter*, 1(17):2857, 1989.

[108] Steven G. Louie, Sverre Froyen, and Marvin L. Cohen. Nonlinear ionic pseudopotentials in spin-density-functional calculations. *Phys. Rev. B*, 26:1738–1742, Aug 1982.

[109] A H MacDonald, W E Picket, and D D Koelling. A linearised relativistic augmented-plane-wave method utilising approximate pure spin basis functions. *Journal of Physics C: Solid State Physics*, 13(14):2675, 1980.

[110] J. M. MacLaren, T. C. Schulthess, W. H. Butler, Roberta Sutton, and Michael McHenry. Electronic structure, exchange interactions, and curie temperature of feco. *Journal of Applied Physics*, 85(8):4833–4835, 1999.

[111] G. Makov and M. C. Payne. Periodic boundary conditions in *ab initio* calculations. *Phys. Rev. B*, 51:4014–4022, Feb 1995.

[112] R. Maranganti and P. Sharma. Revisiting quantum notions of stress. *Proceedings of the Royal Society A: Mathematical, Physical and Engineering Science*, 466(2119):2097–2116, 2010.

[113] Miguel A.L. Marques, Micael J.T. Oliveira, and Tobias Burnus. Libxc: A library of exchange and correlation functionals for density functional theory. *Computer Physics Communications*, 183(10):2272 – 2281, 2012.

[114] R.M. Martin. *Electronic Structure: Basic Theory and Practical Methods*. Cambridge University Press, 2004.

[115] O. Mathon, F. Baudelet, J. P. Itié, A. Polian, M. d'Astuto, J. C. Chervin, and S. Pascarelli. Dynamics of the magnetic and structural $\alpha - \epsilon$ phase transition in iron. *Phys. Rev. Lett.*, 93:255503, Dec 2004.

[116] M. Matsushita, S. Endo, K. Miura, and F. Ono. Evidence of new high-pressure magnetic phases in fe–pt invar alloy. *Journal of Magnetism and Magnetic Materials*, 260(3):371 – 374, 2003.

[117] M. Matsushita, S. Endo, K. Miura, and F. Ono. Pressure induced magnetic phase transition in fe–ni invar alloy. *Journal of Magnetism and Magnetic Materials*, 265(3):352 – 356, 2003.

[118] P. Modak, A. K. Verma, R. S. Rao, B. K. Godwal, and R. Jeanloz. *Ab initio* total-energy and phonon calculations of co at high pressures. *Phys. Rev. B*, 74:012103, Jul 2006.

[119] Yousif Shoaib Mohammed, Yu Yan, Hongxia Wang, Kai Li, and Xiaobo Du. Stability of ferromagnetism in fe, co, and ni metals under high pressure with gga and gga+u. *Journal of Magnetism and Magnetic Materials*, 322(6):653 – 657, 2010.

[120] P. Mohn. *Magnetism in the Solid State: An Introduction.* Springer Series in Solid-State Sciences. Springer, 2003.

[121] P Mohn and K Schwarz. Supercell calculations for transition metal impurities in palladium. *Journal of Physics: Condensed Matter*, 5(29):5099, 1993.

[122] O. N. Mryasov, U. Nowak, K. Y. Guslienko, and R. W. Chantrell. Temperature-dependent magnetic properties of fept: Effective spin hamiltonian model. *EPL (Europhysics Letters)*, 69(5):805, 2005.

[123] Oleg N. Mryasov. Magnetic interactions and phase transformations in fem, m=(pt, rh) ordered alloys. *Phase Transitions*, 78(1-3):197–208, 2005.

[124] O. H. Nielsen and Richard M. Martin. First-principles calculation of stress. *Phys. Rev. Lett.*, 50:697–700, Feb 1983.

[125] O. H. Nielsen and Richard M. Martin. Quantum-mechanical theory of stress and force. *Phys. Rev. B*, 32:3780–3791, Sep 1985.

[126] O. H. Nielsen and Richard M. Martin. Stresses in semiconductors: *Ab initio* calculations on si, ge, and gaas. *Phys. Rev. B*, 32:3792–3805, Sep 1985.

[127] A Ohtomo and HY Hwang. A high-mobility electron gas at the laalo3/srtio3 heterointerface. *NATURE*, 427(6973):423–426, JAN 29 2004.

[128] W. Olovsson and I. A. Abrikosov. Variation of the effective exchange parameter across 3d-transition-metal series. *Journal of Applied Physics*, 97(10):10A317, 2005.

[129] A Oswald, R Zeller, P J Braspenning, and P H Dederichs. Interaction of magnetic impurities in cu and ag. *Journal of Physics F: Metal Physics*, 15(1):193, 1985.

[130] M. Pajda, J. Kudrnovský, I. Turek, V. Drchal, and P. Bruno. *Ab initio* calculations of exchange interactions, spin-wave stiffness constants, and curie temperatures of fe, co, and ni. *Phys. Rev. B*, 64:174402, Oct 2001.

[131] E. Pavarini, S. Biermann, A. Poteryaev, A. I. Lichtenstein, A. Georges, and O. K. Andersen. Mott transition and suppression of orbital fluctuations in orthorhombic $3d^1$ perovskites. *Phys. Rev. Lett.*, 92:176403, Apr 2004.

[132] Rossitza Pentcheva and Warren E. Pickett. Ionic relaxation contribution to the electronic reconstruction at the n-type $\mathrm{laalo_3/srtio_3}$ interface. *Phys. Rev. B*, 78:205106, Nov 2008.

[133] W. Pepperhoff and M. Acet. *Constitution and Magnetism of Iron and its Alloys*. Spring-Verlag, Berlin, 2001.

[134] J. P. Perdew and Alex Zunger. Self-interaction correction to density-functional approximations for many-electron systems. *Phys. Rev. B*, 23:5048–5079, May 1981.

[135] John P. Perdew, Kieron Burke, and Matthias Ernzerhof. Generalized gradient approximation made simple. *Phys. Rev. Lett.*, 77:3865–3868, Oct 1996.

[136] John P. Perdew and Yue Wang. Accurate and simple analytic representation of the electron-gas correlation energy. *Phys. Rev. B*, 45:13244–13249, Jun 1992.

[137] S. Polesya, S. Mankovsky, O. Sipr, W. Meindl, C. Strunk, and H. Ebert. Finite-temperature magnetism of $\mathrm{fe}_x\mathrm{pd}_{1-x}$ and $\mathrm{co}_x\mathrm{pt}_{1-x}$ alloys. *Phys. Rev. B*, 82:214409, Dec 2010.

[138] N. Reyren, S. Thiel, A. D. Caviglia, L. Fitting Kourkoutis, G. Hammerl, C. Richter, C. W. Schneider, T. Kopp, A.-S. Retschi, D. Jaccard, M. Gabay, D. A. Muller, J.-M. Triscone, and J. Mannhart. Superconducting interfaces between insulating oxides. *Science*, 317(5842):1196–1199, 2007.

[139] Andrei Rogalev, Fabrice Wilhelm, Nicolas Jaouen, Jos Goulon, and Jean-Paul Kappler. X-ray magnetic circular dichroism: Historical perspective and recent highlights. In Eric Beaurepaire, Herv Bulou, Fabrice Scheurer, and Jean-Paul

Kappler, editors, *Magnetism: A Synchrotron Radiation Approach*, volume 697 of *Lecture Notes in Physics*, pages 71–93. Springer Berlin Heidelberg, 2006.

[140] A. V. Ruban, M. I. Katsnelson, W. Olovsson, S. I. Simak, and I. A. Abrikosov. Origin of magnetic frustrations in fe–ni invar alloys. *Phys. Rev. B*, 71:054402, Feb 2005.

[141] Andrei V. Ruban, Sergii Khmelevskyi, Peter Mohn, and Börje Johansson. Magnetic state, magnetovolume effects, and atomic order in $fe_{65}ni_{35}$ invar alloy: A first principles study. *Phys. Rev. B*, 76:014420, Jul 2007.

[142] M. A. Ruderman and C. Kittel. Indirect exchange coupling of nuclear magnetic moments by conduction electrons. *Phys. Rev.*, 96:99–102, Oct 1954.

[143] Erich Runge and E. K. U. Gross. Density-functional theory for time-dependent systems. *Phys. Rev. Lett.*, 52:997–1000, Mar 1984.

[144] James E Saal, ShunLi Shang, Yi Wang, and Zi-Kui Liu. Magnetic phase transformations of face-centered cubic and hexagonal close-packed co at zero kelvin. *Journal of Physics: Condensed Matter*, 22(9):096006, 2010.

[145] A. Sakuma, K. Fukamichi, K. Sasao, and R. Y. Umetsu. First-principles study of the magnetic structures of ordered and disordered mn-ir alloys. *Phys. Rev. B*, 67:024420, Jan 2003.

[146] L. M. Sandratskii. Symmetry analysis of electronic states for crystals with spiral magnetic order .1. general-properties. *Journal of Physics: Condensed Matter*, 3(44):8565–8585, NOV 4 1991.

[147] L. M. Sandratskii. Noncollinear magnetism in itinerant-electron systems: Theory and applications. *Advances in Physics*, 47(1):91–160, 1998.

[148] L. M. Sandratskii, R. Singer, and E. Şaşıoğlu. Heisenberg hamiltonian description of multiple-sublattice itinerant-electron systems: General considerations and applications to nimnsb and mnas. *Phys. Rev. B*, 76:184406, Nov 2007.

[149] G. Schütz, W. Wagner, W. Wilhelm, P. Kienle, R. Zeller, R. Frahm, and G. Materlik. Absorption of circularly polarized x rays in iron. *Phys. Rev. Lett.*, 58:737–740, Feb 1987.

[150] K Schwarz, P Mohn, P Blaha, and J Kubler. Electronic and magnetic structure of bcc fe-co alloys from band theory. *Journal of Physics F: Metal Physics*, 14(11):2659, 1984.

[151] J. Slater. Note on hartree's method. *Phys. Rev.*, 35:210, 1930.

[152] J. C. Slater. The virial and molecular structure. *The Journal of Chemical Physics*, 1(10):687–691, 1933.

[153] Daniel Stanek, Oleg P. Sushkov, and Götz S. Uhrig. Self-consistent spin-wave theory for a frustrated heisenberg model with biquadratic exchange in the columnar phase and its application to iron pnictides. *Phys. Rev. B*, 84:064505, Aug 2011.

[154] Gerd Steinle-Neumann, Lars Stixrude, and Ronald E. Cohen. Magnetism in dense hexagonal iron. *Proceedings of the National Academy of Sciences*, 101(1):33–36, 2004.

[155] J. Stöhr and H.C. Siegmann. *Magnetism: from fundamentals to nanoscale dynamics*. Springer series in solid-state sciences. Springer, 2006.

[156] Edmund C. Stoner. Collective electron ferromagnetism. *Proceedings of the Royal Society of London. Series A. Mathematical and Physical Sciences*, 165(922):372–414, 1938.

[157] L. Szunyogh, B. Lazarovits, L. Udvardi, J. Jackson, and U. Nowak. Giant magnetic anisotropy of the bulk antiferromagnets irmn and $irmn_3$ from first principles. *Phys. Rev. B*, 79:020403, Jan 2009.

[158] B. T. Thole, P. Carra, F. Sette, and G. van der Laan. X-ray circular dichroism as a probe of orbital magnetization. *Phys. Rev. Lett.*, 68:1943–1946, Mar 1992.

[159] Izumi Tomeno, Hiromi N. Fuke, Hitoshi Iwasaki, Masashi Sahashi, and Yorihiko Tsunoda. Magnetic neutron scattering study of ordered mn_3ir. *Journal of Applied Physics*, 86(7):3853–3856, 1999.

[160] R. Torchio, Y. O. Kvashnin, S. Pascarelli, O. Mathon, C. Marini, L. Genovese, P. Bruno, G. Garbarino, A. Dewaele, F. Occelli, and P. Loubeyre. X-ray magnetic circular dichroism measurements in ni up to 200 gpa: Resistant ferromagnetism. *Phys. Rev. Lett.*, 107:237202, Nov 2011.

[161] R. Torchio, A. Monza, F. Baudelet, S. Pascarelli, O. Mathon, E. Pugh, D. Antonangeli, and J. Paul Itié. Pressure-induced collapse of ferromagnetism in cobalt up to 120 gpa as seen via x-ray magnetic circular dichroism. *Phys. Rev. B*, 84:060403, Aug 2011.

[162] G. Trimarchi and N. Binggeli. Structural and electronic properties of $LaMno_3$ under pressure: an *ab initio* LDA + U study. *Phys. Rev. B*, 71:035101, Jan 2005.

[163] I. Turek, V. Drchal, J. Kudrnovsky, M. Sob, and P. P. Weinberger. *Electronic Structure of Disordered Alloys, Surfaces and Interfaces*. Kluwer Academic, Boston, 1997.

[164] Gerrit van der Laan, Bernard T. Thole, George A. Sawatzky, Jeroen B. Goedkoop, John C. Fuggle, Jean-Marc Esteva, Ramesh Karnatak, J. P. Remeika, and Hanna A. Dabkowska. Experimental proof of magnetic x-ray dichroism. *Phys. Rev. B*, 34:6529–6531, Nov 1986.

[165] M van Schilfgaarde, IA Abrikosov, and B Johansson. Origin of the invar effect in iron-nickel alloys. *NATURE*, 400(6739):46–49, JUL 1 1999.

[166] Paolo Vilmercati, Alexei Fedorov, Federica Bondino, Francesco Offi, Giancarlo Panaccione, Paolo Lacovig, Laura Simonelli, Michael A. McGuire, Athena S. M. Sefat, David Mandrus, Brian C. Sales, Takeshi Egami, Wei Ku, and Norman Mannella. Itinerant electrons, local moments, and magnetic correlations in the pnictide superconductors $cefeaso_{1-x}f_x$ and $sr(fe_{1-x}co_x)_2as_2$. *Phys. Rev. B*, 85:220503, Jun 2012.

[167] U von Barth and L Hedin. A local exchange-correlation potential for the spin polarized case. i. *Journal of Physics C: Solid State Physics*, 5(13):1629, 1972.

[168] S. H. Vosko, L. Wilk, and M. Nusair. Accurate spin-dependent electron liquid correlation energies for local spin density calculations: a critical analysis. *Canadian Journal of Physics*, 58(8):1200–1211, 1980.

[169] P. Weinberger. John kerr and his effects found in 1877 and 1878. *Philosophical Magazine Letters*, 88(12):897–907, 2008.

[170] R. Wienke, G. Schutz, and H. Ebert. Determination of local magnetic moments of 5d impurities in fe detected via spin-dependent absorption. *Journal of Applied Physics*, 69(8):6147–6149, 1991.

[171] Alex Willand, Yaroslav O. Kvashnin, Luigi Genovese, Alvaro Vazquez-Mayagoitia, Arpan Krishna Deb, Ali Sadeghi, Thierry Deutsch, and Stefan Goedecker. Norm-conserving pseudopotentials with chemical accuracy compared to all-electron calculations. *The Journal of Chemical Physics*, 138(10):104109, 2013.

[172] M. L. Winterrose, M. S. Lucas, A. F. Yue, I. Halevy, L. Mauger, J. A. Muñoz, Jingzhu Hu, M. Lerche, and B. Fultz. Pressure-induced invar behavior in pd_3Fe. *Phys. Rev. Lett.*, 102:237202, Jun 2009.

[173] M. L. Winterrose, L. Mauger, I. Halevy, A. F. Yue, M. S. Lucas, J. A. Muñoz, H. Tan, Y. Xiao, P. Chow, W. Sturhahn, T. S. Toellner, E. E. Alp, and B. Fultz. Dynamics of iron atoms across the pressure-induced invar transition in pd_3fe. *Phys. Rev. B*, 83:134304, Apr 2011.

[174] Jianjun Xie, S P Chen, Holmann V Brand, and Ronald L Rabie. High-pressure thermodynamic, electronic and magnetic properties of ni. *Journal of Physics: Condensed Matter*, 12(42):8953, 2000.

[175] C. S. Yoo, H. Cynn, P. Söderlind, and V. Iota. New β(fcc)-cobalt to 210 gpa. *Phys. Rev. Lett.*, 84:4132–4135, May 2000.

[176] Jing Zhu, X. W. Wang, and Steven G. Louie. First-principles pseudopotential calculations of magnetic iron. *Phys. Rev. B*, 45:8887–8893, Apr 1992.